The fate and dynamics of a river plume in the surf zone

Samuel E. Kastner

A dissertation
submitted in partial fulfillment of the
requirements for the degree of

Doctor of Philosophy

University of Washington

2020

Reading Committee:

Alex Horner-Devine, Chair

Jim Thomson, Chair

Melissa Moulton

Program Authorized to Offer Degree:
Civil & Environmental Engineering

University of Washington

Abstract

The fate and dynamics of a river plume in the surf zone

Samuel E. Kastner

Co-Chairs of the Supervisory Committee:
Professor Alex Horner-Devine
Civil & Environmental Engineering

Professor Jim Thomson
Civil & Environmental Engineering

Small river outflows that directly enter the surf zone,where waves break near the shore, are a common feature of the world's coastlines. Rivers transport sediment, nutrients, and pollutants from the terrestrial to the marine environment, and the fate of this material is important for coastal morphology, ecology, and public health. Breaking waves release their energy and momentum in the surf zone, causing it to be energetic and turbulent, yet retentive, as surf zone cross-shore exchange is small on average. Thus, river water and river-borne material may become trapped in the surf zone. Trapped fresh river water is subject to energetic alongshore circulation and turbulence, and may be transported away from the river mouth, undergoing wave-driven mixing. Using observations from the Quinault River, which flows into an energetic surf zone on Quinault Indian Nation land north of Grays Harbor, WA, I investigate the interaction between river and wave forcing in the surf zone. By synthesizing data from moorings, drifters, and Unmanned Aerial System (UAS) video, I develop a conceptual model of this interaction based on river forcing, wave forcing, and the bathymetry near the river mouth. The relationships between these show how tides and bathymetry change the balance of wave and river momentum. Most frequently, wave forcing dominates over river forcing. Under these conditions the surf zone traps the outflowing river

plume and the river water's initial propagation into the surf zone is set by a plume length scale. When the river velocity is highest during low tide, and when wave forcing is low, river forcing dominates over wave forcing and river water escapes the surf zone. At high tide during low wave forcing, bathymetric effects can allow the river water to bypass wave forcing. In this case minimal wave breaking occurs in the channel and river water escapes onto the shelf. Estimates of entrainment velocity based on the drifter propagation distance indicate that mixing may be elevated above theoretical values in the near field plume by surf zone wave breaking. Based on the discharge, wave, and tidal conditions, I use the conceptual model to predict the fate of river water from the Quinault over a year, showing that approximately 70% of the river discharge is trapped in the surf zone upon exiting the river mouth.

Drifter observations from the surf zone near the Quinault River mouth further indicate that the trapping of freshwater in the surf zone can result in high near-surface stratification. I investigate the rate that river water mixes with ocean water using two metrics: the rate of change of salinity in a Lagrangian reference frame, or material derivative of salinity, and the along track salinity variance. High mixing rates are observed concurrently with high near-surface stratification, as salinity gradients are collocated with wave breaking turbulence, which is unaffected by stratification. I observe a transition from low stratification and low mixing rate at low tidal stage to high stratification and high material derivative of salinity at high tidal stage as river discharge decreases. This decrease in surf zone freshwater content is driven by decreased river volume flux and increased wave-driven alongshore transport combining to export freshwater from the river mouth, and is well described by an analytical framework based on a continuously stirred reactor. In contrast with more commonly studied large river plume systems, lateral exchange and mixing could be significant, especially during periods of low stratification and at the surf zone edge. The results of this study may be applied to find the freshwater fraction of the surf zone as well as the alongshore propagation length scale of trapped river water, and to predict when such water would rapidly mix.

Lastly, I synthesize these findings and offer a view of the surf zone from the perspective of trapped river water. Freshwater that is trapped in the surf zone interacts with surf zone features such as rip currents, alongshore currents, and the Stokes' drift-undertow circulation, as well as potentially altering cross-shore surf zone dynamics by introducing a baroclinic pressure gradient. As plume water propagates in the surf zone, it may undergo increased wave-driven mixing as near-surface stratification increases due to the surface intensification of wave breaking turbulence. These observations fall in line with previous work showing that wave driven mixing is greatest when the plume depth is shallow. Thus, the quantity of river water trapped in the surf zone is related to mixing, as the more river water is trapped, the less stratified the surf zone becomes, and less mixing occurs.

TABLE OF CONTENTS

LIST OF FIGURES

ACKNOWLEDGMENTS

The vast majority of my work on this dissertation took place on the unceded ancestral lands of the Duwamish people, past and present; I honor them and the land with my gratitude.

The fieldwork upon which this dissertation is based took place on the land of the Quinault people, and would not have been possible without the advice and consent of the Quinault Indian Nation, particularly the Quinault Division of Natural Resources and Quinault River Committee. I would like to specifically thank Joe Shumacker, Larry Gilbertson, and Kokomo Snell for their help in facilitating the observational program.

The work presented in this dissertation was funded by the National Science Foundation. I would also like to acknowledge funding from Washington State Ferries during my time at UW that expanded the breadth of my research interests.

I could not possibly thank my advisors, Alex Horner-Devine and Jim Thomson, enough for their endless patience and help. Much of my growth as a person and as a researcher is directly attributable to having two fantastic role models from whom to triangulate a path forward. I have learned to lead and be a team player by watching them every week for the past five years, and I continue to be amazed at their dedication to their work and their students. They have helped me find my way through this process with humor and grace. Jim and Alex, thank you for honoring me with your guidance and your trust.

During my undergraduate years at Skidmore College, I was fortunate enough to work with Greg Gerbi. His calm and straightforward explanations of complex concepts to a bewildered 19 year old incessantly asking questions is a continued inspiration. I would not be here without him.

I am honored to count among my mentors Steve Lentz and Anthony Kirincich; during my summer at the Woods Hole Oceanographic Institute, they never failed to remind me that this work should be fun.

Nirnimesh Kumar's ebullient presence was a welcome addition during my time at UW, and I have been grateful for the opportunity to TA in his classes three separate times. Nirni's scientific prowess is second only to his generosity, from which I have greatly benefited.

Despite being over 1200 miles away in San Diego, Sarah Giddings has been incredibly supportive of and influential to my work, serving on my committee and taking time at every conference to meet and talk science.

Melissa Moulton's creativity and even keel has been an inspiration throughout my dissertation work, as she has served on my committee. I have been truly fortunate to have three fantastic young faculty mentors in Nirni, Sarah, and Melissa, and I thank them for their guidance, scientific and otherwise.

I thank Parker MacCready and Rocky Geyer for admitting me to their 2019 Friday Harbor summer school, which confirmed for me that I want to make a career of studying the coastal ocean. I would like to specifically thank Parker for serving on my committee.

Alex DeKlerk and Joe Talbert are true unsung heros of this work; without them, none of the fieldwork presented in this document would have been possible. Their good humor and encouragement in the field turned fieldwork from something that I dreaded to something that I thoroughly enjoy.

The Environmental Fluid Mechanics group made UW, and Seattle, feel like home. Thank you all for the invaluable feedback and encouragement through the years, and for making Thursday something to look forward to. Thanks especially to Seth, Maricarmen, Raul, Roxanne, Maddie, Christine, David, Sam B., Shelby, and Sam F. for being the best officemates and friends I could have asked for.

Katie—thank you for your immeasurable support. The past few years have been made infinitely brighter with you to laugh with; I continue to be in awe of your kindness, diligence, and graciousness.

Being able to see myself in my grandparents, Bernice Kastner, Sid Kastner, Martha Mednick, Sarnoff Mednick, and Birgitte Mednick, all five of whom were professors or researchers in vocation, has been an immense privilege and inspiration for the last five years and throughout my life.

Throughout my time in Seattle, I have always been able to count on my family, even though they live across the country. I would not have lasted more than a month on the West Coast without your support. Thank you, Mom, Dad, and Sophie, for always picking up the phone, for encouraging me, and for believing in me.

INVOCATION

"It's amazing to me how much you can say

when you don't know what you're talking about."

—Phoebe Bridgers, "I See You"

Chapter 1

INTRODUCTION

1.1 Motivation

A river plume forms where fresh river water meets the salty ocean. The river water flows offshore on top the ocean water due to its buoyancy and momentum, leading to complex transport and mixing pathways [Garvine, 1984; Horner-Devine et al., 2015]. Many small river plume systems are further complicated by the effects of ocean surface gravity waves that break nearshore in the surf zone, a region primarily governed by wave processes [Longuet-Higgins, 1970; Thornton and Guza, 1983; Peregrine, 1998]. Small rivers that empty into the surf zone are a common feature on coastlines around the world. These rivers make up a large portion of midlatitude river flow and can export large amounts of sediment relative to their discharge [Milliman and Syvitski, 1992; Izett and Fennel, 2018].

On the West coast of North America, small river systems vary from low inflow estuaries in Southern California to glacial discharge in Washington State and British Columbia. Many of these systems lack channel engineering, such as jetties, at their mouth, leading to surf zone influence on river plume dynamics and the potential for river water to be trapped in the surf zone by strong wave forcing. The dynamics of surf zone-plume interaction are not well understood, but impact the transport of river water and river-borne material. The fate of sediment, pollutants, nutrients, and larvae has significant economic, cultural, ecological, and public health impacts on coastal regions. The Quinault River, on Quinault Nation land on the Olympic Peninsula, empties directly into an energetic surf zone, and the effects of wave dynamics on the fate of river water are important to the ecology of the vulnerable blueback salmon run [Bruscas, 2019; Quinault Division of Natural Resources, 2020]. In Imperial Beach, California, contaminated runoff from the nearby Tijuana River can impact local public health and the economy due to beach closures, a common problem in Southern California [Fry, 2020; Monterey Bay National Marine Sanctuary, 2019].

The 2019 Quinault River blueback sockeye salmon fishing season ended before it began. After the third smallest number of returning salmon on record was recorded in 2018 and bleak 2019 forecasts, the Quinault Nation River Committee made the decision to close the commercial fishing season in February 2019, in advance of the season's typical April start [Bruscas, 2019]. The blueback salmon is culturally significant and economically important to the Quinault people, and blueback numbers have dropped astronomically since the 1950s, when the average annual run consisted of one quarter million salmon [Bruscas, 2019; Quinault Division of Natural Resources, 2020]. Since the 1990s, restoration efforts have been underway in the Quinault River system; still, the 2018 blueback run consisted of only 6619 salmon [Ensmenger, 2010; Bruscas, 2019]. It is therefore important to understand physical mechanisms that could impact the salmon run, including the trapping of Quinault River water in the surf zone. An aerial image of the Quinault River mouth is shown in figure 1.1.

Poor water quality at beaches led to 6500 contamination advisories at 1200 beaches across the United States in 2017 and 2018 [Sherman, 2019]. The three beaches with the most closures were all in Los Angeles county, which experiences closure associated with increased runoff, including from creek and river mouths near beaches [Sherman, 2019; Xia, 2020]. Most beach contamination advisories are issued due to elevated levels of fecal indicator bacteria, but elevated nutrient levels in the water from such runoff can also lead to harmful algal blooms, which can be toxic [Devine, 2014; Monterey Bay National Marine Sanctuary, 2019; Xia, 2020]. Millions of beachgoers are thought to be sickened by beach-induced illness each year [Sherman, 2019]. Beach closures therefore have a significant impact on the local economy, as vacationers spend \$44 billion yearly (\$10 billion in California alone) on trips to the coast, or \$35 per person per day [Devine, 2014; Monterey Bay National Marine Sanctuary, 2019]. Understanding the surf zone-plume interactions is therefore key to forecasting when beach closures may be necessary.

Our ability as a society to manage beaches and fisheries is therefore impacted by our lack of understanding of surf zone-plume interactions. Most river plume studies have focused on larger rivers that bypass the surf zone with engineered channels, while surf zone studies have typically examined areas with little freshwater input. Wave breaking is an omnipresent source of both momentum and energy in the nearshore environment, and two recent studies show that wave breaking greatly influences river plume dynamics and mixing in the surf zone

Figure 1.1: An aerial image of the Quinault River mouth, taken on April 28. 2017, using an unmanned aerial system (UAS) as part of the 2017 observational program.

[Wong et al., 2013; Rodriguez et al., 2018]. A somewhat larger number of studies have shown weaker wave breaking impacts farther offshore on larger river plumes [Gerbi et al., 2013b; Thomson et al., 2014; Gerbi et al., 2015b; Akan et al., 2017b; Kastner et al., 2018].

This dissertation aims to expand current knowledge of surf zone-plume interactions through the use of observational data from the mouth of the Quinault River and synthesize findings from this novel dataset with previous work on wave-plume interaction across spatial scales. The remainder of this chapter provides basic background information on river plumes (section 1.2) and wave processes (section 1.3), as well as wave-plume interaction (section 1.4).

1.2 River plume mixing and dynamics

River plumes are commonly delineated into dynamical regions [Horner-Devine et al., 2015], which will be more thoroughly examined below. The plume begins where an outflow enters ambient coastal water. The momentum and buoyancy of this outflow are controlled by upstream dynamics, either directly by the river discharge, or by the presence of an estuary [Geyer and MacCready, 2014]. As the river water propagates onto the shelf, it spreads, thins, and mixes intensely in the near field region (figure 1.2).

Near field plume dynamics can be strongly modulated by tidal processes [Horner-Devine et al., 2015]. Tidal variability in the river mouth freshwater flux has a strong influence on the salinity and velocity structure of the plume, with higher horizontal velocity (u and v) and lower salinity (and therefore density, ρ) associated with ebb tide while lower velocity and higher salinity are associated with flood tide [Horner-Devine, 2009; Kilcher and Nash, 2010; Kilcher et al., 2012; Jurisa et al., 2016]. The pulse of fast moving freshwater released on ebb tide may form a front (spatial discontinuity of salinity and velocity) at the edge of the near field. As the ebb pulse wanes, the front weakens, and the plume may recirculate and/or propagate down the coast in the direction dictated by earth's rotation.

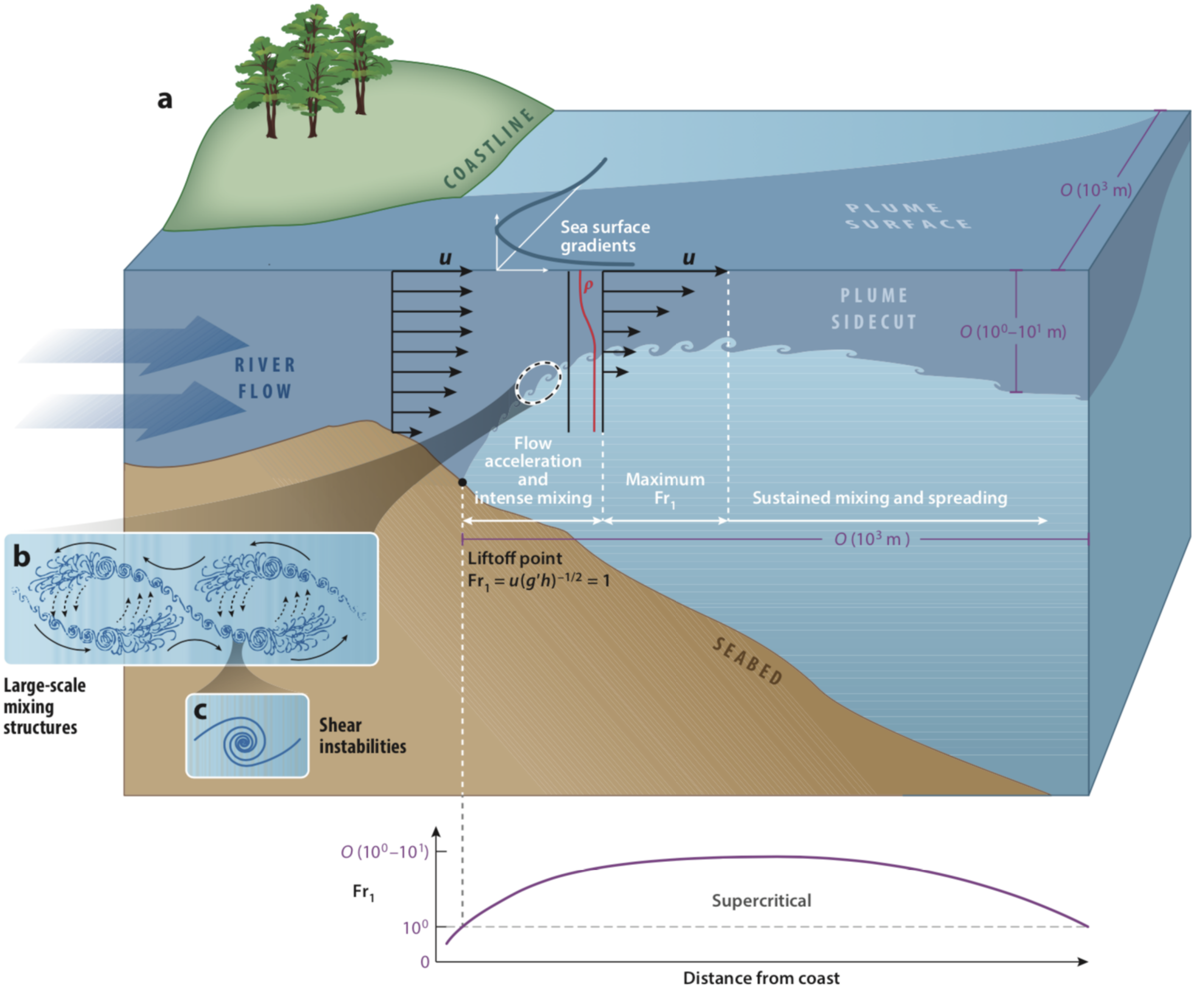

Figure 1.2: A schematic of the near field river plume from Horner-Devine et al. [2015]. Panel (a) shows the plume structure, with darker colors indicating the fresher plume layer. Profiles of density, velocity, and sea surface height show the relevant dynamics, with the cross-shroe structure of the upper layer Froude number Fr_1 shown on the bottom axis. Panels (b) and (c) show the shape of turbulent structures associated with mixing due to stratified shear instability.

1.2.1 River plume mixing

Stratified shear instability has been shown to be the dominant mechanism for river plume mixing [MacDonald and Geyer, 2004; MacDonald et al., 2007; Horner-Devine et al., 2015; Jurisa et al., 2016]. Mixing is possible when velocity shear becomes high enough to overcome stratification, as characterized by the Richardson number,

$$
\begin{aligned}
Ri &= \frac{N^2}{S^2}, \text{ where} && (1.1)\\
N &= \sqrt{\frac{-g}{\rho_0}\frac{\partial \rho}{\partial z}}, \text{ and} && (1.2)\\
S &= \sqrt{\left(\frac{\partial u}{\partial z}\right)^2 + \left(\frac{\partial v}{\partial z}\right)^2}; && (1.3)
\end{aligned}
$$

N is the Brunt-Vaisala frequency and S is the velocity shear. The Richardson number represents the relative importance of stabilizing stratification to destabilizing shear, or potential energy to kinetic energy. The onset of mixing therefore begins when Ri drops below a critical value, $Ri_c = 1/4$, as at this point the shear is strong enough to overcome stable stratification [Gregg, 2004; Geyer et al., 2010, 2017].

Mixing of fresh river water and salty ambient ocean water results in a change in density. The density difference between river and ambient water is mostly driven by the difference in salinity between the two water masses, and so the evolution of the salinity field is an important indicator of mixing. The salinity field evolution is described by

$$\frac{\partial S}{\partial t} + \vec{u} \cdot \nabla S = \nabla(K \cdot \nabla S), \tag{1.4}$$

where S is salinity, $\vec{u}$ is the three-dimensional velocity vector, and K is the eddy diffusivity of salt (hereafter referred to as simply the eddy diffusivity, dropping the "of salt"). The time derivative term on the left hand side of equation 1.4 is the local change in salinity, the spatial gradient term is the advection of salinity gradients by the velocity field, and the right hand side is a parameterization of the salt flux divergence using the eddy diffusivity.

River plume mixing has been shown to be a primarily vertical process due to the small aspect ratio (depth/width) of most plumes [MacDonald and Geyer, 2004; Chen and Mac-

Donald, 2006; McCabe et al., 2008; Horner-Devine et al., 2015]. Since lateral mixing is small, equation 1.4 reduces to

$$\frac{\partial S}{\partial t} + \vec{u} \cdot \nabla S = \frac{\partial}{\partial z} K_z \frac{\partial S}{\partial z}, \tag{1.5}$$

where K_z is the vertical eddy diffusivity. This simpler equation relates temporal and advective salinity changes to only the vertical gradient of the vertical salt flux. The salt flux is related to the buoyancy flux $\mathcal{B}$ such that

$$\mathcal{B} = \frac{g}{\rho_0} \beta \langle S'w' \rangle, \text{ where the salt flux is} \tag{1.6}$$

$$\langle S'w' \rangle = K_Z \frac{\partial S}{\partial z}. \tag{1.7}$$

Above, $\beta = \partial\rho/\partial S = 0.77 \times 10^{-3}$ kg m^{-3} psu^{-1}, w is the vertical velocity, the prime superscript denotes a turbulent fluctuation, and angle brackets denote Reynolds' averaging. In the Lagragian reference frame (following a water parcel), the unsteady and advective change terms on the left hand side of equation 1.5 combine, yielding

$$\frac{g\beta}{\rho_0} \frac{DS}{Dt} = \frac{\partial \mathcal{B}}{\partial z}, \tag{1.8}$$

where the notation D/Dt indicates the materal derivatve. Taking the mixing efficiency for stratified shear flow to be $\Gamma = \frac{\mathcal{B}}{\varepsilon} = 0.2$ [Gregg et al., 2018], the buoyancy flux is directly proportional to the TKE dissipation rate ε, which can reach $\varepsilon \sim \mathcal{O}(10^{-3})$ W/kg in river plume environments [Nash and Moum, 2005a; MacDonald et al., 2007; Jurisa et al., 2016]. Note that $\Gamma = 0.2$ may not hold for mixing driven by wave breaking turbulence.

1.2.2 River plume dynamics

Near the river mouth, river plume behavior is governed by the momentum and buoyancy of the outflow, which can be tidally variable [Garvine and Monk, 1974; O'Donnell, 1990; Hetland, 2010; Geyer and MacCready, 2014; Horner-Devine et al., 2015]. The outflow buoyancy flux can be characterized as $g'Q$, where Q is the river discharge and the reduced gravity is $g' = g\Delta\rho/\rho_0$, with $\Delta\rho$ being the difference between the outflow density and the offshore density and ρ_0 being a reference density [Fischer, 1972; Jirka, 1982; Hetland, 2010]. The outflow momentum flux can be characterized as uQ, where u is the river mouth velocity, which can vary due to processes unrelated to the discharge, such as the tide [Fischer, 1972; Jirka, 1982; Hetland, 2010].

In the plume near field, the streamwise momentum balance is between the pressure gradient and the interfacial shear stress divergence, eventually resulting in deceleration away from the river mouth [Garvine, 1987; McCabe et al., 2009; Kilcher et al., 2012]. The high momentum causes the plume layer to be supercritical, such that the upper layer Froude number

$$Fr_1 = \frac{u}{\sqrt{g' h_p}}, \tag{1.9}$$

where h_p is the plume layer depth, is larger than unity throughout the near field [Hetland, 2010]. The stream-normal momentum balance is typically between Coriolis, the pressure gradient, and interfacial shear stress divergence [Garvine, 1987; Chen et al., 2009; McCabe et al., 2009]. Spreading caused by the stream-normal momentum balance and stream-normal variability in the streamwise momentum balance leads to acceleration, as plume water moves faster through a shallower layer. This increased velocity leads to increased shear, which in turn lowers Ri, leading to mixing. As a result of mixing, the plume layer thickens, leading to a deceleration and a decrease in shear, increasing Ri (potentially about critical) [MacDonald et al., 2007; Hetland, 2010; Kastner et al., 2018]. In this way, Ri is always near its critical value, as is expected in cases of marginal instability [Smyth et al., 2019].

At the offshore edge of the near field region, a front can form. Lateral density gradients across the plume front are often large [Garvine and Monk, 1974; Garvine, 1984; Kilcher and Nash, 2010]. The front propagates at the speed of a buoyant gravity current, so that at the front $Fr_1 = 1$. Thus, if the velocity in the near-field is higher than the characteristic internal wave speed associated with its stratification, $c = \sqrt{g' h_p}$, plume water will catch up to the front, causing convergence and downwelling [Garvine and Monk, 1974; Horner-Devine, 2009; Kilcher and Nash, 2010; Thomson et al., 2014]. Conversely, if the velocity onshore of the front becomes less than c, the front is free to propagate at its characteristic speed, detaching from the plume as an internal wave [Nash and Moum, 2005a; Kilcher and Nash, 2010; Cole et al., 2020].

Far from the river mouth, plume water propagates along the coast as a buoyant coastal current at a speed close to c [Rennie et al., 1999; Marmorino and Trump, 2000]. These speeds are typically less than 1 m/s, leading to lower shear and higher Ri in the far field than in the near field. The far field plume is therefore less susceptible to mixing along its base due to shear from its own momentum than the near field plume. Mixing in the far field therefore tends to be predominantly due to external forcing, such as wind [Fong and Geyer, 2001; Lentz, 2004; Lentz and Largier, 2006; Fisher et al., 2018].

1.3 Wave properties and wave breaking

Surface gravity waves can traverse vast swathes of ocean from their generation to the moment they break. Linear wave theory, wave breaking mechanisms, and the turbulence generated by wave breaking will be more thoroughly examined below. Linear wave theory, where wave slopes are assumed to be small, does reasonably well at approximating wave dynamics in most environments (section 1.3.1). Waves break as they reach a limiting steepness, causing energetic turbulence 1.3.2. Waves over-steepen and break for different reasons in deep and shallow water. In deeper water, steepening and breaking can be caused by excess energy input from the wind into the waves or wave-current interaction. Wave shoaling due to energy flux conservation as depth decreases close to shore causes also increasing steepness and breaking. This process typically occurs in the surf zone, where waves break near shore.

1.3.1 Surface gravity wave basics

Entire textbooks have been written on the basic dynamics of surface gravity waves (Dean and Dalrymple [1984] and Mei [1989] among others), so I will present here only what is necessary to understand the work presented in section 1.4 and chapters two, three and four. Linear surface gravity names owe their name to the “linearization” of the free surface boundary condition in the surface gravity wave derivation: the free surface is approximated as the mean sea surface instead of the wave-following surface.

Surface gravity waves are typically wind-generated, caused by the "piling up" of water by the wind, forming a sea surface perturbation. The wave height, H, is the distance from crest to trough (twice the amplitude of a sinusoidal oscillation). Wave propagation depends on the frequency (radial ω or cyclic f), $\omega = 2\pi f = 2\pi/T$, wavenumber, $k = 2\pi/\lambda$, and the water depth, d, where the wave period and wavelength are notated by T and λ, respectively. The dispersion relation connects these properties:

$$\omega^2 = gk \tanh kd. \tag{1.10}$$

The dispersion relation has deep and shallow water limits, as kd approaches infinity or zero, respectively. This work mostly discusses shallow water, where the small angle approximation reduces equation 1.10 to

$$\omega^2 = gk^2 d \tag{1.11}$$

The wave phase speed c, and wave group velocity c_g, are given by:

$$c = \frac{\omega}{k} \approx \sqrt{gd} \text{ in shallow water, and} \tag{1.12}$$

$$c_g = \frac{\partial \omega}{\partial k} \approx \sqrt{gd} \text{ in shallow water.} \tag{1.13}$$

The shallow water limits of c and c_g are the same. The phase speed indicates the propagation speed of wave crests, while the group velocity indicates the propagation of wave energy.

Wave energy E is related to wave height squared, and is best defined using spectral analysis. The ocean surface gravity wave field is typically heterogeneous in height, frequency, and direction (although I will not go into detail about directional spectra in this work). Using spectral analysis, specifically the Fourier transform, complex wave fields are represented as a sum of linear sinusoidal oscillations, with different amplitudes and frequencies. The spectral wave energy at each frequency can be used to calculate a representative wave height H_S for the heterogeneous wave field,

$$H_S = 4\sqrt{\int E(f)df} = 4\sigma_\eta, \tag{1.14}$$

where $\sigma_\eta = \sqrt{\int E(f)df}$ is the standard deviation of the sea surface displacements. H_S is refered to as the "significant wave height", and represents the average wave height of the largest 1/3 of the wave field. Wave energy can then be defined as

$$E = \frac{1}{16}\rho g H_S^2 \tag{1.15}$$

The significant wave height is related to the root mean square wave height H_{rms} by $H_S = \sqrt{2}H_{rms}$. In general, wave heights follow the Rayleigh distribution, such that the probability of a given wave being higher than some height $\hat{H}$ is given by

$$P(H \geq \hat{H}) = e^{-(H/H_{rms})^2}. \tag{1.16}$$

A representative frequency for a heterogenous wave field can be taken as either the peak wave frequency f_p (or period T_p), associated with the mode of the wave energy spectra, or the energy weighted average wave frequency, f_e (or period T_e). The wave energy flux F, a conservative property, is defined as $F = Ec_g$, which depends on wave height, frequency, wavenumber, and water depth. In shallow water,

$$F = \frac{1}{16}\rho g^{3/2} d^{1/2} H_S^2, \tag{1.17}$$

which only depends on wave height and water depth. F can be increased by a source of wave energy, such as the wind, and decreased by a sink of wave energy, such as dissipation due to wave breaking.

The velocities associated with the propagation of linear surface gravity waves are referred to as orbital velocities, as they cause no net particle displacement (they are closed orbits). Therefore, linear waves do not have their own momentum in the Eulerian (fixed) reference frame. These orbital velocities decay in depth, leading to a simple Lagrangian (and nonlinear) mechanism for wave-induced momentum known as Stokes' drift [Stokes, 1847; Lentz et al., 2008]. Nonlinear wave dynamics take the free surface boundary condition as the wave-following surface, resulting in larger orbital velocity and particle displacements occurring higher in the water column as a particle moves around its orbit. The resulting velocity is typically small ($\mathcal{O}(10^{-2})$ m/s), but can be significant over the inner shelf [Lentz et al., 2008; Kumar et al., 2012; Lentz and Fewings, 2012].

The primary mechanism for wave induced momentum considered in this work are gradients in the wave flux of momentum, known as the "radiation stress". A series of seminal papers on the subject by Longuet-Higgins and Stewart shows the detailed derivation of this quantity from basic linear wave theory and several of its applications [Longuet-Higgins and Stewart, 1960, 1961, 1962, 1964; Longuet-Higgins, 1970]. Surface gravity waves propagate laterally, and can therefore flux momentum in the x (typically cross-shore) and y (typically alongshore) directions. Momentum, in turn, can act in either the x or y directions, so the radiation stress is a second order tensor of form

$$\mathcal{S} = \begin{bmatrix} S_{xx} & S_{xy} \\ S_{yx} & S_{yy} \end{bmatrix} = E \begin{bmatrix} n(\cos^2\theta + 1) - \frac{1}{2} & \frac{n}{2}\sin 2\theta \\ \frac{n}{2}\sin 2\theta & n(\sin^2\theta + 1) - \frac{1}{2} \end{bmatrix}, \tag{1.18}$$

where θ is the wave direction and $n = c_g/c$. A negative radiation stress gradient represents a decrease in the wave flux of momentum, functioning as a source of momentum to the surrounding ocean, while a positive radiation stress gradient represents an increase in the wave flux of momentum, functioning as a sink of momentum from the surrounding ocean.

1.3.2 Wave breaking

Waves break as they reach either a limiting steepness or water depth. Steepness limitation is described by the classic Miche [1944] formulation,

$$\frac{H}{L} \leq \frac{1}{7}\tanh kd, \tag{1.19}$$

where 1/7 is the theoretical maximum wave steepness in deep water. If the wind input of energy to the waves is sufficiently high, waves can reach this limiting steepness and break in a process known as whitecapping.

Steepness limited breaking can also be induced by wave-current interaction. The presence of a current, $\vec{u}$ alters the dispersion relation (eq. 1.10) such that

$$\omega = \sqrt{g|k| \tanh |k| d} + \vec{u} \cdot \vec{k}, \tag{1.20}$$

where the wavenumber vector $\vec{k}$ indicates the direction of wave propagation. For a given frequency, this leads to longer waves when the current and waves are parallel (following currents), and shorter waves when the current and waves are antiparallel (opposing currents). A wave that propagates from ambient water across a river plume front, encountering an opposing current, will therefore shorten but maintain its height, potentially causing the wave to oversteepen and break [Kirby and Chen, 1989; Booij et al., 1999; Thomson et al., 2014; Zippel and Thomson, 2015, 2017].

In shallow water, waves break at a depth proportional to their height. This is expressed as a critial value of the quantity $\gamma = H_S/d$. For a soliton, $\gamma = 0.781$, but in the field, a range of $0.3 < \gamma < 0.7$ is commonly reported [Raubenheimer et al., 1996]. The region onshore of the the breaker depth is called the surf zone. In a “saturated” surf zone where depth monotonically increases in the offshore direction, a constant value of γ is maintained, such that H_S decreases throughout the surf zone and goes to zero at the shoreline. This causes a negative cross-shore radiation stress gradient.

The surf zone is very energetic. This is due to the pressure gradients and currents caused by radiation stress gradients and other processes driven by constant wave breaking. The cross-shore gradient $\partial S_{xx}/\partial x$ causes water to pile up closer to shore, creating a cross-shore pressure gradient known as “setup”. Alongshore differences in setup due to bathymetric variability can lead to alongshore pressure gradients, which in turn cause offshore flow in bathymetrically driven rip currents. The cross-shore gradient $\partial S_{xy}/\partial x$ induces a mean alongshore current in the surf zone which can be energetic ($\sim 0.5 - 1$ m/s) [Longuet-Higgins, 1970; Thornton and Guza, 1986]. Other significant processes include the creation of vertical vorticity by short crested breaking waves, leading to transient rip currents that form from convalescing vortex dipole structures [Clark et al., 2012; Hally-Rosendahl et al., 2014; Kumar and Feddersen, 2017a,b]. Other than rip currents, which are spatially sparse, cross-shore circulation in the surf zone is fairly weak, leading the surf zone to be retentive [MacMahan et al., 2004; Kumar et al., 2012; Lentz and Fewings, 2012; Hally-Rosendahl et al., 2014].

Turbulence is large in the surf zone due to consistent wave breaking driving large gradients in wave energy flux. The maximum resultant TKE dissipation rates are higher than in river plumes, $\varepsilon \sim \mathcal{O}(10^{-2})$ W/kg, reaching these values near the water surface and at the break point [Thornton and Guza, 1986; Feddersen and Trowbridge, 2005a; Feddersen, 2012b; Thomson, 2012]. This energetic turbulence typically leads to minimal surf zone stratification [Feddersen and Trowbridge, 2005a; Lentz et al., 2008; Kumar and Feddersen, 2017b].

1.4 Wave breaking effects on river plumes

The effects of wave breaking on river plume dynamics and mixing depend on the plume region and the type of breaking. Recent work has focused on three main types of wave-plume interactions: depth limited breaking in the surf zone near the river mouth [Wong et al., 2013; Rodriguez et al., 2018; Kastner et al., 2019], wave-current interaction in the near field [Akan et al., 2017b; Kastner et al., 2018], and whitecapping in the far field [Gerbi et al., 2013b, 2015b],.

Studies of river outflows in the surf zone have sought to determine the mechanisms by which river water can escape the region's strong wave forcing. If river forcing is larger than wave forcing, then the river water should be able to propagate out of the surf zone and onto the inner shelf. In the cross-shore, the relevant dynamics are encapsulated by the relationship of the river momentum flux, $\rho u^2 h$ (where u is the river mouth velocity and h is the river mouth depth), and the wave radiation stress, S_{xx}. When $u^2 h > S_{xx}$, Rodriguez et al. [2018] show using a numerical model that more river water escapes onto the shelf. An analogous approach uses the characteristic length scale of the plume near field, L_{NF}, and the surf zone width, L_{SZ}, in a similar manner. Using drifter-based observations, Kastner et al. [2019] show that when $L_{NF} > L_{SZ}$, river water is more likely to escape onto the inner shelf (chapter 2 of this dissertation). While Rodriguez et al. [2018] use an idealized numerical model run to steady state and the observations of Kastner et al. [2019] (chapter 2) show considerable influence of bathymetry and tidal processes, these results are mostly in agreement. They also show that the relationship between river and wave forcing results in a probability of river water escape or a percentage of escaped discharge, not a binary "escape or trap" outcome.

A river outflow in the surf zone can also be influenced by alongshore surf zone dynamics. If the surf zone alongshore current generated by $\partial S_{xy}/\partial x$ is large compared to the river outflow, river water can be trapped [Wong et al., 2013]. This is expressed by the relationship of the crossflow length scale, L_a, to the surf zone width, L_{SZ}. The crossflow length scale characterizes how much the river outflow will turn based on the momentum of the river outflow and the alongshore current speed. Using observations of dye concentration and a numerical model, Wong et al. [2013] show that as L_{SZ} increases relative to L_a (increased wave forcing relative to river forcing), more river water is trapped in the surf zone. This is similar to the results from Rodriguez et al. [2018] and Kastner et al. [2019], as higher wave forcing traps more river water in the surf zone. The importance of the alongshore current in this mechanism indicates that the fate of river water in the surf zone can be influenced by more than just cross-shore dynamics.

When wave breaking is due to steepness limitation rather than depth limitation, river plume dynamics are less severly impacted. Wave-driven momentum in deeper water can play a role in altering the stream-normal plume momentum balance, but does not significantly alter plume dynamics by itself [Akan et al., 2017b; Kastner et al., 2018]. The turbulence caused by current-induced wave breaking at the plume front, however, may contribute to frontal mixing [Thomson et al., 2014]. In the far-field, wave-driven mixing has been shown to alter plume structure by deepening the plume layer more than would be expected due only to wind driven mixing [Gerbi et al., 2013b]. This is due to the high near surface TKE from wave breaking turbulence [Gerbi et al., 2013b]. Several of these studies suggest that wave breaking can elevate plume mixing when the ratio of H_S/h_p is large. Observations from the Quinault River presented in chapter 2 suggest that this is also the case in the surf zone.

1.5 Outline

This dissertaton uses data from an observational field campaign at the mouth of the Quinault River to assess the fate of river water in the surf zone by answering the following two-pronged question: *Where does river water go in the presence of surf zone wave forcing, and how fresh is it when it gets there?* Each of these questions receive attention in a chapter of this dissertation, and they are interpreted together in another chapter, as described below.

Chapter 2 uses observations of drifter behavior at the Quinault River mouth in the context of mooring measurements of river and wave forcing to develop an understanding of when river water is likely to escape the surf zone. The results show that tidal variability of river forcing and the surf zone width, along with bathymetric variability, play a key role in determining the likelihood of river water escape. This chapter is reproduced with minor changes from:

> S. E. Kastner, A. R. Horner-Devine, and J. M. Thomson. A conceptual model of a river plume in the surf zone. *Journal of Geophysical Research: Oceans*, 124(11):8060–8078, 2019. doi: 10.1029/2019JC015510.

Chapter 3 uses a case study from one day of drifter and mooring data at the Quinault River mouth to assess the dependencies of mixing in the surf zone. A conceptual framework is developed for the removal of freshwater from near the river mouth, which increases stratification in the near-surface, elevating wave-driven mixing. This chapter is being prepared for submission to the *Journal of Physical Oceanography* as:

> S. E. Kastner, A. R. Horner-Devine, and J. M. Thomson. Observations of river plume mixing and transport in the surf zone. *Journal of Physical Oceanography*, in prep.

Chapter 4 summarizes the dissertation and discusses its implications. The chapter addresses how observed river water behavior at the Quinault River mouth might interact with general surf zone circulation, discusses the utility of scaling wave-driven river plume mixing as the ratio H_S/h_p, and points toward further work that could be done on these subjects.

Chapter 2

A CONCEPTUAL MODEL OF A RIVER PLUME IN THE SURF ZONE

2.1 Introduction

Small freshwater discharges represent an important source of sediment, nutrients, and pollutants to the coastal ocean. Relative to their discharge, such rivers export proportionally more sediment to the coastal ocean, as they often lack deltas that sequester sediment [Milliman and Syvitski, 1992]. The net effect of the export of sediment, nutrients, and pollutants from small rivers can be especially large in the mid-latitudes, where small rivers comprise a large fraction of total river discharge to the coastal ocean [Izett and Fennel, 2018].

Most studies of coastal plumes have focused on large river sytems and our understanding of small river plumes is poor [Garvine, 1977; MacDonald and Geyer, 2004; Kilcher et al., 2012; Horner-Devine et al., 2015]. The interaction of plume dynamics with surf zone processes is a key component in the dynamics of small river discharges. Recent studies have shown that the relative importance of river plume momentum and alongshore or cross-shore surf zone dynamics can determine the fate of river water that flows into the surf zone [Wong et al., 2013; Rodriguez et al., 2018].

Small river mouths are often unengineered, allowing surf zone wave breaking to occur near or at such outflows. In regions with higher population densities, engineered structures such as jetties are present at most river mouths, preventing wave breaking and the influence of surf zone dynamics on buoyancy and momentum-driven river plume processes [Clark et al., 2010; Hally-Rosendahl et al., 2014; Horner-Devine et al., 2015].

2.1.1 Surf zone processes

Wave breaking is the dominant driver of physical processes in the surf zone, where waves break near the shore as a result of depth limitation. Depth-limited breaking occurs at a critical value of $\gamma = \frac{H_S}{d}$, where H_S is the significant wave height and d is depth [Miche, 1944]. Theoretical work finds that for a solitary wave, $\gamma = 0.781$, while observational studies have found that random waves have a range $0.3 < \gamma < 0.6$ [Miche, 1944; Raubenheimer et al., 1996; Janssen and Battjes, 2007]. Breaking waves lose radiation stress (i.e., the momentum flux associated with the waves), and the resulting momentum drives nearshore currents and coastal setup [Longuet-Higgins and Stewart, 1961, 1962; Longuet-Higgins, 1970]. Breaking waves are also a significant source of turbulence near the ocean surface, especially in the surf zone, where near-surface values of dissipation rate reach $\varepsilon \approx 10^{-2}$ $\mathrm{m^2/s^3}$ [Thornton and Guza, 1983; Feddersen and Trowbridge, 2005a; Feddersen, 2012b; Thomson, 2012].

Transport of freshwater from a river entering the surf zone could be reasonably expected to be influenced by surf zone circulation processes, as has been shown for passive tracers [Clark et al., 2010; Hally-Rosendahl et al., 2014; Brown et al., 2015]. The strongest surf zone circulation is driven in the alongshore direction by obliquely directed breaking waves [Longuet-Higgins, 1970; Feddersen et al., 1998]. The cross-shore circulation, relevant for exchange between the surf zone and the inner shelf, is generally weak [MacMahan et al., 2004; Reniers et al., 2009; Clark et al., 2010; Hally-Rosendahl et al., 2014]. Exceptions are rip currents, which can generate significant exchange between the surf zone and the inner shelf [Haller et al., 2002; Clark et al., 2010; Hally-Rosendahl and Feddersen, 2016; Kumar and Feddersen, 2017a]. Other cross-shore mechanisms for transport are Stokes' drift (onshore lagrangian motion) and undertow (offshore return flow). [Stokes, 1847; Fewings et al., 2008]. Wave-driven alongshore currents are therefore a likely transport mechanism for surf zone freshwater, with cross-shore flow being of secondary importance (excepting rip currents).

2.1.2 River plume processes

Coastal river discharges are a significant driver of cross-shelf transport of freshwater and river-borne material, which has motivated significant efforts to understand and model their dynamics. In the near-field of river plumes, the dynamics are governed by the outflow momentum and buoyancy [Garvine and Monk, 1974; O'Donnell, 1990; Hetland, 2010; Horner-Devine et al., 2015] and are typically described using the upper layer Froude number, $Fr_1 = \frac{u}{\sqrt{g' h_p}}$. Here u is the upper layer velocity, $g' = \frac{g\Delta\rho}{\rho_0}$ is the reduced gravity associated with the plume stratification, $\Delta\rho$, and h_p is the plume layer depth. The plume near-field is considered to be the region where momentum effects dominate over buoyancy effects and so the upper layer is supercritical ($Fr_1 > 1$) [Garvine, 1977; Hetland, 2010; Horner-Devine et al., 2015]. Eventually, mixing causes the upper layer Froude number to drop and the near-field ends where $Fr_1 = 1$ [Luketina and Imberger, 1987; McCabe et al., 2008; Hetland, 2010]. Beyond this point, plume dynamics are strongly influenced by buoyancy, and are characterized in terms of the gravity current speed, $u_{gc} = \sqrt{g'h_p}$, as well as local wind forcing and earth′s rotation.

Mixing influences the upper layer Froude number through the entrainment of high-density, low-momentum ambient water due to shear-driven turbulence. Mixing is characterized as a density flux through the base of the plume $\rho_e w_e$, where ρ_e is the entrained density and w_e is the entrainment velocity [MacDonald and Geyer, 2004; McCabe et al., 2008; Hetland, 2010]. Plume entrainment is often parameterized in terms of the local bulk Richardson number, Ri_b [Ellison and Turner, 1959; Christodoulou, 1986; Yuan and Horner-Devine, 2013]. This relationship varies over different regimes of Ri_b, but the normalized entrainment velocity $\delta = w_e/u$ is generally dependent on Ri_b. The inflow bulk Richardson number, $Ri_{b0} = \frac{g_0' h_0}{u_0^2}$, best characterizes this functionality such that $\delta = aRi_{b0}^{-1/2}$, where $a \approx 0.02$ and the subscript 0 indicates that the bulk Richardson number is evaluated at the river mouth [Christodoulou, 1986; Yuan and Horner-Devine, 2013]. Calculations of normalized entrainment vary between $3 \times 10^{-3} < \delta < 6 \times 10^{-2}$, with field studies [MacDonald and Geyer, 2004] reporting lower values than laboratory studies [Ellison and Turner, 1959; Yuan and Horner-Devine, 2013]. Field observations of turbulent kinetic energy dissipation associated with plume entrainment vary between $10^{-5} < \varepsilon < 10^{-3}$ W/kg [MacDonald and Geyer, 2004; Kilcher et al., 2012; Jurisa et al., 2016].

2.1.3 Wave-plume processes

Most previous studies of the interactions of river plume and wave dynamics have focused on large river plumes. The results of numerical model studies show that turbulence due to wave breaking increases mixing in the far field surface plume layer [Gerbi et al., 2013b, 2015b]. Elevated mixing has also been observed at the offshore front of the Columbia River plume, where strong, sheared currents lead to wave blocking and breaking due to steepness limitation. The turbulence resulting from this wave breaking is scaled by a gradient in wave energy flux across the front, and could be downwelled to the base of the plume layer by frontal convergence [Thomson et al., 2014; Zippel and Thomson, 2017]. In the near field of large river plumes, wave effects are less clear. Stokes' drift causes modest advection (hundreds of meters) of the Columbia river plume [Akan et al., 2017b]. Large plume depths relative to wave heights in the Fraser River plume shield the plume from mixing due to breaking wave-driven turbulence [Kastner et al., 2018].

At New River Inlet, NC, an unengineered tidal inlet, depth-limited wave breaking is enhanced by the presence of an opposing tidal current, causing waves to steepen and break [Zippel and Thomson, 2015]. Preferential breaking can occur on either side of the inlet mouth, away from the deeper channel, forcing a rip-current like circulation that enhances offshore tidal velocities out of the inlet [Olabarrieta et al., 2014].

Rodriguez et al. [2018] show that for an idealized small river entering a surf zone, the percentage of freshwater that remains in the surf zone is related to the ratio of river momentum flux to wave momentum flux. When wave momentum flux dominates, freshwater remains in the surf zone, and mixes minimally. When river momentum flux dominates, most freshwater escapes the surf zone and exhibits normal river plume behavior on the shelf, with some freshwater remaining trapped in the surf zone. Wong et al. [2013] show that surf zone trapping of dye released in the mouth of a small creek emptying into the surf zone is determined by the degree to which the creek outflow is turned by wave-driven forcing. When the outflow is significantly turned by wave-driven currents, it is trapped in the surf zone, while a straighter outflow can result in river water reaching the inner shelf. This finding is analogous to that of Rodriguez et al. [2018] in that alongshore wave-driven currents are stronger (for a constant wave angle) when wave forcing is stronger. Rodriguez et al. [2018] and Wong et al. [2013] thus show that wave forcing can trap a small river plume in the surf zone by controlling the cross-shore momentum flux balance, or by turning the plume with strong alongshore currents.

2.1.4 Conceptual model framework

In this work we propose that the dynamics of a river plume in the surf zone can be understood in terms of the relative magnitudes of three length scales that characterize the governing processes in this interaction: the surf zone width, L_{SZ}; the near-field plume length, L_{NF}; and the channel length, L_C.

The surf zone width, L_{SZ}, is a function of the offshore significant wave height, local bathymetry, and the local critical value of γ. L_{SZ} represents the cross-shore distance over which wave breaking occurs, causing a radiation stress gradient.

Hetland [2010] defines the near-field plume length, L_{NF} based on the plume momentum $M = u_0 Q$, buoyancy $B = g'Q$, and nondimensional entrainment δ, where u_0 is the river mouth velocity, Q is the river discharge, and g' is a measure of the density difference between the river mouth and the ambient offshore water. The resulting scaling from Hetland [2010] is

$$L_{NF} = \frac{u_0^{3/2} Q^{1/4}}{g'^{1/2} w_e^{3/4}}, \tag{2.1}$$

This is a modification of the jet-to-plume length scale, which predicts the region in which the momentum of a jet, rather than its buoyancy, controls the flow [Fischer et al., 1979; Jirka et al., 1981; Jones et al., 2007]. With the inclusion of the parameter δ, Hetland [2010] shows that L_{NF} as defined by Equation 2.1 agrees well with the location where $Fr_1 = 1$. A critical assumption for the use of L_{NF} is that the plume is in steady state. In a tidally variable system, this assumption is valid providing that the time scale characterizing the near field, T_{NF}, is short compared with tidal time scales. This is evaluated in section 2.2.3.

The channel length, L_C, is the cross-shore location where the channel formed by the seaward extension of the river channel into the nearshore bathymetry is no longer deeper than the surrounding bathymetry. At a natural river mouth, sediment transport processes determine this length scale. At an engineered river mouth, the length scale is set by dredging and/or the presence of jetties.

We expect that the fate of river water will be predicted by the relative magnitude of these scales as they vary over the course of a tidal cycle. When the wave forcing is sufficiently energetic relative to the strength of the river discharge, the surf zone will be wider than the near field plume length ($L_{SZ} > L_{NF}$). In this case we anticipate that the plume loses momentum before exiting the surf zone and freshwater is trapped. If the opposite is true, the discharge penetrates through the surf zone to the inner shelf. As we will show in section 2.3.3, we observe a third mode of behavior that completes the conceptual picture. When the surf zone is narrower than the channel length ($L_{SZ} < L_C$) freshwater escapes by bypassing the wave forcing. These three modes of behavior form the conceptual model that we will test and apply in interpreting our data. They are summarized in Table 2.1.

Table 2.1: The conditions and river water behaviors associated with each conceptual mode.

Mode	Condition	Predicted Behavior
Wave dominance	$L_{SZ} > L_{NF}$ & $L_{SZ} > L_C$	River water exits the river mouth and is trapped in the surf zone by wave forcing
River dominance	$L_{NF} > L_{SZ}$	River water exits the surf zone as its momentum overcomes breaking wave forcing
Bathymetric dominance	$L_C > L_{SZ}$	River water exits the river mouth and reaches the inner shelf, largely bypassing wave forcing due to minimal wave breaking in the channel

2.2 Methods

2.2.1 Observational Setup

We made observations at the Quinault River, in Taholah, WA, between 24 April and 5 May, 2017. During the study period, the tidal range measured by the USGS Point Grenville gauge varied from 1.5 – 3 m (Figure 2.2a). The discharge at the river mouth is calculated as 1.5× the USGS measured discharge at Quinault Lake per local knowledge from the Quinault Nation Department of Natural Resources, and falls from ∼220 m^3/s to ∼110 m^3/s during the study period(Figure 2.2b). The tidally reconstructed velocity at the surface in the river mouth (see section 2.2.2) varies from ∼0.5-2 m/s (Figure 2.2c). The wave height observed by the AWAC varied from ∼1-2 m, with a mean wave angle of ∼6.5±6.2° relative to shore normal (Figure 2.2d). Offshore winds from NDBC 46041 varied from 5-10 m/s, mostly from the northwest and southeast (Figure 2.2e).

Our observational program consisted of three main components: Drifter deployments from inside the river inlet, nearshore and inlet-based moorings, and unmanned aerial system (UAS) flights from the shore.

Drifter deployments

We deployed two types of SWIFT drifters from inside the river mouth throughout each day of the study, SWIFT v3 and SWIFT v4 [Thomson, 2012; Thomson et al., 2019]. All of these SWIFTs measure wave properties using either an Inertial Measurement Unit (v3, v4) or a Global Positioning System (v3). SWIFT v4 and SWIFT v3 measure salinity and temperature using an Aanderaa 4319 CT sensor. SWIFT v3 measures either near-surface turbulence using an uplooking Nortek Aquadopp HR or a velocity profile using a downlooking Nortek Aquadopp. SWIFT v4 measures both near-surface turbulence and a velocity profile using a downlooking Nortek Signature 1000 (HR). The Signature 1000 is also used to measure water depth. The SWIFT v3 has a draft of 1.2 m, the SWIFT v4 has a draft of 0.25 m, and the μSWIFT has a draft of 0.5 m. SWIFT v3 and v4 sample in 512 second bursts every 12 minutes, such that there are 5 bursts each hour, starting on the 0, 12, 24, 36, and 48 minute marks.

The drifters were deployed from a small boat station at the center of the river channel close to the river mouth mooring (Figure 2.1). We conducted a total of 60 drifter deployments during daylight hours throughout the study period, spanning all tidal phases, a variety of

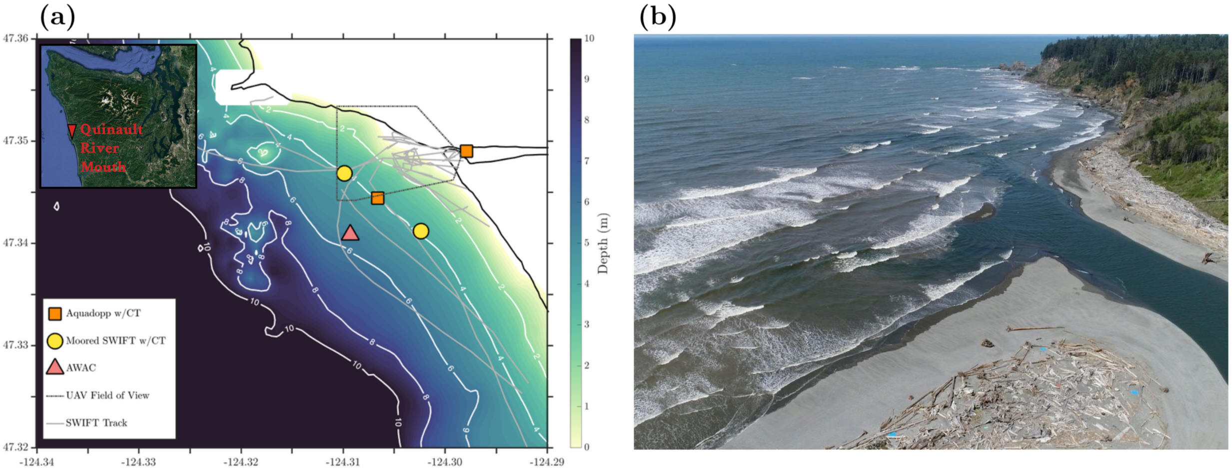

Figure 2.1: The observational field campaign at the Quinault River mouth. Panel (a) shows a map of deployed instruments and bathymetry. Color indicates depth, and isobaths are given as white lines with notations in meters. Orange squares indicate moorings using Nortek Aquadopp ADCPs, yellow circles indicate moorings using SWIFTs, and the red triangle indicates the offshore AWAC. The UAS field of view is given as a dashed-dotted black line, and SWIFT drift tracks are solid grey lines. The inset Google Earth image shows the location of the Quinault river mouth on the Washington coast. Panel (b) is an example UAS perspective image from April 28, 2017, when $H_S = 1.5$ m, $Q = 171$ m^3/s, and $\eta = 1.3$ m.

tidal amplitudes, a variety of incident wave conditions, and a twofold variation in river discharge (Figure 2.2). Drifters were deployed in staggered pairs with one released 3 minutes before the start of a given data collection burst and one released at the start of a given data collection burst. This deployment scheme maximized observations in the surf zone within the constraints of the 12-minute burst sampling scheme.

In order to qualitatively assess tidal influence on the system, we define three categories of drifter behavior: 1) escaping the surf zone, 2) nearly escaping the surf zone, or 3) remaining trapped in the surf zone (Table 2.2). Drifters that escape the surf zone transit to the inner

Table 2.2: Distribution of SWIFT deployments by behavior and type of drifter.

Drifter type	Escape	Near-Escape	Trap	Total
SWIFT v3	4	6	18	28
SWIFT v4	4	4	9	17
Total	8	10	27	45

shelf, where their trajectories are determined by the local inner shelf circulation. Drifters that nearly escape the surf zone follow river momentum nearly to the surf zone edge before losing offshore momentum, turning around to travel onshore, and beaching near the river mouth. Trapped drifters lose their offshore momentum before reaching the edge of the surf zone and beach quickly after deployment.

Moorings

We deployed five moorings: three nearshore moorings positioned at the outer edge of the surf zone in 4 m water depth, a Sea Spider tripod with a Nortek Acoustic Waves and Currents (AWAC) instrument in 6 m water depth, and a Datawell DWR-G4 buoy (telemetry wave parameters only, raw data not recorded) in 15 m water depth with a HOBO temperature sensor at 0.5 m and a HOBO PT sensor at 1.5 m. The offshore (WaveRider and Sea Spider) moorings were deployed on 24 April, while the nearshore moorings were deployed on 28 April, when wave conditions were lower. The three nearshore moorings all included two YSI 600LS CTD sensors at 1 m and 3 m below the surface, HOBO temperature sensors at 1.5 m, 2 m, and 2.5 m, and HOBO pressure/temperature (PT) sensors at 4 m below the surface. The middle mooring had a PT sensor at 2 m instead of a temperature sensor. Each nearshore mooring also included a surface following downlooking acoustic Doppler current profiler. On the north and south moorings, this was a SWIFT v4 with an integrated Nortek Signature 1000, while the middle mooring had a Nortek Aquadopp mounted on a Doppcat

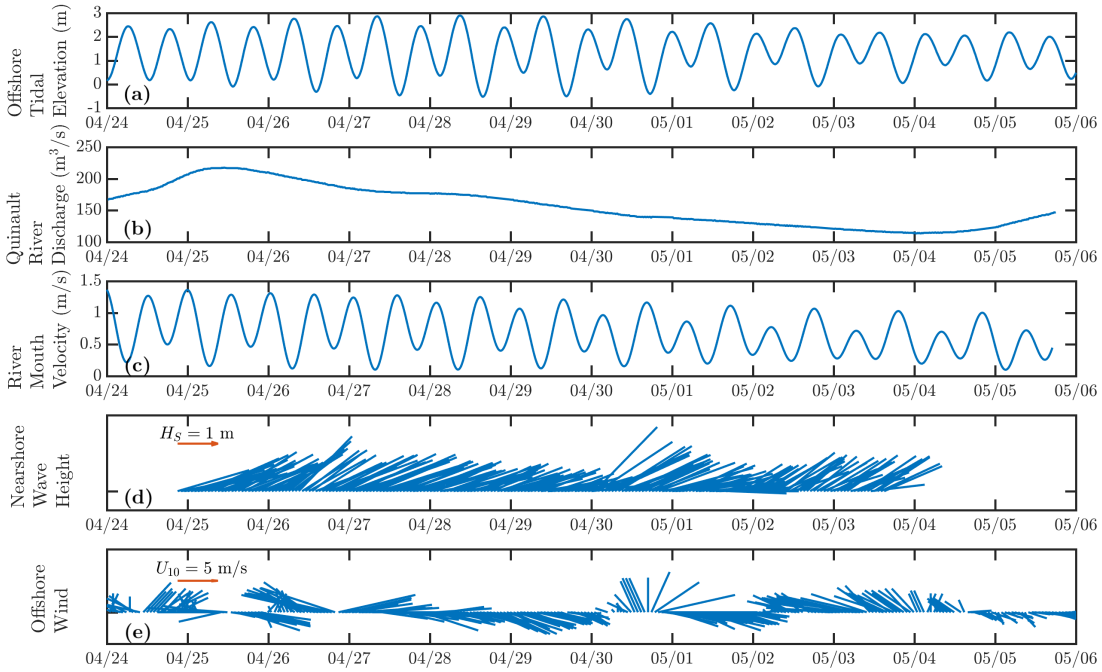

Figure 2.2: Time series of the observational period of (a) the tidal elevation at Point Grenville, (b) the modified discharge from the Lake Quinault USGS gauge, (c) the tidally interpolated river mouth velocity, (d) the AWAC wave height and direction (East to the right), and (e) the offshore wind speed and direction from NDBC 46041 (same convention as wave direction).

floatation system. All of these moorings were recovered on 3 May. The nearshore moorings were deployed progressively closer to shore southward in the array roughly following the 4 m isobath; the north mooring was ∼900 m offshore, the middle mooring was ∼750 m offshore, and the south mooring was ∼550 m offshore (Figure 2.1).

The moorings in the river inlet included a HOBO PT sensor at the dock to measure the tidal signature in the inlet, as well as a Nortek Aquadopp mounted on a Doppcat small instrumented catamaran that was deployed in the river mouth while a team was onsite during daylight hours. This Doppcat had a HOBO PT sensor attached to its anchor. The PT sensor at the dock was deployed starting 26 April and ending 5 May. These deployments captured three-quarters of a neap-spring cycle.

UAS operations

We conducted UAS flights using a DJI Phantom 4 Pro equipped with a 4k video camera near the river mouth, imaging from an altitude of approximtely 120m. These flights lasted ∼10 minutes each, including ascent and descent. We flew the UAS during daylight hours, normally concurrent with a SWIFT deployment, in order to capture video of the SWIFTs traversing the surf zone near the river mouth. We placed 5-8 ground control points (GCPs) on the bar near the river mouth in order to rectify the UAS video [Holman et al., 2017]. Twenty-eight flights were made during the study period.

2.2.2 Momentum flux calculations

River Momentum Flux

We calculate the river momentum flux, u^2h, where the velocity u is the surface river velocity immediately inside the river mouth measured with the Doppcat ADCP, and h is the river channel depth. The channel depth h is determined by combining measurements of depth from the ADCP and the dock pressure sensor. The dock depth was consistently shallower than the river mouth by 1.5 m (not shown), and so we use the more complete dock tide

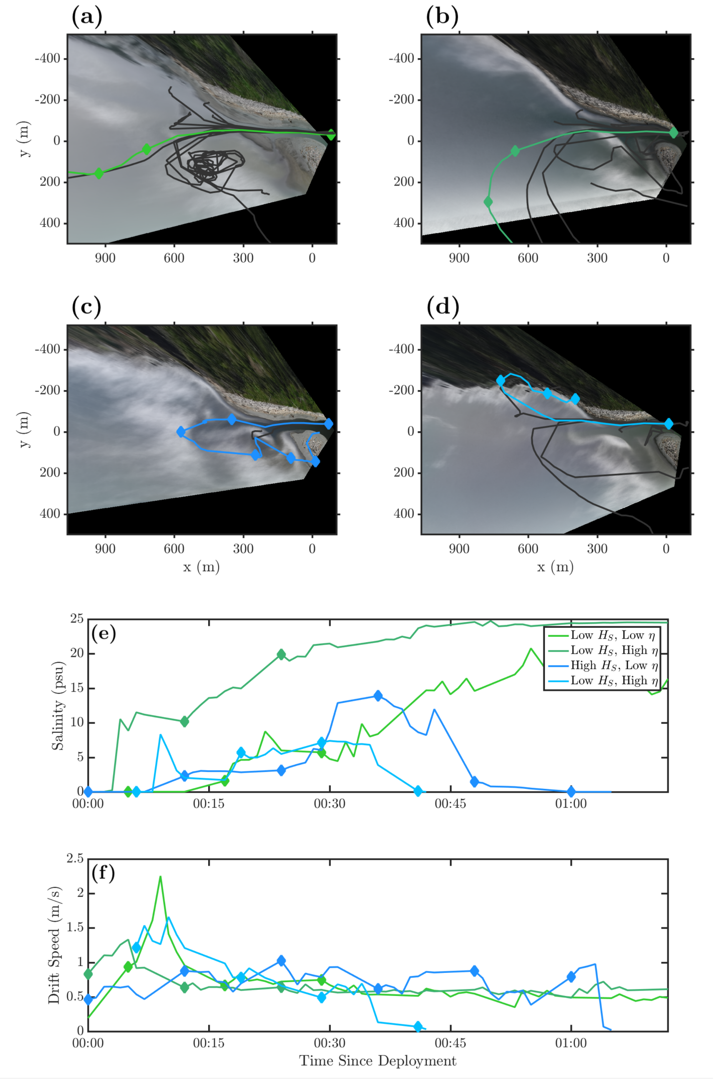

Figure 2.3: Example UAS images, drifter tracks, and drifter data time series for varying wave and tidal conditions. Images have been rectified and averaged over ten minutes. (a) shows low water and low wave forcing, (b) shows high water and low wave forcing, (c) shows low water and high wave forcing, (d) shows high water and high wave forcing. Panels (e) and (f) show time series plots of near-surface salinity and drift speed, respectively, for the same colored drift tracks in panels (a)-(d). Filled diamonds occur indicate the corresponding point in space on (a)-(d) to a point in time in (e)-(f).

gauge time series, adjusted by this factor, in our calculations. In order to fill in the gaps in both time series, we use the *UTide* Matlab functions [Codiga, 2011]. In this time series reconstruction, we consider the M2, S2, and K1 tidal constituents while allowing a trend over time to account for the decrease in discharge during the study period. We perform this time series reconstruction on both the river mouth ADCP and dock tide gauge in order to be consistent in our calculations. This time series reconstruction does not allow for the constant river velocity and depth observed during maximum flow at low water. These effects will partially cancel, as the velocities have maxima higher than the observed constant while the depths have minima lower than the observed constant. This will likely cause overestimates of peak river momentum flux.

Wave radiation stress

We calculate the cross-shore component of the shoreward wave radiation stress as

$$S_{xx} = g \int_{f0}^{\infty} E(f) \left(\frac{c_g(f)}{c_p(f)} (\cos^2 \theta(f) + 1) - \frac{1}{2} \right) df, \tag{2.2}$$

where $E(f)$ is the spectral wave energy in m^2/Hz, $c_g(f)$ is the wave group velocity associated with a frequency at the water depth where the measurement is made, $c_p(f)$ is the wave phase speed associated with a frequency at the water depth where the measurement is made, and $\theta(f)$ is the wave direction from shore normal associated with a frequency. This formulation assumes the waves are shore-normal, which is approximate, but not exact, at the AWAC (where this calculation is made). We ignore the role of wave direction in the calculation of S_{xx}, thus the calculation represents the maximum crosshore radiation stress for a given wave energy flux and depth.

2.2.3 Length & velocity scale calculations

Surf zone width

We use the AWAC measurements of local wave conditions, the UAS images, and the SWIFT v4 water depth measurement to estimate surf zone width. The SWIFT v4 water depth measurement is used to generate a depth profile for the beach south of the Quinault River mouth. This calculation uses detided SWIFT depth measurements averaged on a 30 m cross-shore grid. We use the same gridding to obtain channel bathymetry. The average depths are then smoothed using a low pass Butterworth filter. To resolve near-shore bathymetry, we extract the waterline from 25 georectified time averaged UAS images at varying tidal stages. By combining the waterline extractions with the SWIFT South beach bathymetry and smoothing again, we obtain a cross-shore bathymetry profile.

We calculate surf zone widths using this bathymetry profile, the AWAC measurements, the wave shoaling equations, and assuming a critical $\gamma = H_S/d$, where H_S is significant wave height and d is water depth. We calculate the increase in wave height to the point of breaking using a shoaling constant K_S, such that $H = K_S H_o$ and $K_S = \sqrt{\frac{c_{go}}{c_{gb}}}$, where H is a shoaled wave height, H_o is the wave height at the AWAC, c_{go} is the group velocity at the AWAC and c_{gb} is the group velocity at the onset of wave breaking. We assume that waves break in shallow water, and so $c_{gb} = \sqrt{gd_b}$. By assuming $\gamma_b = 0.6$, we can thus calculate the depth at breaking such that $d_b = \left(\frac{H_o}{\gamma_b}\frac{c_{go}^{1/2}}{g^{1/4}}\right)^{4/5}$. We choose $\gamma_b = 0.6$ to match the conditions when no breaking is seen in the channel in the UAS imagery (Figure 2.3a-d). We then look up the corresponding cross-shore distance of d_b at the tidal stage associated with that time, and calculate a surf zone width L_{SZ} by measuring the distance to the breakpoint from the origin of our coordinate system, the maximum onshore position of the river mouth. This length scale includes the tidal modulation of the waterline in the nominal surf zone width for ease of comparison. Examples of the surf zone width calculation can be seen in Figure 2.4 for both the channel and the South beach bathymetry.

This methodology does not take into account wave-current interaction in and near the offshore channel. Such interactions cause refraction, steepening, and breaking in surface waves, and could be expected to influence the surf zone width [Kirby and Chen, 1989; Zippel and Thomson, 2015, 2017]. We neglect such interactions in our calculation of surf zone width due to their spatially complex nature. Discussion of the potential effects of wave-current interaction can be found in section 2.4.4. In general, we expect depth-limited breaking to be

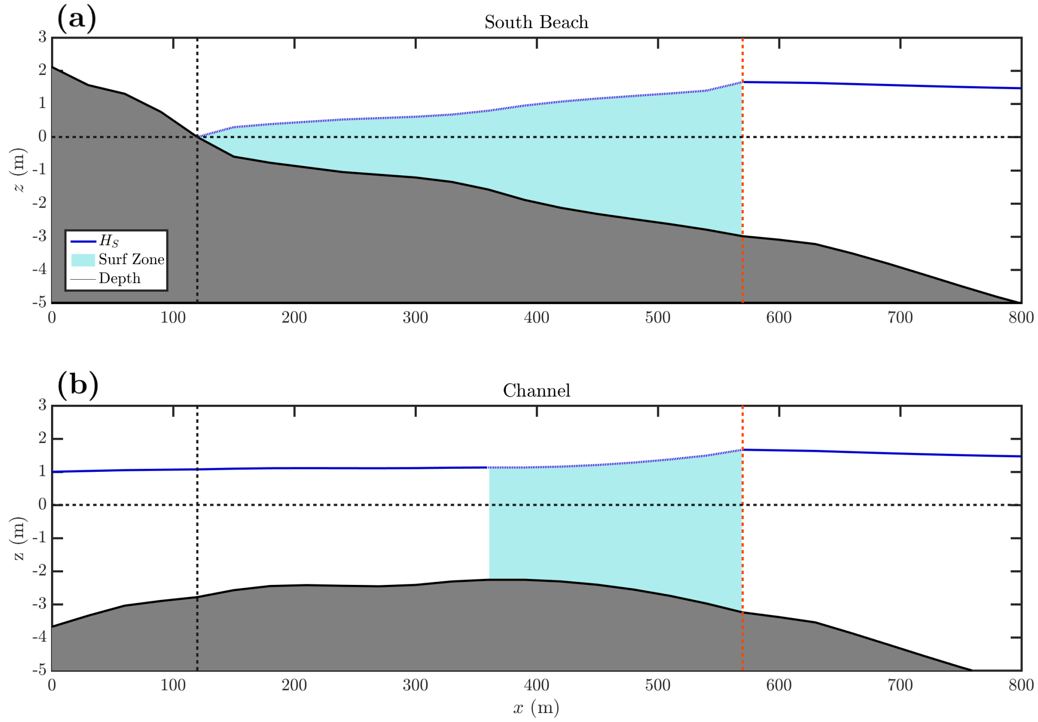

Figure 2.4: Wave shoaling over cross-shore bathymetric profiles on the (a) South beach and (b) channel at $\eta = 1.05$ m. The shaded grey region indicates the bathymetric profile. The solid blue line indicates a cross-shore position where a wave of height H_S would not be expected to break via depth limitation, while the dotted blue line and corresponding shaded area indicate a region of expected wave breaking. The horizontal dashed black line indicates the still water level at $\eta = 1.05$ m, and the vertical dashed black line indicates the cross-shore location at which $d = 0$ m on the South beach. The red dashed line indicates the predicted break point.

a much more important process in this system.

Near field plume length

We calculate L_{NF}, the offshore extent of the plume nearfield, based on equation 2.1. Here $M = M_0 = u_0 Q_0$, $B = B_0 = g' Q_0$, and $\delta = w_e / u_0$. We take u_0 to be the tidally varying river mouth velocity from the UTide reconstructed ADCP surface velocity (2.2.2) and $Q_0 = u_0 b_0 h_0$ to be the river discharge. The effective channel width b_0, is determined according to $b_0 = \frac{\int Q dt}{\int u_0 h_0 dt}$, where Q is the modified USGS Quinault Lake gage discharge. The reduced gravity for the system, g', is calculated using the average ambient water density at the nearshore moorings such that $\Delta\rho = 24$ kg/m^3. The entrainment velocity w_e is calculated from the inflow bulk Richardson number using the methodology from Yuan and Horner-Devine [2013] such that $\delta = 0.03 Ri_{b0}^{-1/2}$. To calculate $Ri_{b0} = \frac{g' h_0}{u_0^2}$, we use the river mouth velocity and depth, along with the reduced gravity for the system. The median result from this calculation yields $w_e = 8$ mm/s. This is similar to results from the Fraser liftoff zone, where $1 < w_e < 7$ mm/s [MacDonald and Geyer, 2004]. In order to minimize noise, we use the tidally phase averaged quantity $\overline{L_{NF}}$ to define the modes of the conceptual model. The surf zone width is not similarly averaged so as not to eliminate the surf zone width's dependence on wave conditions during a given bin of tidal phase. Using the surf zone width concurrent with each drifter deployment on both axes introduces auto-correlation, but allows a more complete dynamical understanding of the conceptual modes.

As discussed in section 2.1.4, L_{NF} is used in this analysis as a representation of the scale of the near field plume at one point in time, even though it is based on variables that vary significantly over the course of a tidal cycle. This characterization is only meaningful if the timescale over which L_{NF} adjusts is short relative to the tidal period. We estimate the near field adjustment timescale as $T_{NF} = L_{NF}/u_0$, which is approximately 10 minutes for the Quinault. This is much less than one quarter of a tidal cycle, indicating that L_{NF} is able to adjust to tidal changes in the forcing variables. In larger plume systems, T_{NF} is expected to be longer and more caution must be taken in applying this scaling. For example, at the

Columbia River, $u = 2.5$ m/s, $Q = 7000$ m^3/s, and $w_e = 2$ mm/s [McCabe et al., 2008], resulting in $L_{NF} \sim 8.5$ km and $T_{NF} = 1$ hr.

2.3 Results

2.3.1 Tidal variability of river and wave forcing

Drifter behavior, as defined in section 2.2.1, shows a clear dependence on tidal phase (Figure 2.5a); all drifter escapes and near escapes occur at high or low water. This result suggests that tidally varying depth and discharge velocity strongly influence the fate of river water in the surf zone. The maximum velocity at the river mouth occurs just before low water and minimum velocity occurs just after high water. Drifter behavior is thus related to tidal variations in the momentum flux, u^2h, in the Quinault system (Figure 2.5c-d); escapes occur only near maxima of tidal stage or river velocity. The incident wave radiation stress does not vary tidally. Thus, low water drifter escapes are coincident with a tidal maximum in river momentum flux relative to a tidally constant wave momentum flux. Escapes also occur at high water, when river momentum is at its lowest. Observations from drifters that escape the surf zone indicate an increase in near-surface salinity as the drifters transit onto the inner shelf. This increase occurs more quickly for high water escapes than low water escapes 2.3e). Trapped drifters tend to measure freshwater while remaining in the surf zone (Figure 2.3e). These behaviors will be further examined in section 2.3.3.

Time series of salinity measurements show episodic occurrences of freshwater at the nearshore moorings (Figure 2.6b) that can be compared with the variability of river momentum flux and wave radiation stress (Figure 2.6d) over the 5 days when all the moorings were concurrently deployed. The lowest salinities during freshwater events were observed furthest from the river mouth in alongshore position at the south mooring. These salinities reach as low as 13.7 psu during the strongest event at the south mooring, and between 20 and 25 psu during other events. These salinities differ from ambient water by 15 psu during the strongest event, and by 3-5 psu during other events (Figure 2.6b). The freshwater events

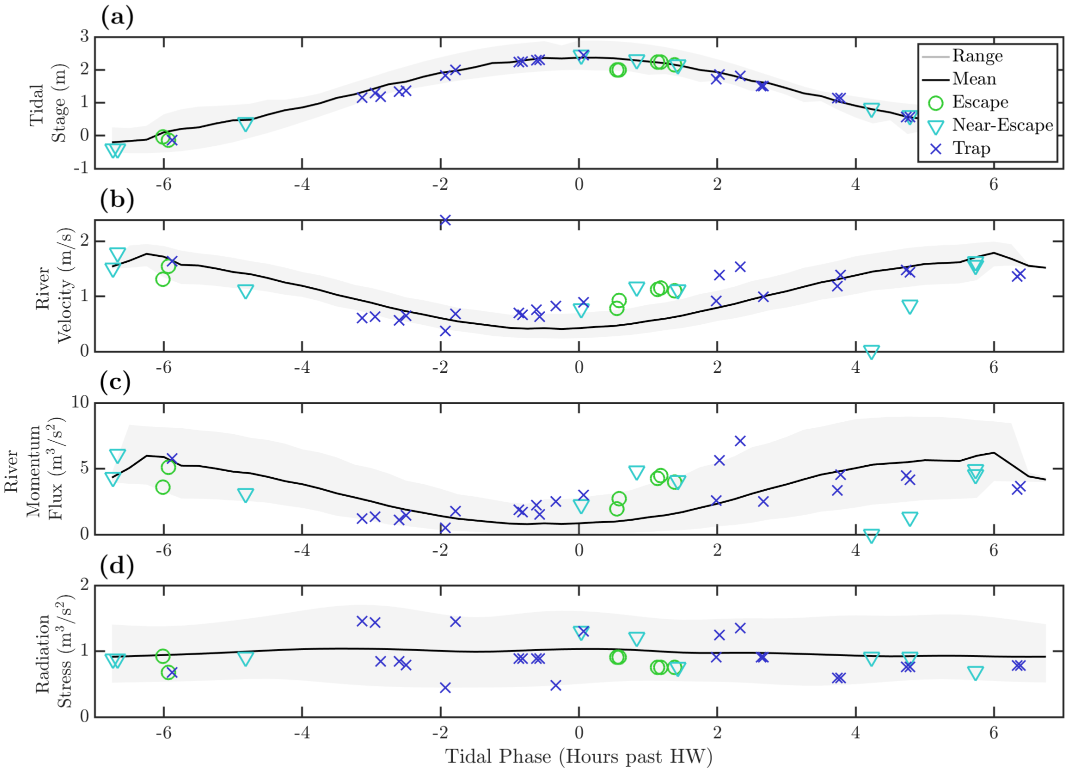

Figure 2.5: Tidally phase-averaged measured quantities and calculations using moorings or gauge data (solid black lines), and drifter data (markers). Markers indicate drifter behavior: green circles are escapes, teal triangles are near-escapes, and blue crosses are traps. The grey shaded area indicates the range of values for a measurement or calculation at a given tidal phase. (a) shows tidal stage from the Point Grenville gauge, (b) shows river velocity from the inlet mooring or measured by a drifter deployment, (c) river momentum flux from the inlet mooring or a drifter deployment, (d) radiation stress from the AWAC.

occur when river momentum is near its maximum at low water, and thus when the ratio $\frac{u^2h}{S_{xx}}$ is near a local peak. This correlation is not necessarily indicative of river water reaching the shelf due to its own momentum, however; the salinity minima are usually observed closest to shore at the south mooring, which is sometimes inside the surf zone. Therefore, observations of freshwater at nearshore moorings are concurrent with maximum river momentum at low water, but are not necessarily indicative of freshwater escaping the surf zone, as the surf zone width is also at maximum at low water and could be larger than the near field plume length. This observation suggests that the surf zone width is an important scale in this system and motivates the conceptual model proposed in section 2.1.4.

2.3.2 Length scale comparison & drifter fate

The length scales L_{NF} and L_{SZ} also vary tidally. The near field length and the river momentum flux have similar dependencies, and so it follows that L_{NF} is also at maximum at low water and minimum at high water (Figure 2.6c). The surf zone width as defined in section 2.2.3 varies tidally as the shoreline moves toward or away from a fixed reference point, and as such is at maximum at low water and a minimum at high water. Therefore, L_{NF} and L_{SZ} vary in phase with each other over the course of a tidal cycle. The tidal variability of the near field length is larger than that of the surf zone width, and so the quantity L_{NF}/L_{SZ} is maximum at low water and minimum at high water.

In Figure 2.8, every SWIFT v3 and v4 drift concurrent with the AWAC deployment is plotted in terms of its cross shore excursion normalized by surf zone width, x_{max}/L_{SZ}, and the ratio $\overline{L_{NF}}/L_{SZ}$. Drifters may be quantitatively defined as having escaped the surf zone when $x_{max}/L_{SZ} > 1$ and as trapped in the surf zone when $x_{max}/L_{SZ} < 1$. Most drifters are observed to be trapped in the surf zone, but escapes do occur when $\overline{L_{NF}}/L_{SZ}$ is low or high, coincident with high or low water, respectively. The surf zone width is low for high water escapes, potentially indicating bathymetric dominance, while the near field length is large for low water escapes, potentially indicating river dominance.

Trapping events occur when wave forcing dominates over river forcing and channel bathymetry does not play a significant role in determining the breakpoint. During times when the moorings are not in the surf zone the salinity is generally high and stratification is generally low, corroborating this observation (Figure 2.6b). Closer to shore, drifter observations indicate the presence of trapped freshwater. The wave dominated behavior may thus be associated with a cross-shore density gradient through the surf zone. Trapped drifters are typically associated with $\gamma > 0.6$ at the edge of the channel, indicating that waves have broken or are breaking in the channel during these drifter deployments. The maximum drifter excursions during wave dominated conditions are smaller than the surf zone width (Figure 2.8a).

Escapes can occur when river forcing dominates over wave forcing at low water or bypasses wave forcing when there is minimal wave breaking in the channel. Drifters that escaped the surf zone were subject to the forcing present on the inner shelf; all but two such drifters beached within hours or days of deployment after travelling along the coast. When river forcing is large at low water, high stratification (low surface salinity) is sometimes observed at the moorings, while high water escapes are generally associated with low offshore stratification (Figure 2.6b). These observations are corroborated by drifter measurements of salinity, which show a faster increase in salinity for a drifter escape at high water than a drifter escape at low water (Figure 2.3e). When drifters escape the river mouth at high water, waves are not breaking at the offshore edge of the channel ($\gamma < 0.6$). Low water drifter escapes often occur near the daily maximum in L_{NF} and river momentum flux u^2h.

The behaviors described above can be classified into wave, river, or bathymetric dominant modes by the conceptual model.

2.3.3 Conceptual model

Wave dominant conditions

The most common behavior observed in our study is that wave breaking traps river water in the surf zone. Based on the definition of the near field, the plume has lost most of its initial momentum once it reaches L_{NF}. If it is still in the surf zone at that point, the wave forcing

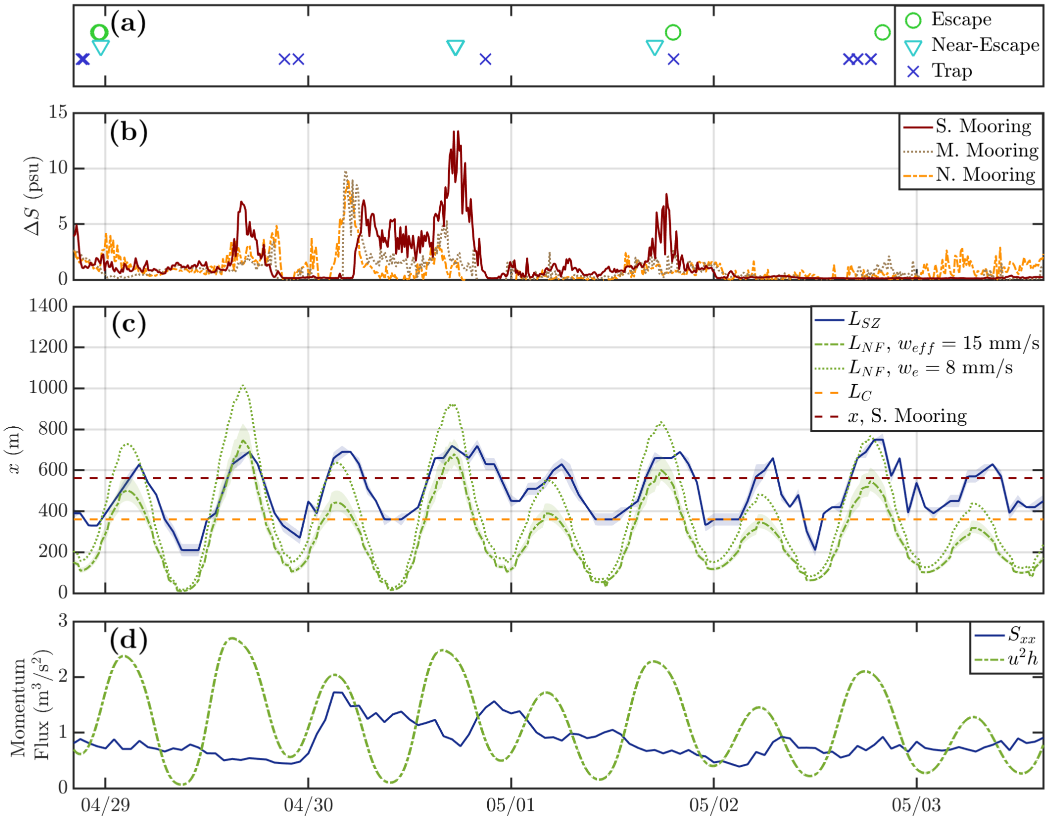

Figure 2.6: Time series of (a) drifter behavior, with the same symbols as in Figure 2.5; (b) Salinity difference from 3 m to 1 m at the south (red solid line), middle (brown dashed line); and north nearshore moorings (orange dashed-dotted line); (c) Surf zone width (blue), near field length (green), and channel length (orange). The near field length is calculated with $w_e = 8$ mm/s (green dashed line) and a range of $12 < w_{eff} < 18$ mm/s (purple shaded region) with $w_{eff} = 15 mm/s$ as the dashed-dotted green line. The dashed burgundy line indicates the cross-shore position of the south mooring; (d) Wave radiation stress, S_{xx} at the AWAC and river momentum flux, u^2h at the inlet mooring.

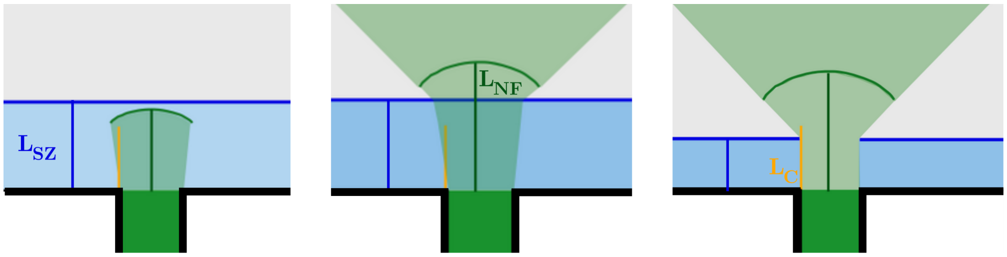

(a) Wave dominance **(b) River dominance** **(c) Bathymetric dominance**

Figure 2.7: Schematics of each mode of the conceptual model, with the surf zone width indicated by the blue line, the near field length by the green line, and the channel length by the orange line. Panel (a) shows wave dominance, (b) shows river dominance, and (c) shows bathymetric dominance. The dominant length scale for each mode is labeled.

appears to block further seaward movement (Figure 2.7a).

Wave dominant conditions can be defined for the length scales presented in Figure 2.8 as when $\overline{L_{NF}} > mL_{SZ}$ and $nL_{SZ} < L_C$. Here, m and n are constants close to unity and $L_C \approx 360$ m (section 2.3.3). In our observations, $m = 0.8$ and $n = 0.83$. Thus, once a drifter approaches the edge of the surf zone, there exists the possibility of an escape while $\overline{L_{NF}} > 0.8L_{SZ}$. Likewise, when the surf zone width narrows such that $0.83L_{SZ} < L_C$, there exists the possibility of a bathymetric dominated escape. The value $m = 0.8$ is chosen such that drifts where $x_{max}/L_{SZ} > 1$ when L_{NF}/L_{SZ} is high (low water) are classified as river dominated escapes. Similar logic leads us to define $n = 1.2$, such that drifts where $x_{max}/L_{SZ} > 1$ and L_{NF}/L_{SZ} is low (high water) are classified as bathymetric dominated escapes. This classification results in 100% of drifts during wave dominant conditions being trapped in the surf zone. The difference of m and n from unity is partially due to unresolved short time scale variability in forcing, such as the timing of a drifter release relative to the timing of the maximum wave height in a wave group. Specifically for n, measurement error in SWIFT bathymetry estimates could play a role in n being less than unity. Additionally, it is likely that m & n do not define exact thresholds between the conceptual modes, i.e.

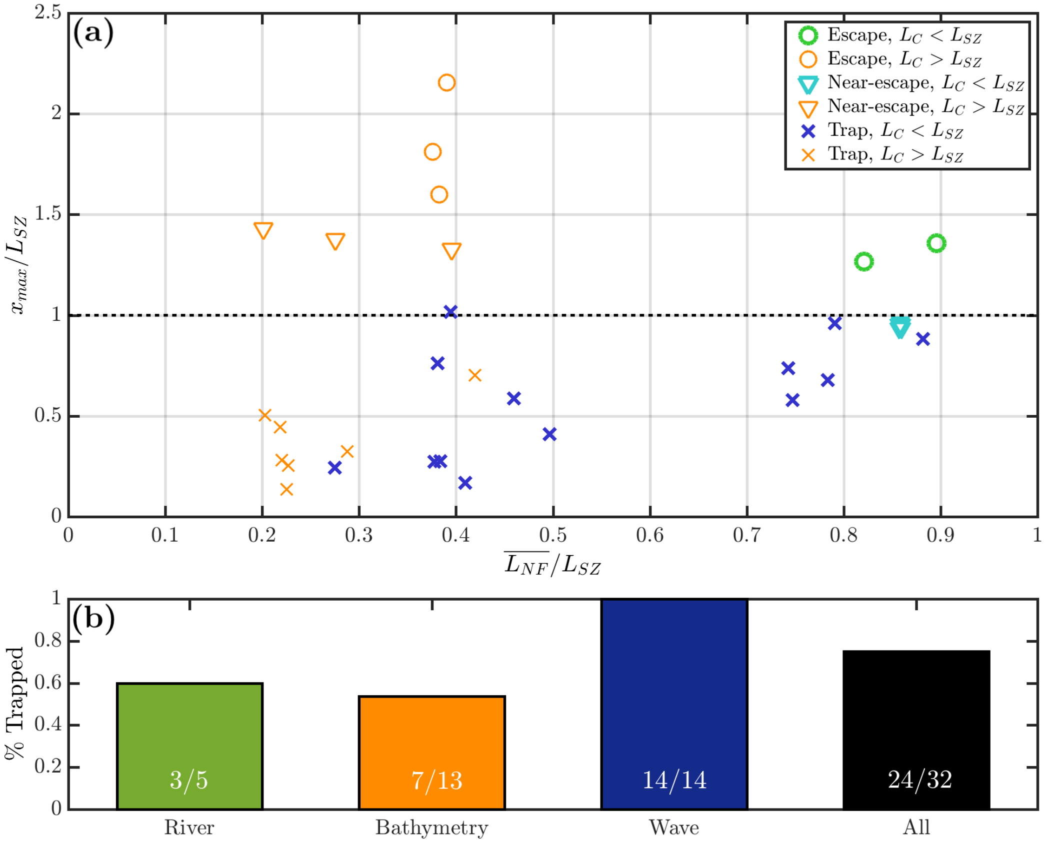

Figure 2.8: Panel (a) shows drifter excursion normalized by surf zone width plotted against the tidally phase averaged near field length normalized by surf zone width. Marker symbol indicates drifter behavior as in Figure 2.5, and orange marker color indicates drifts during bathymetric dominated conditions. Panel (b) shows the percent of drifters trapped during each mode of behavior and all drifts. The 32 drifts shown here were v3 or v4 SWIFTs deployed concurrently with the AWAC.

the value of m could represent a value of $\overline{L_{NF}}/L_{SZ}$ where river dominated escapes occur more frequently. Similar logic could be applied to the value of n for the bathymetric and wave dominant modes. More drifts would be needed to fully develop a more probabilistic approach to the conceptual model.

The observed trapping of river water in the surf zone is consistent with the modelling results of Rodriguez et al. [2018], who find that the percentage of freshwater within the surf zone scales with increased wave forcing. An important distinction of this result, however, is the dependence of L_{NF} on w_e, indicating that mixing, as well as momentum, can be important in determining wave effects. This is discussed in more detail in section 2.4.1.

River dominant conditions

Calculations of $\overline{L_{NF}}$ and L_{SZ} show that $\overline{L_{NF}} > mL_{SZ}$ at low water, such that river dominant conditions can occur when the river momentum is at its daily maximum (Figure 2.7b). There are two cases where drifters escape the surf zone when $\overline{L_{NF}}$ and river momentum flux are at their maximum at low water, such that $\overline{L_{NF}} > mL_{SZ}$ and $u^2h > S_{xx}$ (Figure 2.8). Therefore, 60% of deployed drifters are trapped in the surf zone when river dominant conditions occur (Figure 2.8b). As some, but not all, drifters escape the surf zone during river dominant conditions, $\overline{L_{NF}} > mL_{SZ}$ is a necessary but not sufficient condition for river water escape.

Rodriguez et al. [2018] conclude that higher river momentum can result in a larger percentage of freshwater transport onto the inner shelf. Their numerical model simulations do not include tides, but we suggest here that the conditions in their higher river momentum and wave forcing simulations are analogous to those leading to maximum values of L_{NF} and L_{SZ} that we observe at low water at the Quinault. The most similar simulation to Quinault conditions uses a discharge $Q = 100$ m^3/s and a wave height $H_S = 1$ m, which results in 10% of river water being trapped in the surf zone. During the two instances of river water escapes at low water we observed with drifter deployments, $Q \approx 140$ m^3/s and $H_S \approx 1.4$ m.

Bathymetric (channel) dominant conditions

For low wave conditions at high water, $nL_{SZ} < L_C$, indicating that wave breaking is initiated onshore of the end of the offshore channel (thus, there is minimal breaking in the channel). In order for wave forcing to trap river water in the surf zone, wave-driven momentum must dominate over river momentum. Wave-driven momentum in the surf zone is caused by the spatial gradient in the cross-shore component of the shoreward radiation stress, and this gradient is directly related to wave breaking. When (and where) wave breaking does not occur, there is minimal opposition to the river momentum and river water can escape from the surf zone (Figure 2.7c). This can occur in the the natural offshore channel, which is analogous to the dredged channels often constructed in engineered river mouths. For the Quinault, the channel diverges from the beach bathymetry profile at a cross-shore distance $L_C \approx 360$ m, and is on average 1 m deeper than the beach bathymetry before dropping to a maximum depth of 4.5 m inside the river inlet. Thus, breaking will only occur in the channel for $nL_{SZ} > L_C$, when $\gamma > 0.6$ inside the channel. Bathymetric dominance is indicated on Figure 2.8a by orange symbols. Immediately after high water, all drifts reach $x_{max}/L_{SZ} > 1$ until $nL_{SZ} > L_C$, around 2 hours after high water (not shown). Interestingly, while $nL_{SZ} < L_C$ before high water, drifts result in traps at values close to L_{NF}, despite $\gamma < 0.6$ at the channel edge during most such drifts.

When bathymetric dominant conditions occur, 55% of drifters are trapped in the surf zone (Figure 2.8b). As with river dominant conditions, this implies that bathymetric dominance is necessary but not sufficient for the escape of river water. Our results suggest a minimum river momentum that is required for these escapes to occur, specifically the value observed just as the river momentum increases following high water. This minimum river momentum is equal to the minimum wave momentum in the channel, which occurs when $\gamma < 0.6$. The wave momentum is nonzero due to the breaking of some waves that are larger than H_S (i.e., the breaking criterion is statistical, and the 1/3 of waves larger than H_S may break even when γ is subcritical). Before high water, the river momentum falls below this threshold, but as the river momentum increases after high water, escapes can occur.

Breaking occurs on either side of the channel when $nL_{SZ} < L_C >$ and may increase outflow currents and thus the probability of escape during bathymetric dominant conditions. The alongshore gradients of radiation stress introduced when breaking occurs near the edges of the channel are similar to bathymetrically driven rip currents. Olabarrieta et al. [2014] show that such a spatial pattern of breaking around a tidal channel introduces a rip-like circulation in the channel, increasing the outflow velocity.

Bathymetric dominance is a significant mechanism for transporting fresh river water onto the inner shelf in the Quinault River system, but may not be important in systems with small or zero tides [Rodriguez et al., 2018] because variation in the offshore extent of the surf zone is lower. Other systems with a deep channel offshore of the river mouth and a steep beach at high water may also export river water to the shelf in this manner.

Rodriguez et al. [2018] find that the percentage of freshwater trapped in the surf zone scales with the ratio of river momentum flux. This gives similar results to the scaling of L_{NF} versus L_{SZ} presented in the present work. The tidal variability we examine in this paper is similar to the variable parameter space explored in the numerical studies of Rodriguez et al. [2018], with three notable distinctions. First, the minima and maxima of L_{NF} and L_{SZ} are co-located within the tidal cycle at high water and low water, leading to coupled dynamics. Second, the local bathymetry plays a significant role in the transport of river water onto the shelf; when the breakpoint moves onshore of the channel edge, minimal wave breaking induced momentum is present to counteract the river momentum. Third, the tidal modulation of L_{NF} sets the initial excursion of river water into the surf zone in wave dominated conditions (section 2.4.1), and it is possible that L_{NF} is modified by breaking wave induced mixing or momentum.

2.4 Discussion

2.4.1 Scaling drifter excursion

We find that the near-field plume length is an important factor in determining the extent to which river water penetrates the surf zone. The maximum drifter excursion for trapped drifters ($x_{max} < L_{SZ}$) varies tidally (Figure 2.8). In Figure 2.9, x_{max} is plotted versus the tidally phase averaged near field plume length L_{NF} for all trapped drifters. We observe a linear trend in this relationship with an R^2 value of 0.9. This result suggests that, during trapping conditions, the distance freshwater penetrates into the surf zone is set by L_{NF}. Thus, the tidal variability in the observed excursion distance is largely explained by the variability in L_{NF} associated with the tidal fluctuations in velocity and depth at the river mouth.

There are several possible sources of variability in the relationship between x_{max} and L_{NF}. We expect, however, that entrainment resulting from wave breaking turbulence in the surf zone will be a dominant source of variability; it will significantly increase w_e above the value predicted for shear mixing in the absence of waves and decrease L_{NF}. In this section we investigate the relationship between x_{max} and L_{NF}, defining an effective entrainment velocity, w_{eff}, which accounts for the enhanced turbulence associated with wave-breaking.

The value of $w_{eff} = 15$ mm/s is based on the fit in Figure 2.9, assuming that all the variability can be accounted for by entrainment. This is clearly a simplification of a very complex system, but provides useful estimates for understanding the possible mixing enhancement in the surf zone. The predicted value of $w_e = 8$ mm/s based on Yuan and Horner-Devine [2013] and Christodoulou [1986] underpredicts the drifter excursion (Figure 2.9). Since $w_{eff} > w_e$, we conclude that a higher effective entrainment better characterizes the relationship between L_{NF} and x_{max}. Calculations of L_{NF} made using $w_e = 8$ mm/s yield larger values, which in turn increase the value of m such that $m \approx 1.2$ for a lower entrainment velocity. This increase of m above unity is physically unintuitive and statistically unlikely. We expect that river water will escape the surf zone when $L_{NF} > L_{SZ}$ ($m = 1$) because once river water

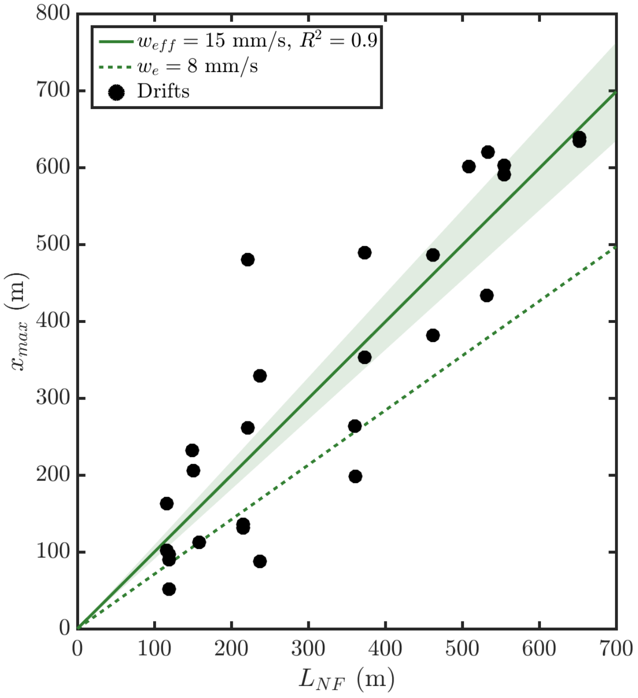

Figure 2.9: The relationship between near field length and drifter excursion. Two fits are shown, one calculated with $w_e = 8$ mm/s (dashed green line) and one calculated with $w_{eff} = 15$ mm/s (solid green line). The shaded area indicates the 95% confidence interval of the slope for the case where $w_{eff} = 15$ mm/s.

is outside of the surf zone its propagation is no longer opposed by the landward force from breaking waves. This indicates that $w_e = 8$ mm/s is too low to properly represent the observed dynamics. The effective increase of entrainment in the presence of breaking waves could indicate that the high levels of turbulence in the surf zone lead to more plume mixing.

The relationship evident in Figure 2.9 suggests that drifters stop when they reach L_{NF}, which corresponds to the point where the initial river momentum falls below the buoyant gravity current speed. Thus, this result implies that the buoyant gravity current speed is less than the opposing cross-shore wave velocities in the surf zone. The latter can be estimated based on the Stokes' drift [Stokes, 1847]. Based on estimates from our mooring measurements, the average Stokes' drift and gravity current velocities are 0.13 m/s and 0.08 m/s, respectively. Thus the Stokes' drift is generally larger than the gravity current speed. The plume may therefore be stopped from propagating offshore as a buoyant gravity current in the surf zone.

The mixing and entrainment rate due to wave breaking in the surf zone is an active area of research, with no canonical estimate available to compare to plume entrainment rates. However, the turbulent kinetic energy dissipation rate that would be associated with wave-driven mixing in the surf zone is generally higher than the dissipation rate associated with shear-driven mixing in a river plume. Near-surface dissipation rates in the surf zone can reach order $\varepsilon = 10^{-2}$ W/kg [Feddersen and Trowbridge, 2005a], while plume dissipation rates have been found to be of order $\varepsilon = 10^{-4}$ W/kg in medium sized rivers like the Quinault, such as the Merrimack River in Massachusetts [MacDonald et al., 2013]. There are other factors that could contribute to the drifter excursion differing from the near field length. For example, wave momentum influences the system dynamics [Rodriguez et al., 2018] and is not included in the near field length scale. Wave momentum influence would result in a decrease in w_{eff} to compensate for a decrease in total offshore momentum. As w_{eff} is larger than w_e, wave mixing is likely the relevant controlling process in the Quinault system. In larger systems it has been suggested that the ratio H_S/h_p determines the extent to which wave-driven turbulence can affect plume mixing [Kastner et al., 2018]. SWIFT drifters with

3 CT sensors that escape the surf zone measure strong stratification in the upper 1.2 m, indicating that H_S/h_p could be in a range where wave-driven turbulence could affect plume mixing.

The drifter excursion for trapped drifters is a reference point for where those drifters stop following the near-surface velocity and begin to be influenced by breaking waves. Thus, the over-prediction of x_{max} by L_{NF} for $w_e = 8$ mm/s could also be due to the drifters no longer behaving in a Lagrangian manner onshore of L_{NF}. This would suggest that the drifters are no longer Lagrangian once they reach a fraction of L_{NF} determined for $w_e = 8$ mm/s. From the best fit line for $w_e = 8$ mm/s from Figure 2.9, this excursion would be $x_{max} \approx 0.7L_{NF}$. If non-Lagrangian bias was the most significant driver of x_{max}, we would expect the drifter hull type to play a role in drifter fate. This is not the case, however, as the different hull shapes of drifters used in the study do not have an effect on drifter statistics: about one third of each type of SWIFT escape or nearly escape the surf zone (Table 2.2). It is impossible to completely rule out non-Lagrangian bias in x_{max}, but it seems likely that wave-driven mixing and entrainment plays a significant role. Thus, when $L_{NF} < L_{SZ}$ and $L_{SZ} > L_C$, the near field plume length scale sets the distance river water can penetrate through the surf zone.

2.4.2 Seasonal variability of the fate of freshwater

In this section we apply the conceptual model developed above to a time series of wave, discharge, and tidal amplitude data from the entire year 2017 in order to assess longer time scale processes. These time series are acquired from the CDIP 036 Grays Harbor buoy, the USGS Quinault Lake stream gauge, and the NOAA Pt. Grenville tide gauge. All quantities necessary for the calculation of L_{NF}, L_{SZ}, and L_C can be calculated or used directly from this data, except for u and h at the river mouth. We estimate the water depth at the river mouth as $h = f_h(\eta, Q)$, where η is the offshore tidal amplitude, and f_h is a multiple linear regression. The river mouth velocity can then be estimated as $u = f_u(h, \partial h/\partial t, Q)$, where f_u is a multiple linear regression. We define the functions f_h and f_u using data collected during our measurement periods. Lower and upper limits are set on the variability of u by enforcing continuity, such that if the estimated volumetric flux out of the river mouth is greater than twice the gage discharge or less than one quarter the gage discharge, the velocity is instead set by the discharge, assuming a channel width of $b = 60$ m. These thresholds are determined by the tidal variability of the river mouth volumetric flow rate observed during the study period. The surf zone width is calculated using the methods from section 2.2.3, assuming that wave conditions along the coast do not vary significantly between Gray's Harbor and the Quinault River mouth, and that the bathymetry measurement shown in Figure 2.4 are representative of the entire year. In general, the length scales calculated from our measurement period and extrapolations from the gage and buoy time series for the same period agree well, with $R^2 = 0.93$ and $R^2 = 0.7$ for L_{NF} and L_{SZ} respectively. The lower correlation in surf zone width is likely caused by spatial heterogeneity in the wave field.

The results of this year-long extrapolation are shown in Figure 2.10. The length scales vary on seasonal and shorter time scales, driving changes in the fate of the river discharge. In general, L_{NF} varies with Q, L_{SZ} varies with H_S (not shown), and both vary with the tide (Figure 2.10b). The minimum and maximum values of L_{NF} and L_{SZ} shown by the shaded region in Figure 2.10b are likely to occur for both length scales at high and low water, respectively, and are thus comparable. For simplicity, we assume that river water discharged during bathymetric and river dominated conditions initially escapes the surf zone, and river water discharged during wave dominated conditions is initially trapped in the surf zone. Fourteen day averaged values of the frequency of each mode and the percent of discharge during each are shown in Figure 2.10c. We can thus use the frequency of occurrence for each mode and the measured discharge to calculate the percent of river water that initially escapes the surf zone or is initially trapped in the surf over the course of one year (Figure 2.10c-d). We find that ∼70% of the discharge is trapped in the surf zone, with ∼20% escaping due to river dominance and the remaining ∼10% escaping due to bathymetric dominance.

Our results suggest that wave dominant conditions are prevalent during most of the year, except during summer and late fall (Figure 2.10c). As a result, most of the river water is trapped in the surf zone immediately after it is discharged from the mouth. During the

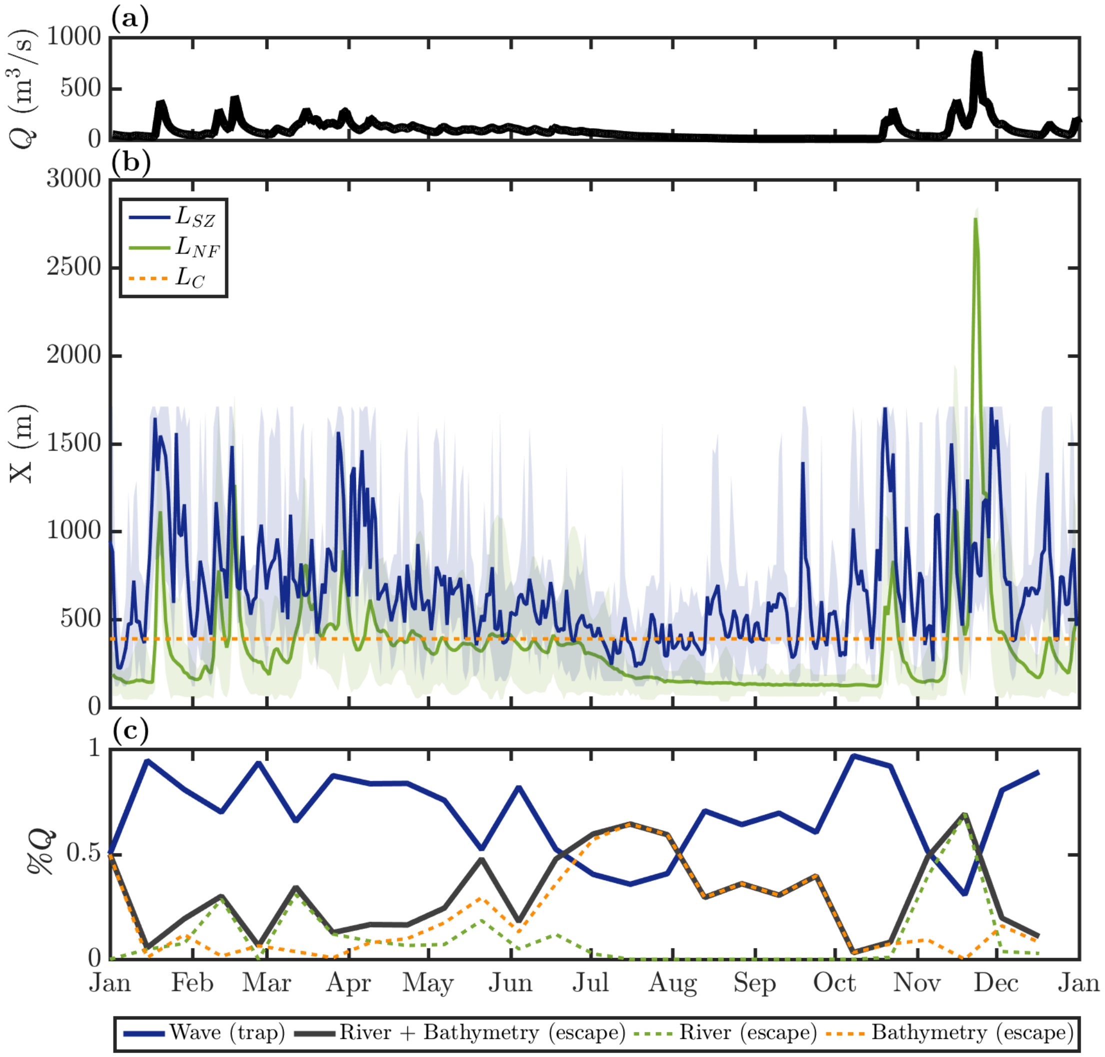

Figure 2.10: The conceptual model, applied to wave, discharge, and tidal amplitude data for the year 2017. Panel (a) shows a time series of discharge; panel (b) sbows a time series of the conceptual model length scales averaged over one day, with the maximum and minimum of L_{SZ} and L_{NF} given by the shaded region; panel (c) shows the percent of river discharge over 14 days governed by each conceptual mode, with the bathymetric and river dominated conditions summed to give a total percent of time when escapes might be expected.

summer, the model predicts that more than 50% of river water is exported through the surf zone to the inner shelf because Wave forcing is low and the bathymetric condition is the dominant mode. Local residents report that the Quinault estuary can be quite salty during these low flow periods in the summer, so the freshwater flux associated with bathymetric escapes in the summer may be low. In late fall, discharge reaches its largest peak of the year during a stormy period and the model predicts more than 50% export of freshwater due to river dominated conditions. The smaller storm-driven peaks in discharge between January and April also result in export driven by river dominance. River dominant export during late fall, winter and early spring accounts for most of the escaped river water over the course of the year. Not all storms force river water escapes—storms also result in large waves and surf zone widths that can trap river water.

The strong dependence of the conceptual model on tidal variability indicates that the neap-spring cycle should be an important driver of the fate of freshwater, with more energetic spring tides leading to more bathymetric and river dominated escapes than neap tides. The neap-spring signal is only visible in L_{NF} during the summer, when no river dominant conditions are observed. For the rest of the year neap-spring effects are obscured by variability in river discharge and wave height.

2.4.3 Comparison to other river systems

The conceptual model developed above can be applied to other rivers by plotting L_C/L_{SZ} against L_{NF}/L_{SZ}, using characteristic values of the length scales for other systems (figure 2.11). High values of L_{NF}/L_{SZ} indicate river dominance, while low values indicate wave dominance. High values of L_C/L_{SZ} indicate bathymetric dominance, while low values indicate wave dominance. Low values of both ratios are required for wave dominant conditions. Figure 2.11 may thus be divieded into four different quadrants: (i) river or bathymetric dominance, (ii) bathymetric dominance, (iii) wave dominance, and (iv) river dominance.

We use literature values of river plume properties to calculate L_{NF} for the Fraser [MacDonald and Geyer, 2004], Columbia [McCabe et al., 2008], and Merrimack [MacDonald and

Chen, 2012] rivers. Surf zone widths are approximated using Google Earth as the maximum distance waves break offshore in all available historical images. The channel length for these rivers is taken as the length of the jetty, as measured in a Google Earth image. All three large rivers are in quadrant (i), indicating that both bathymetric and river dominant conditions lead to freshwater escapes. This is consistent with the engineering present at these river mouths, as well as their large discharges and river mouth velocities.

The range of values for the Quinault is closer to the transition for each axis, but most data is in quadrant (i), (ii), and (iii), which is consistent with the conceptual model results for the Quinault (section 2.1.4). The modelling results of Rodriguez et al. [2018] are included (assuming $w_e \approx 10$ mm/s) for four different cases ($Q = 20\&100$ m^3/s, $H_S = 0.6\&1$ m), and lie in quadrant (iii) and (iv), indicating that for the parameter space explored in Rodriguez et al. [2018], the wave and river dominant modes are relevant. This is consistent with the scaling developped in Rodriguez et al. [2018], which predicts the escape of river water when river momentum flux is larger than wave momentum flux. This parameter space may thus be helpful to future studies in determining the fate of river water in relation to surf zone wave breaking.

2.4.4 Wave-current interaction

The surf zone width calculations (Figure 2.6b) developed in section 2.2.3do not include the effects of wave-current interaction, which has a different impact at different wavelengths. In general, an opposing current causes waves to shorten and steepen, as their wavenumber k changes to conserve absolute frequency $\omega = \sqrt{gk \tanh kd} + u \cdot k$, where u is the speed of the current [Mei, 1989]. For short waves, this steepening can lead to breaking as the Miche breaking criteria is exceeded [Miche, 1944; Zippel and Thomson, 2017]. Short waves also refract to be normal to an opposing current, and so a reasonable expectation would be that short waves would refract to be normal to the Quinault outflow before breaking as they over-steepen, while very long (i.e. infragravity) waves could propagate into the estuary [Mei, 1989; Williams and Stacey, 2016]. However, some longer waves may simultaneously refract

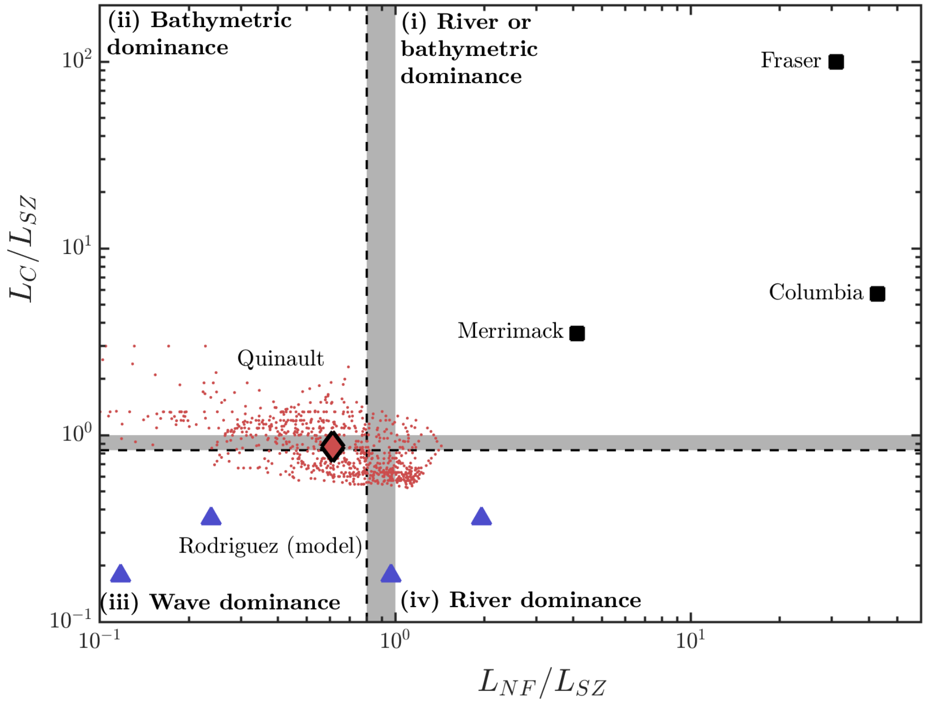

Figure 2.11: River dominance vs. wave dominance (L_{NF}/L_{SZ}) and bathymetric dominance vs. wave dominance (L_C/L_{SZ}) for different systems. Data from the Quinault is presented as small red points, with the median value represented as the black lined diamond. Four different model runs from Rodriguez et al. [2018] with varying Q and H_S are represented as blue triangles. Literature values for the Fraser, Columbia, and Merrimack are represented as black squares. Dashed lines indicate the values of m (vertical) and n (horizontal) reported in section 2.3.3. The grey shaded areas indicate the region between m or n and unity. Four different quadrants are identified using the roman numeral notation defined in section 2.4.3.

away from the deep channel extending from the river mouth.

The dominance of depth-limited breaking complicates this picture. In order to understand the effects of wave-current interaction at the Quinault, let us first consider the case in which breaking is initiated far offshore of the region of high flow near the channel during low water and/or a period of high waves ($L_{SZ} > L_C$). A wave that has already broken when it encounters the high flow region in the channel will continue to break as the channel deepens nearshore due to the opposing current, causing the surf zone to extend further onshore than shown in Figure 2.4. In the bathymetric dominance case where depth-limited breaking is initiated onshore of the region of high flow ($L_{SZ} < L_C$), we might expect the currents to play a larger role in the initiation of breaking. What is unclear, however, is where this breaking would occur. In the bathymetric dominance behavior, river water can escape minimally opposed onto the inner shelf, with currents in the range of $0.5 - 0.75$ m/s persisting onto the inner shelf as drifters escape (Figure 2.3f). Thus, shorter waves may refract towards and break against a current well offshore of L_{SZ} in this case. It is unclear whether such wave breaking would have an impact on the fate of river water, but based on section 2.4.1, the position of the current-induced wave breaking relative to L_{NF} would likely be important.

2.5 Summary

We present results from an observational study of the Quinault River, a small river that flows into the surf zone in western Washington state. We find that the interaction of the outflow and the surf zone can be characterized in terms of the plume near field length, L_{NF}, the surf zone width, L_{SZ}, and the offshore end of the channel, L_C, such that three behaviors dominate:

1. river water is trapped within the surf zone and remains fresh when $L_{SZ} > L_{NF}$ & $L_{SZ} > L_C$;

2. river water escapes the surf zone when $L_{NF} > L_{SZ}$ and mixes intensely;

3. river water escapes the surf zone when $L_C > L_{SZ}$ and mixes intensely.

We observe surf zone trapping to be the dominant behavior at the Quinault River, as only one third of drifters escape or nearly escape the surf zone, and river water is rarely observed offshore of the surf zone by nearshore moorings. Maximum drifter excursions are correlated with L_{NF}, but the predicted entrainment velocity for the Quinault River plume overestimates the drifter excursions, indicating that wave-induced turbulence may increase plume mixing. Trapped river water propagates a distance into the surf zone roughly equal to L_{NF}, at which point its fate is governed by surf zone processes. Extrapolating over the course of one year, we find that 70% of river discharge is trapped in the surf zone due to wave dominance.

Chapter 3

OBSERVATIONS OF RIVER PLUME MIXING AND TRANSPORT IN THE SURF ZONE

3.1 Introduction

Riverine transport of freshwater, nutrients, sediment, and pollutants is important to coastal environments [Hickey et al., 2010]. Small discharge rivers represent a large fraction of total river discharge in the midlatitudes [Izett and Fennel, 2018], and many such rivers empty directly into the surf zone, where surface waves break near shore due to depth limitation. Recent work has found that river discharge can often be trapped in the surf zone under these conditions [Wong et al., 2013; Rodriguez et al., 2018; Kastner et al., 2019]. These studies focus on predicting the quantity of river water that will escape the surf zone, and have not addressed the transport and mixing of trapped river water. In particular, Kastner et al. [2019] shows that river water is often trapped in the surf zone at the Quinault River mouth, on Quinault Indian Nation land by Taholah, WA, as a result of the relationship between two tidally variable quantities: the surf zone width, L_{SZ}, and the near field river plume length scale, L_{NF}, as defined in Hetland [2010]. This study uses observational data, including salinity measurements from Lagrangian drifters, from near the Quinault River mouth to investigate surf zone-trapped river plume transport and mixing processes.

3.1.1 Mixing in river plumes

Vertical mixing in river plumes is typically driven by stratified shear instability, where turbulence is initiated when vertical shear is strong enough to overcome stratification [MacDonald and Geyer, 2004; Geyer et al., 2010; MacDonald and Chen, 2012; Jurisa et al., 2016]. River plumes are often approximated as two layer flows [Fong and Geyer, 2001; Hetland, 2010; McCabe et al., 2008; Kastner et al., 2018], where stratification and shear are often highest near the base of the plume layer, resulting in the co-location of turbulence and the salinity gradient. Turbulent kinetic energy (TKE) dissipation values in river plume systems are typically of order $\varepsilon \sim \mathcal{O}(10^{-4} - 10^{-3})$ W kg^{-1} [Nash and Moum, 2005a; MacDonald et al., 2007; Jurisa et al., 2016]. Lateral mixing in river plumes is small because the aspect ratio of a river plume is typically small [MacDonald and Geyer, 2004; Chen and MacDonald, 2006;

McCabe et al., 2008; Horner-Devine et al., 2015].

The vertical Lagrangian salt balance can be expressed as

$$\frac{DS}{Dt} = \frac{\partial}{\partial z}\langle S'w' \rangle \tag{3.1}$$

where S is salinity, the notation D/Dt indicates the material derivative, the prime superscript denotes a fluctuation and w is the vertical velocity. The material derivative of salinity represents the change in salinity a small parcel of water experiences as it moves through the plume. In this formulation, the eddy diffusivity parameterizes the vertical salt flux, such that

$$\langle S'w' \rangle = K_z \frac{\partial S}{\partial z}, \tag{3.2}$$

where K_z is the eddy diffusivity of salt in the vertical direction (hereafter referred to as simply eddy diffusivity, dropping the "of salt"). Eddy diffusivity values in river plumes typically vary from $\mathcal{O}(10^{-4})$ to $\mathcal{O}(10^{-2})$ m^{2}s^{-1} [MacDonald and Geyer, 2004; McCabe et al., 2008]. Most river plume studies are primarily based on shipboard observations and Eulerian moorings, and so do not calculate DS/Dt. Drifter based plume studies have utilized a control volume technique to calculate a salt flux comparable to shipboard and mooring studies [McCabe et al., 2008; Kastner et al., 2018]. River plume salt fluxes are typically of order $\mathcal{O}(10^{-2})$ psu m s^{-1} [MacDonald and Geyer, 2004; McCabe et al., 2008; Kastner et al., 2018].

The surf zone at the Quinault River mouth is shallow, wide, and saturated with energetic breaking waves, making it an all but impossible environment to conduct traditional shipboard river plume observations. We therefore use drifter estimates of DS/Dt to quantify mixing, representing the vertically integrated salt flux by combining equations 3.1 and 3.2 (Section 3.2.2).

Mixing can also be quantified by the spatial salinity variance, $\overline{S_x'^2}$, which represents the mean deviation of salinity in a system from the mean salinity of that system [MacCready et al., 2018]. The destruction of spatial salinity variance is shown by MacCready et al. [2018] to be directly related to mixing. We develop an analogous temporal salinity variance,$\overline{S_t'^2}$, in Section 3.2.2.

3.1.2 River plumes in the surf zone

River plume water that has been trapped in the surf zone is no longer primarily forced by its initial momentum and could therefore be strongly influenced by surf-zone forcing [Wong et al., 2013; Rodriguez et al., 2018; Kastner et al., 2019]. In a saturated surf zone, waves break at a depth d proportional to their height H_s, such that $\gamma = H_s/d$ is constant throughout the surf zone. Wave height therefore decreases with depth approaching the shoreline, resulting in gradients in wave energy flux and radiation stress (flux of momentum) that cause the surf zone to be turbulent and energetic, yet retentive.

Gradients in wave energy flux in the surf zone are related to local energy loss rates [Battjes and Janssen, 1978; Thornton and Guza, 1983]. The turbulent kinetic energy (TKE) dissipation rate, ε, is high in the surf zone, with values typically of order $\varepsilon = \mathcal{O}(10^{-2})$ W kg^{-1} near the surface [Thornton and Guza, 1986; Feddersen and Trowbridge, 2005a; Feddersen, 2012b; Thomson, 2012]. The TKE dissipation rate has been found to scale with the wave height and inversely with distance from the water surface, such that dissipation is higher closer to the surface and closer to the break point.

Gradients in the wave radiation stress in the surf zone force alongshore currents ($v \sim 0.5 - 1.5$ m s^{-1}) [Longuet-Higgins, 1970; Thornton and Guza, 1986; Feddersen and Guza, 2003; Clark et al., 2010], which can be estimated using the formulation from Longuet-Higgins [1970],

$$u_{al} = \frac{5\pi}{16C_f}\left(\frac{tan\beta}{1+3\gamma^2/8}\right)\gamma\sqrt{gd}\sin\theta\cos\theta, \tag{3.3}$$

where $C_f = 0.01$ is a constant, $\tan\beta$ is an approximate beach slope, and θ is the incident wave angle relative to shore-normal. In addition to mean currents, vertical vorticity introduced by short-crested breaking waves, wave groups, and shear instability cause the formation of energetic horizontal eddies [Peregrine, 1998; Haller et al., 1999; Bowen and Holman, 1989; Clark et al., 2012; Feddersen, 2014]. These eddies mix gradients in the cross- and alongshore directions, leading to large horizontal dispersion with horizontal eddy diffusivity $K_x \approx \mathcal{O}(0.1 - 1)$ m^{2}s^{-1} [Clark et al., 2010; Spydell and Feddersen, 2012; Hally-Rosendahl et al., 2014]. A variety of measurement techniques have been used to quantify surf zone dispersion, including dye [Hally-Rosendahl et al., 2014] and drifting buoys [Spydell and Feddersen, 2012].

Despite this high dispersion, the surf zone tends to be retentive. Cross-shore circulation in the surf zone, driven by mechanisms such as Stokes' drift and undertow [Kumar et al., 2012; Lentz and Fewings, 2012], is small, resulting in minimal exchange with the inner shelf [MacMahan et al., 2004; Hally-Rosendahl et al., 2014]. Notable exceptions are rip currents, both bathymetric [Reniers et al., 2009; MacMahan et al., 2010; Moulton et al., 2017] and transient [Clark et al., 2012; Hally-Rosendahl et al., 2014; Kumar and Feddersen, 2017a]. Additionally, the surf zone has often been shown to be unstratified due to vertical turbulence; horizontal processes are therefore considered to be the primary mechanism for dispersion within the surf zone [Feddersen and Trowbridge, 2005b; Feddersen, 2012a; Hally-Rosendahl et al., 2014].

Outside of the surf zone, several recent studies have shown that surface wave breaking can affect plume mixing in deeper water. Breaking waves can significantly contribute to river plume mixing when the plume layer is shallow and slow moving far from the river mouth [Gerbi et al., 2015a], or when strong wave breaking is co-located with a plume front [Thomson et al., 2014]. Breaking waves can impact the structure of a river plume far from the river mouth where the plume propagates as a buoyant coastal current [Gerbi et al., 2013a], but these effects are less important closer to the mouth where river momentum is large [Akan et al., 2017a; Kastner et al., 2018]. The impact of depth-limited wave-driven turbulence has not been similarly assessed, but Kastner et al. [2019] suggest that breaking waves increase plume entrainment velocity at the Quinault River mouth.

In this study, we will assess the mixing and transport of river plume water that has been trapped in the surf zone. We make use of drifters following the trapped plume water and moorings at the edge of the surf zone. These measurements allow us to make calculations of stratification, DS/Dt, and $\overline{S_t'^2}$, and to develop a conceptual framework for the evolution of surf zone freshwater content based on alongshore surf zone transport (Section 3.2). Specifically, we will show that the surf zone near the Quinault River mouth can be highly stratified, and that DS/Dt depends on the stratification. This dependence results in a reasonable approximation of eddy diffusivity K_z near the Quinault River mouth. Changes in surf zone stratification, and therefore DS/Dt, are driven by changes in the surf zone freshwater content. The freshwater content of the surf zone decreases as river discharge decreases and surf zone alongshore currents increase, resulting in a net transport of freshwater away from the river mouth, an increase in stratification, and an increase in DS/Dt as strong salinity gradients are exposed to high wave-breaking turbulence near the water surface (Section 3.3). These results suggest the importance of alongshore currents in predicting changes in the surf zone salinity structure and the mixing and transport of river water in the surf zone (Section 3.5).

3.2 Methods

3.2.1 Observations

The data presented here were collected as part of an observational campaign at the Quinault River mouth described in detail by Kastner et al. [2019] (figure 3.1). We focus in this work primarily on measurements from the SWIFT (Surface Wave Instrument Float with Tracking) drifting buoys deployed in the river inlet. Two models of SWIFTs were used, as detailed in table 3.1. Figure 3.2 shows raw, high resolution observations of salinity (figure 3.2b), drift speed (figure 3.2c), and heave (figure 3.2d), as well as estimates of TKE dissipation rate (figure 3.2e) from a SWIFTv3 that escaped the surf zone on 28 April 2017. This combination of measurements effectively resolves wave-driven processes, plume dynamics, and mixing on time scales varying from seconds to the duration of a given drift. We use nearshore moorings with YSI Sonde 600LS CTD sensors ~ 1 and ~ 3 m below the water surface deployed at the edge of the surf zone in ~ 4 m water depth (relative to mean lower low water at the USGS Pt. Grenville station) to constrain the offshore salinity field. At the boundaries of the surf zone-plume system, we use measurements of spectral wave properties from a Nortek Acoustic Waves And Currents (AWAC) instrument deployed in ~ 6 m water depth as an offshore wave condition as well as a downlooking Nortek Aquadopp and bottom mounted Onset HOBO pressure sensor deployed at the river mouth to capture the river momentum and volume flux. The results presented in section 3.3.1 use data from the entire two week study period.

Model	Version 3	Version 4
Draft (m)	0.25	1.05
No. of CTs	1	3
CT depth (m)	0.2	0.1, 0.5, 1.05
ADCP Model	Aquadopp HR (2 MHz)	Signature (1 MHz)

Table 3.1: The instrumentation and specifications of the two versions of SWIFT drifters used during the Quinault observational campaign.

Case Study: 30 April 2017

Additional insights on the surf zone salinity evolution are based on the concurrent deployment of one SWIFTv3 and one SWIFTv4 on 30 April 2017 (sections 3.3.2, 3.3.3, & 3.4.2). Wave conditions, river discharge, and tidal range were close to average for the two week deployment on this day (table 3.2). The drifters were deployed in the river mouth at low water tidal stage, and recirculated in a region within ~ 500 m to the south of the river mouth for a period of 5 hours before beaching (until almost high water tidal stage). A similar event occurred on 05 May 2017, but the SWIFTs deployed on that day did not have functioning CT sensors. Both of these events occurred during normal wave conditions for our deployment period and for different river discharges, suggesting that this recirculation may be a common feature at the Quinault River mouth.

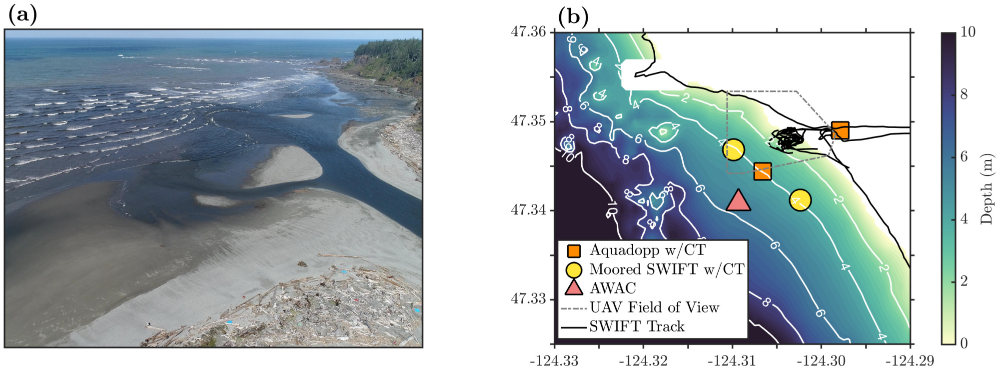

Figure 3.1: The observational field campaign at the Quinault River mouth. Panel (a) is an example UAS perspective image from April 28, 2017, when the offshore wave height $H_s = 1.62$ m, the river volume flux $Q_t = 181$ m^3 s^{-1}, and the tidal stage $\eta = -0.41$ m. Panel (b) shows a map of deployed instruments and bathymetry. Color indicates depth, and isobaths are given as white lines with notations in meters. Orange squares indicate moorings using Nortek Aquadopp ADCPs, yellow circles indicate moorings using SWIFTs, and the red triangle indicates the offshore AWAC. The UAS field of view is given as a dashed-dotted grey line, and SWIFT drift tracks on 30 April 2017 are solid black lines.

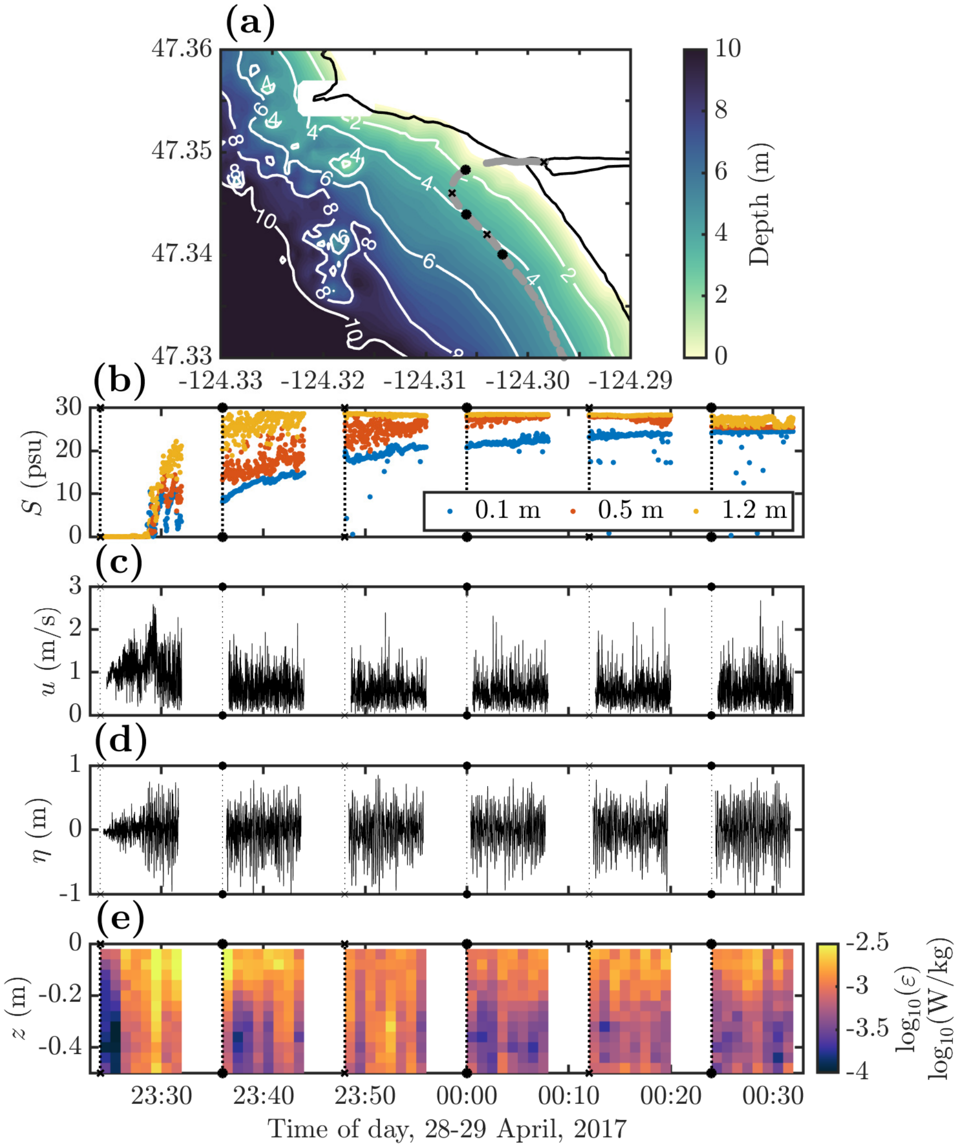

Figure 3.2: Data from SWIFT 17 on 28 April 2017, an escape from the surf zone. Panel (a) shows the drift track overlaid on the bathymetry map from figure 3.1b; panel (b) shows the 0.5 Hz salinity data at 0.1, 0.5, and 1.05 m depth; panel (c) shows the raw 4 Hz drift speed data from the GPS; panel (d) shows the raw 15 Hz inertial measurement unit heave data; panel (e) shows structure function estimates of TKE dissipation rate from 1 minute of uplooking Aquadopp HR ADCP data [Thomson, 2012; Thomson et al., 2019]. Alternating crosses and circles indicate the beginning of each SWIFT data collection burst shown on panels b-e.

	All observations			30 April 2017		
Quantity	Mean	Min	Max	Mean	Min	Max
H_s (m)	1.64	1.00	2.3	1.81	1.51	2.05
Q_R (m^3 s^{-1})	156	217	114	139	139	140
η (m)	1.31	-0.53	2.89	0.74	-0.40	1.98

Table 3.2: Conditions over the course of the entire Quinault field campaign and on 30 April 2017. Significant wave height. H_s is calculated from the AWAC, River discharge, Q_R, is calculated as 150% of the Quinault Lake discharge per information from the Quinault Nation Division of Natural Resources, and tidal stage η in m above lower low water is taken from the USGS Point Grenville tide gage.

3.2.2 Estimating mixing and stratification in the surf zone

We will use drifter measurements of salinity to quantify mixing with two estimates: the material derivative of salinity, DS/Dt, and the temporal salinity variance, $\overline{S_t'^2}$. These are not commonly used means of quantifying river plume mixing, but can be estimated from a single drifter and are therefore robust to the environmental constraints of the Quinault River mouth.

The material derivative of salinity, DS/Dt, can be calculated for each salinity sensor on a SWIFT drifter, either at 3 depths for the SWIFTv3 (0.1, 0.5, and 1.05 m) or at 0.2 m for the SWIFTv4. We apply a third order median filter to minimize the influence of bubbles, which cause spurious low salinity spikes in the raw data collected at 0.5 Hz, and obtain robust 1-minute ensemble values of salinity. We calculate DS/Dt as the slope of a linear best fit to a 1 minute time series of salinity data from each SWIFT CT sensor (figure 3.3a). We assume that an approximation of local linearity is reasonable over the 1 minute period. We exclude very fresh water, where $S < 0.5$ psu, from fits. This occurs near the beginning of drift tracks.

The SWIFT buoys are not perfectly Lagrangian tracers. This can be partially quantified by comparing the drift speeds of the two versions of the SWIFT, the larger 1.05 m draft SWIFTv3 and the smaller 0.3 m draft SWIFTv4. Note that this comparison accounts for the different in SWIFT draft, but cannot account for non-Lagrangian bias in the SWIFTv4 measurements. After applying this comparison, we exclude values of $DS/Dt < 1 \times 10^{-4}$ psu s^{-1} from our analysis (1% of DS/Dt values). This represents the overestimation of salt flux caused by the larger draft of the v3 SWIFT, as the v3 SWIFT is $\sim \mathcal{O}(10^{-2})$ m s^{-1} slower than the smaller draft v4 SWIFT. The salt flux threshold is found by multiplying this velocity difference by the cross-shore salinity gradient, $\partial S/\partial x \sim \mathcal{O}(10^{-2})$ psu m^{-1} (see sections 3.5.2 & 3.7).

Using the SWIFTv3 measurements of salinity at three vertical positions, we calculate a local stratification, $\partial S/\partial z$, as the slope of a linear salinity profile. This stratification will be used alongside DS/Dt in section 3.3.3 to calculate a vertical eddy diffusivity of salt. We estimate vertical eddy diffusivity, K_z, from the Lagrangian salt budget (eq. 3.1). Vertically integrating DS/Dt, measured at each SWIFTv3 CT sensor, and dividing by $\partial S/\partial z$, yields an expression for the vertical eddy diffusivity in the top 1.05 m:

$$K_z = \left(\int \frac{DS}{Dt} dz \right) \Big/ \frac{\partial S}{\partial z}. \tag{3.4}$$

We can therefore calculate K_z for each 1 minute SWIFT average calculation of DS/Dt and $\partial S/\partial z$.

We define $\overline{S_t'^2}$ as the mean of the squared differences of the median filtered salinity value from the fitted salinity value, such that

$$\overline{S_t'^2} = \frac{1}{f_s T_{win}} (S(t) - S_{fit}(t))^2, \tag{3.5}$$

where $f_s = 0.5$ Hz is the CT sampling frequency, $T_{win} = 60$ s is the averaging window, $S(t)$ is the median filtered salinity at a time t within the window, and $S_{fit}(t)$ is the linear salinity fit found in order to calculate DS/Dt, evaluated at the same time t. Propagating error from the SWIFT's onboard Aanderaa 4319 CT sensor (precision of 0.03 psu) indicates that this

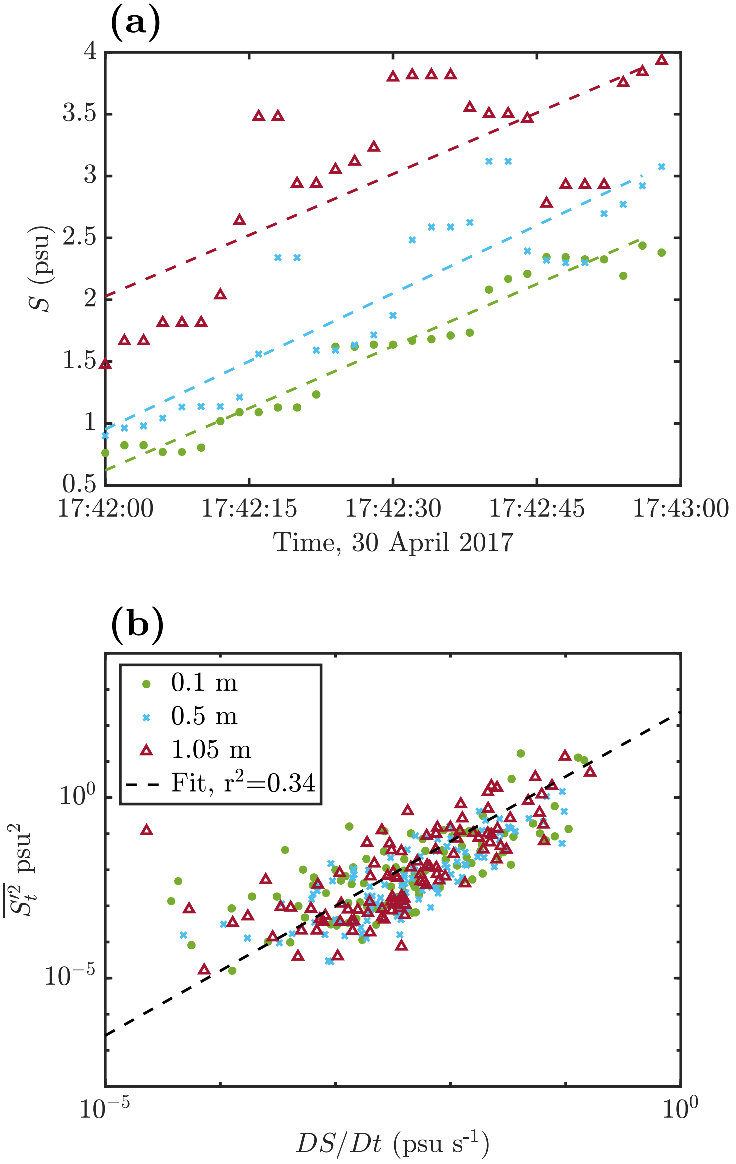

Figure 3.3: Estimates of DS/Dt and $\overline{S'^2}$ using salinity observations from a SWIFTv3 deployed on 30 April 2017. Panel (a) shows median filtered salinity data and the linear fits used to calculate DS/Dt at each CT sensor depth, as indicated by symbols (all $r^2 > 0.99$); panel (b) shows the comparison of $\overline{S_t'^2}$ and DS/Dt for each CT sensor depth (indicated by symbols) for all SWIFTv3 1-minute averages on 30 April 2017.

calculation will be in error by $sim2\%$ of the calculated value. The temporal salinity variance as defined above represents the scatter around the linear fit DS/Dt. In our calculations, we assume that our one minute averaging window and salinity thresholds are sufficient to achieve local linearity. In this case, $\overline{S_t'^2}$ only represents the scatter around the best fit line. If instrument noise and non-Lagrangian bias are small, then the local turbulent fluctuations dominate $\overline{S_t'^2}$, and we expect $\overline{S_t'^2}$ to be related to DS/Dt, as shown in figure 3.3b.

This temporal salinity variance is similar to the spatial salinity variance introduced by MacCready et al. [2018] in that it is a squared salinity residual, but differs in that intense mixing is indicated by high $\overline{S_t'^2}$, whereas a sharp decrease in spatial salinity variance indicates intense mixing.

3.2.3 Estimating and scaling surf zone turbulence

In section 3.3.3, we compare SWIFTv4 estimates of TKE dissipation rate to previously developed models of the vertical variability of surf zone turbulence. SWIFT TKE dissipation rate estimates use a structure function method to estimate ε in the top 1.05 m (SWIFTv4) of the water column [Thomson, 2012; Thomson et al., 2019]. Terray et al. [1996] uses a power law scaling dependent on the significant wave height and a surface flux of TKE which Feddersen [2012a] takes as the wave energy flux gradient, $\partial F/\partial x$. This scaling is given by

$$\frac{\varepsilon H_s}{\partial F/\partial x} = A_T\left(\frac{z}{H_s}\right)^{\lambda}, \tag{3.6}$$

where A_T and λ are fitted constants. Feddersen [2012b] uses a scaling based on water depth,

$$\frac{\varepsilon d}{\partial F/\partial x} = A_F e^{\alpha\zeta}, \tag{3.7}$$

where A_F and α are fitted constants and $\zeta = (d-z)/d$ is a transformed depth coordinate.

We fit both models to 30-minute averages of dissipation estimates in the top 1.05 m of the water column, as well as to all of these averages (figure 3.9). For the Feddersen [2012b] scaling, we take d to be the 30 minute average depth measurement from the SWIFTv4

AD2CP echosounder, and for the Terray et al. [1996] scaling, we take the 30 minute average of H_s as calculated in section 3.3.2. The SWIFT measurements do not resolve the wave energy flux gradient, so we use a mean value for $\partial F/\partial x$ over the course of the day,

$$\frac{\partial \vec{F}}{\partial x} = \frac{\rho g^{3/2} \gamma^2 d_b^{5/2}}{16 L_{SZ}}, \tag{3.8}$$

where $\vec{F}$ is the wave energy flux, determined using the AWAC wave measurements on 30 April 2017.

3.3 Results

3.3.1 Cross-shore structure

High wave forcing at the Quinault River mouth results in river water being mostly trapped in the surf zone during our observational period [Kastner et al., 2019]. Salinity measurements from all surf zone trapped SWIFT drifters over the course of the entire study period show that the surf zone can remain fresh ($S < 5$ psu), while salinity measurements from the nearshore moorings are significantly higher ($S > 25$ psu) (figure 3.4a). The deepest SWIFTv3 salinity measurements (1.05 m) are frequently more than 10 psu fresher than the shallowest mooring salinity measurements (~ 1 m). Salinity does not vary significantly in the cross-shore direction within the surf zone, resulting in a large horizontal cross-shore salinity gradient near the surf zone edge when the surf zone salinity is low.

Calculations of stratification (section 3.2.2) indicate that the surf zone can be stratified (figure 3.4b). Specifically, the stratification in the upper 1.05 m of the surf zone reaches higher values than the offshore stratification between 1 and 3 m. This differs from surf zone studies conducted far from river mouths, which have shown the surf zone to be unstratified (e.g. Feddersen and Trowbridge [2005b]; Kumar and Feddersen [2017b]), however, these studies have not included the effects of river discharge. We do not observe any significant cross-shore trend in surf zone stratification.

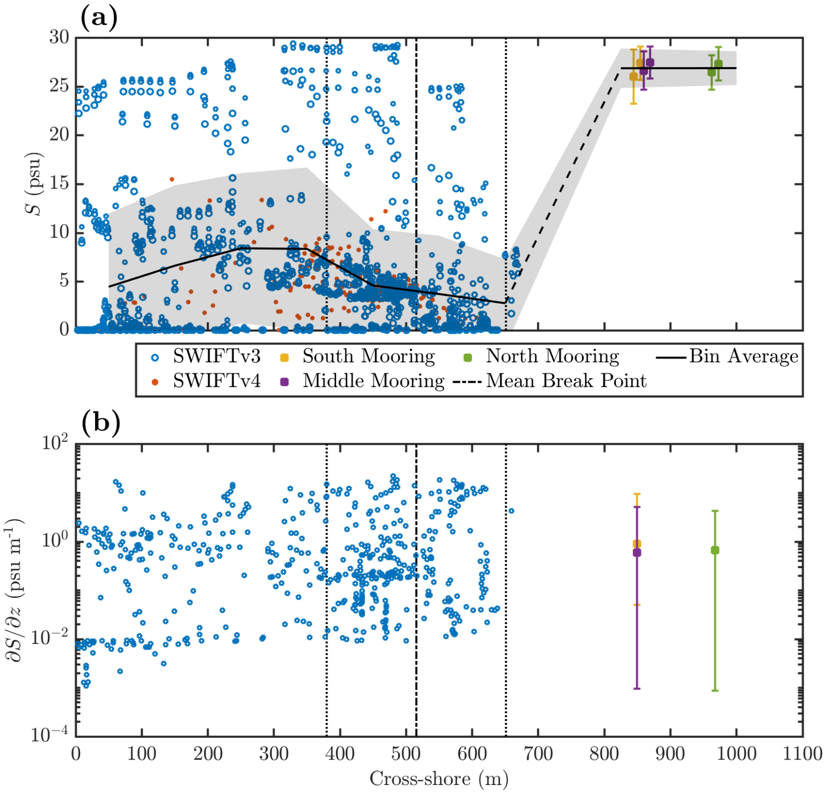

Figure 3.4: Cross-shore profiles of quantities measured from trapped SWIFT drifters and nearshore moorings at alongshore positions less than 1500m from the river mouth. Panel (a) shows the 1-minute average salinity from v3 and v4 SWIFTs, as well as the deployment average salinity for the nearshore moorings, with error bars indicating standard deviation. The depth of the v3 SWIFT CT sensors are indicated by decreasing marker size, with the largest marker indicating the measurement closest to the surface (0.1 m) and the smallest indicating the deepest measurement (1.05 m). There are two points for each mooring, offset in the horizontal for clarity; the fresher point for each mooring is the 1m CTD, and the saltier is the 3m CTD. The black line shows a cross-shore bin average with a bin size of 100 m; the shaded area represents the standard deviation of salinity in each bin. Panel (b) shows the near-surface stratification from the v3 SWIFTs along with the mean and range of mid water column stratification from the moorings. The mean surf zone width is given by the black dashed vertical line, with the black dotted lines indicating one standard deviation from the mean break point.

3.3.2 Surf zone observations

Drifters deployed on 30 April 2017 entered a surf zone eddy and recirculated for a period of over 4.5 hours, spanning most of the time from low water to high water tidal stage. At the Quinault, discharge from the river mouth, Q_T, is maximum at low water, and minimum at high water (figure 3.5a). We calculate the tidal volume flux through the river mouth as

$$Q_T = u_T d_T b_T, \tag{3.9}$$

where u_T is the tidally varying velocity at the river mouth, d_T is the tidally varying river mouth depth, and the effective river mouth width $b_T \approx 87$ m is defined as in Kastner et al. [2019]. The surf zone is also widest at low water (given a constant wave condition) due to the concave shape of the beach [Kastner et al., 2019]. Measurements of salinity from drifters trapped in the surf zone show that minimum salinity occurs at low water, when the drifters are deployed, and increases with the tidal stage (figures 3.5b & 3.6). Salinity at the moorings also increases with tidal stage during this time period (particularly at the south mooring)(figures 3.5b & 3.6). Coincident with increasing salinity in the surf zone, estimates of stratification using drifter measurements of salinity increase with tidal stage (figure 3.5c). At the moorings, stratification between 1 and 3 m decreases with tidal stage (figure 3.5c). Water at the moorings is always saltier than in the surf zone. So, from low to high water on 30 April 2017, the surf zone transitions from fresh and unstratified to saltier and stratified.

Near surface velocity in the surf zone, as observed by SWIFT drifters, increases with tidal stage throughout the drifter deployment (figure 3.5d). The initial momentum of the drifters is set by the river flow, which decreases with tidal stage. Similarly to the near surface velocity, the wave height measured by the drifters increases over the duration of the drifter deployment as the offshore wave height increases (figure 3.5e). We calculate the significant wave height as $H_s = 4\sigma_z$, the standard deviation of the sea surface elevation measurements from the SWIFT inertial measurement unit, sampling at 16 Hz. The increase of near surface velocity with wave height suggests that the eddy in which the drifters recirculated was a wave-driven feature.

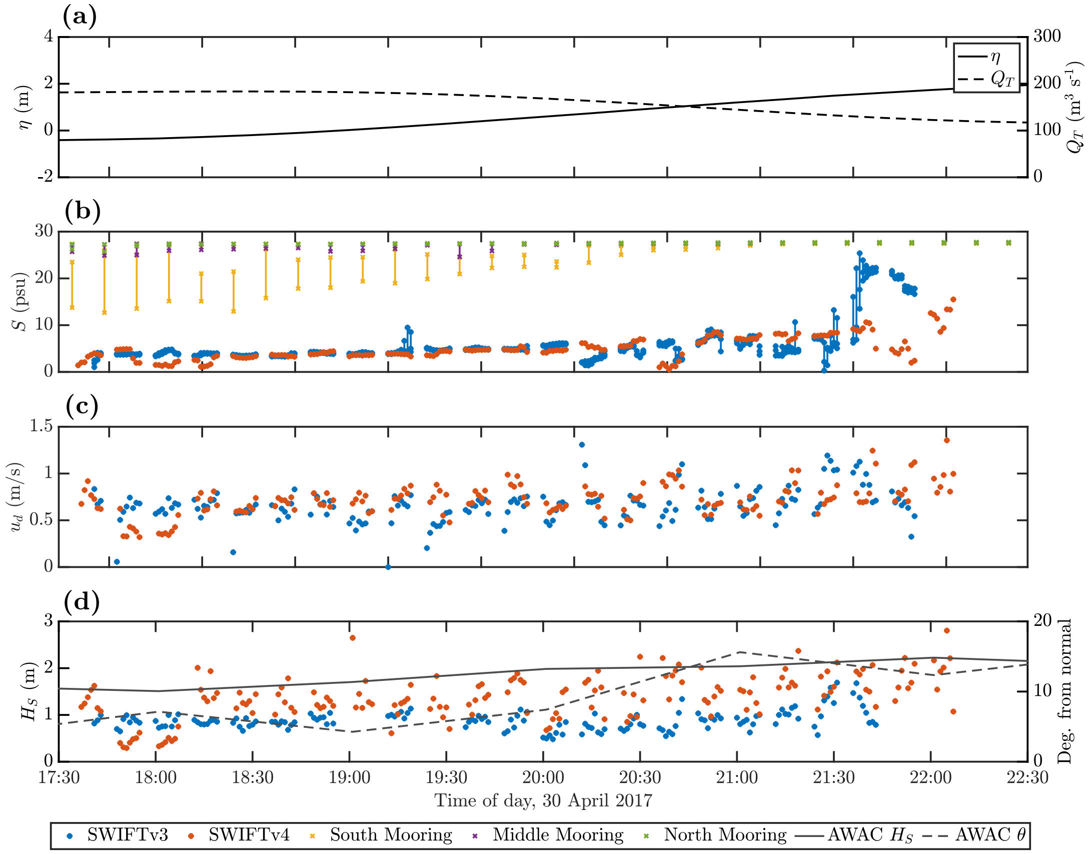

Figure 3.5: Time series of SWIFT and mooring measurements on 30 April 2017. Panel (a) shows tidal stage in meters above mean lower low water from the USGS Point Grenville station and tidal river volume flux reconstructed from the river mouth mooring using the Matlab *utide* codes [Codiga, 2011]. Panel (b) shows SWIFT v3, SWIFTv4, and mooring measurements of salinity, with the range between the top and bottom measurement for each shown as a solid line. Panel (c) shows SWIFT drift speed; panel (d) shows wave height calculated from SWIFT heave measurements and offshore AWAC wave spectra on the left axis and wave direction from the offshore AWAC wave spectra on the right axis in degrees from shore normal.

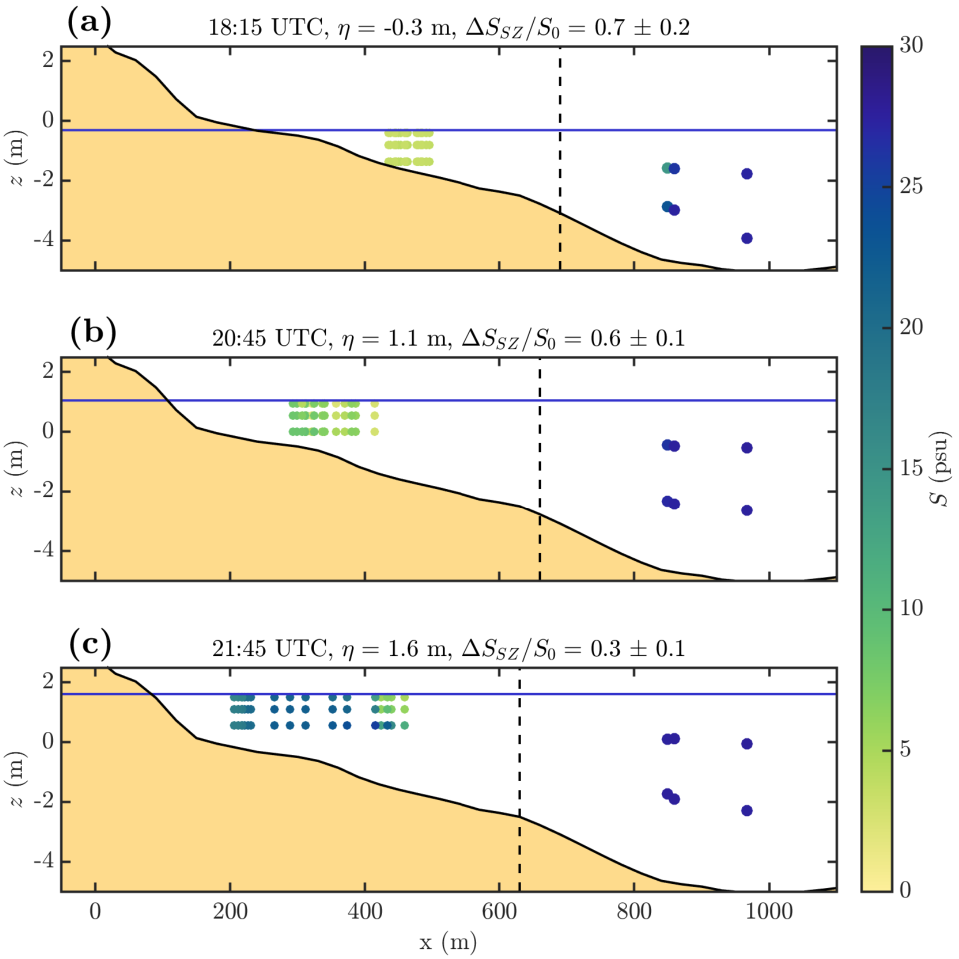

Figure 3.6: Color scatter plots showing the salinity structure across the surf zone to the inner shelf as measured by the SWIFTv3 and the moorings. Time advances, and tidal stage increases, from panel (a) to panel (c), which show 30-minute averages around that tidal stage. The solid black line and tan filled region indicate the seabed, with depth that changes as the tide increases, and the vertical dashed black line indicates the surf zone width. The colored dots inside the surf zone indicate the salinity measured the SWIFTv3, while the colored dots outside the surf zone indicate the salinity measured by the moorings, showing all measurements within the 30-minute averaging window. The mooring data points are shown larger to emphasize that they are 30 minute average salinity values, as opposed to the one minute SWIFT data. The dashed black line indicates the break point position. The uncertainty interval generated by this method is shown in the title of each plot.

3.3.3 Turbulence and mixing in the surf zone

The dependence of salinity on tidal stage leads to dependencies of $\partial S/\partial z$, DS/Dt, and $\overline{S_t'^2}$ on tidal stage. Both mixing estimates, DS/Dt and $\overline{S_t'^2}$, increase with tidal stage, as observed for $\partial S/\partial z$ (figure 3.7a-b). TKE dissipation rate estimates from the SWIFTv4 show that ε does not increase with tidal stage (figure 3.7c). Therefore, DS/Dt and $\overline{S_t'^2}$ increase irrespective of ε, corresponding instead to an increase in $\partial S/\partial z$. This differs from many river plume studies, which have shown more intense mixing to occur in regions with higher TKE dissipation rate [McCabe et al., 2008; Jurisa et al., 2016; Geyer et al., 2017; Kastner et al., 2018].

Estimates of K_z over the SWIFT deployment on 30 April 2017 have considerable scatter, but show no significant trend with tidal stage (figure 3.7d). The mean of the 1 minute average estimates of eddy diffusivity during the 30 April 2017 deployment is 12×10^{-3} m^{2}s^{-1} or 8×10^{-3} m^{2}s^{-1}, using normal and log-normal calculations, respectively. We observe no significant dependence of K_z on quantities that increase over the drifter deployment, such as salinity, near-surface velocity, or wave height, as indicated by the fact that K_z does not vary over the deployment.

The vertical eddy diffusivity can also be calculated by fitting the relationship between the vertically integrated Lagrangian mixing rate and stratification using a linear trend line with no y-intercept. The slope of this line will be the eddy diffusivity (following equation 3.4). When calculated, this fit shows an eddy diffusivity of 5.7×10^{-3} m^{2}s^{-1} , with a modest correlation of $r^2 = 0.28$ (figure 3.8). This suggests that a constant vertical eddy diffusivity reasonably parameterizes vertical mixing in the surf zone. The values of K_z reported above fall in the upper range of previous values of eddy diffusivity in river plumes (typically $\mathcal{O}(10^{-4})$ to $\mathcal{O}(10^{-2})$ m^{2}s^{-1}) [MacDonald and Geyer, 2004; McCabe et al., 2008], and are the first estimates of the vertical eddy diffusivity of salt in the surf zone, where lateral dispersion has been shown to be dominant [Clark et al., 2010; Spydell and Feddersen, 2012; Hally-Rosendahl et al., 2014]. The scatter around the fit estimated eddy diffusivity in figure 3.8 is not dependent on tidal stage or quantities that vary over the course of the tidal cycle,

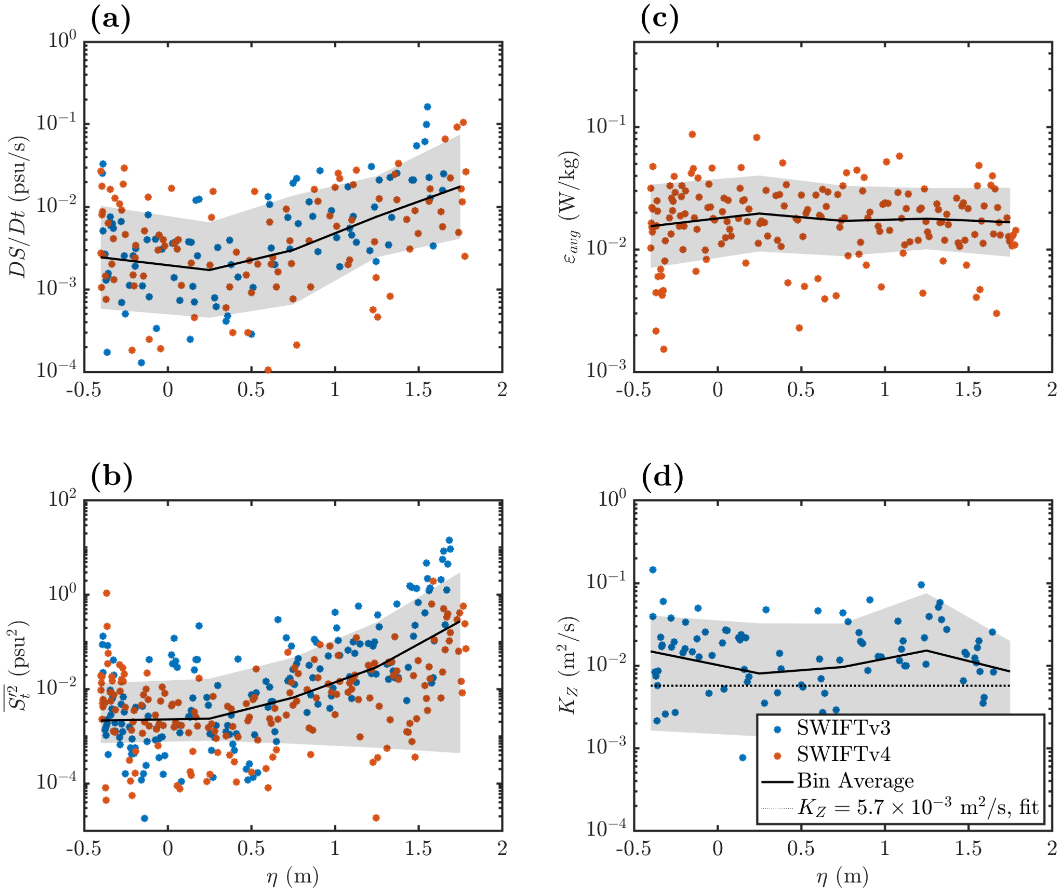

Figure 3.7: Calculations of (a) DS/Dt for SWIFTv3 and v4, and (b) $\overline{S_t'^2}$ for SWIFTv3 and v4; estimates of (c) TKE dissipation rate from the SWIFTv4 and calculations of (d) the eddy diffusivity for each 1 minute SWIFT burst using equation 3.4, all plotted against tidal stage. The black line on each plot indicates a bin average in tidal stage, using a bin size of 0.5 m and a log-normal mean. The shaded area indicates the log-normal standard deviation from the bin average.

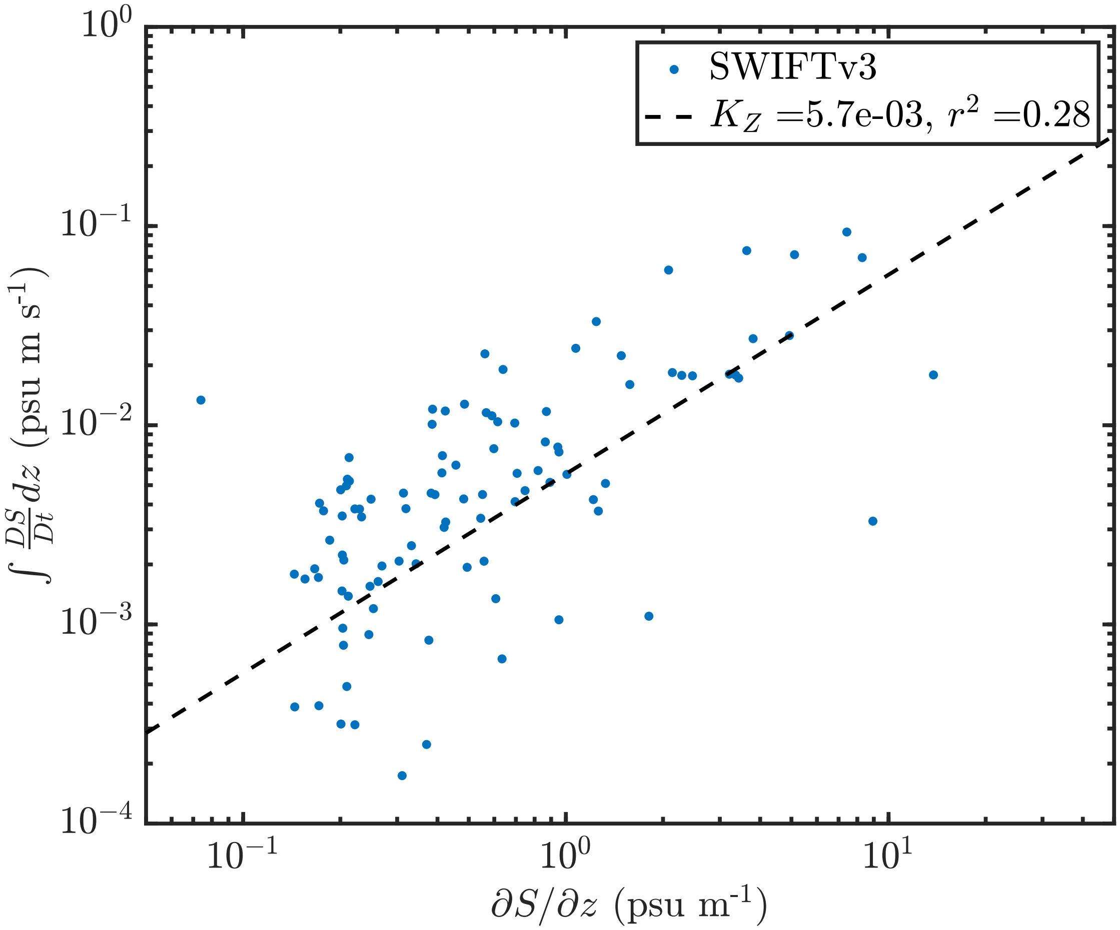

Figure 3.8: Eddy diffusivity is estimated as the slope of the linear fit between the vertically integrated Lagrangian mixing rate on the y-axis and the stratification on the x-axis. SWIFTv3 data is shown as blue data points, the fit is shown as a dashed black line.

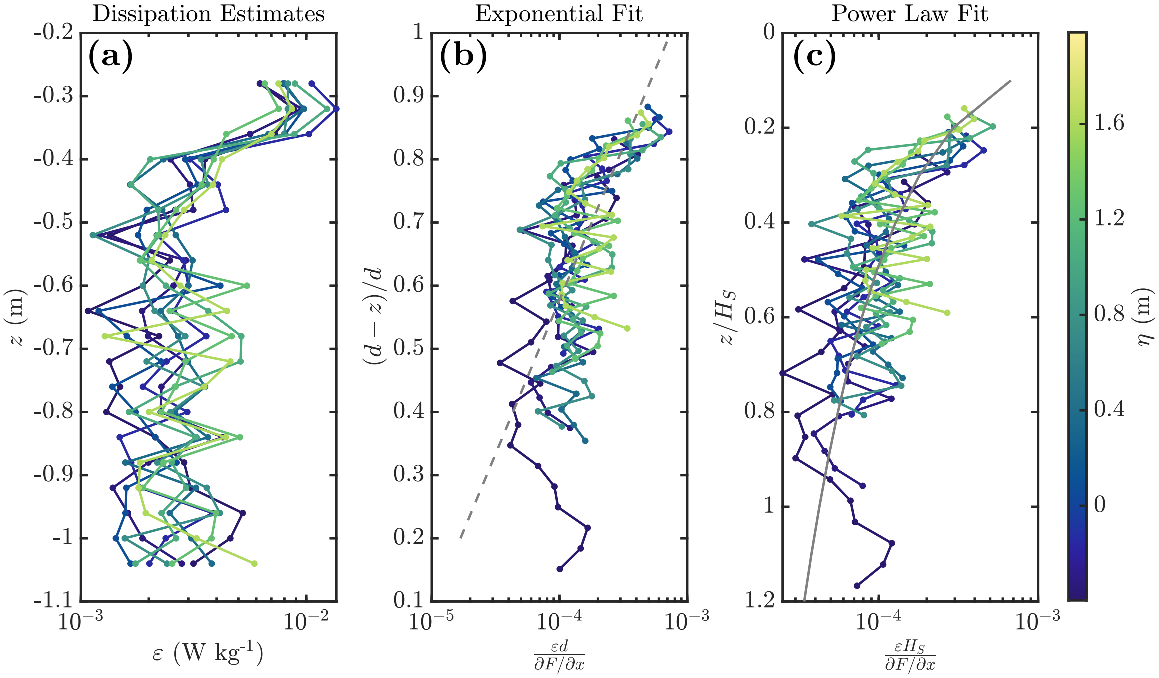

Figure 3.9: The vertical structure of surf zone turbulence. Panel (a) shows the average dissipation rate profiles over 30 minute bins, panel (b) applies the exponential scaling from Feddersen [2012b], and panel (c) applies the exponential scaling from Terray et al. [1996] as modified by Feddersen [2012a]. The color of the profile indicates the tidal stage during that bin, and the fits to all the data are shown as solid grey lines.

further indicating that K_Z may be approximated as constant (not shown). Neither K_z nor the TKE dissipation rate have a significant trend over the course of the deployment, and so while we do not observe a direct dependence between K_z and ε, a dependence cannot be explicitly ruled out. The vertical structure of ε in the presence of stratification is described below.

The vertical structure of surf zone turbulence has not previously been assessed in the presence of stratification. Since stratification varies by two orders of magnitude over the course of this time period, we will compare the performance of the vertical models for wave-driven turbulence developed by Terray et al. [1996] (equation 3.6) and Feddersen [2012b] (equation 3.7) to investigate whether deviations may be attributable to changes in stratification (figure 3.9). Both models fit SWIFTv4 dissipation estimates well, similar to findings from Zippel and Thomson [2015]. The power law scaling from Terray et al. [1996] has a correlation $r^2 = 0.56$ from all dissipation estimates, with a range of $0.34 < r^2 < 0.75$. The exponential scaling from Feddersen [2012b] has a correlation $r^2 = 0.46$ from all dissipation estimates, with a range of $0.25 < r^2 < 0.69$. There is no significant change in the performance of either model as stratification increases from low to high water, indicating that the presence of near-surface stratification does not inhibit wave-driven turbulence.

3.4 Evolution of the surf zone freshwater content

Mixing requires turbulence to interact with a gradient. In the surf zone, turbulence will always be present and energetic due to breaking waves. We show in sections 3.3.2 and 3.3.3 that surf zone stratification varies with the tide, which results in tidally variable DS/Dt and $\overline{S_t'^2}$. The increased stratification and salinity indicates that the surf zone freshwater content has decreased, or that freshwater has been exported from the region near the river mouth. Here, we develop a conceptual framework to explain the export or accumulation of freshwater in the surf zone near a river mouth and apply it to the Quinault River system.

3.4.1 Conceptual framework

To develop a conceptual framework for the evolution of the surf zone freshwater content, we consider the surf zone volume budget in a control volume near the river mouth,

$$\frac{\partial V_{SZ}}{\partial t} = Q_{in} - Q_{out} + Q_B, \tag{3.10}$$

where Q_{in} and Q_{out} are alongshore fluxes into and out of the surf zone volume V_{SZ} and Q_B is an effective flux caused by the break point moving in the cross-shore direction due to changing wave conditions or tidal water level variability. The volume V_{SZ} includes the river mouth, as shown in figure 3.10a, and extends alongshore of the river mouth for a distance

B_{SZ}. The surf zone is allowed to migrate onshore and offshore with the tide. As V_{SZ} is set only by wave dynamics and tidal depth variability, the alongshore volume fluxes are equal such that $Q_{in} = Q_{out}$. In order to constrain the surf zone freshwater balance, we examine the magnitudes of the volume fluxes into and out of V_{SZ}.

We define the cross-shore break point volume flux as $Q_B = v_b d_b B_{SZ}$, where v_b is the velocity at which the break point translates. Taking representative values of $v_b \approx 0.01$ m s^{-1} (100 m in 2 hours), $d_b \approx 3$ m, and $B_{SZ} \approx 300$ m yields $Q_B \sim 10$ m^3 s^{-1}. This scaling matches the calculations from the Quinault data (see section 3.4.2).

The alongshore volume fluxes into and out of the surf zone volume can be due to two processes: alongshore flow driven by the wave radiation stress gradient, Q_A, and trapped river discharge, Q_T. The alongshore surf zone transport due only to wave forcing is $Q_A = u_{al} A_{SZ}/2$, where u_{al} is the value of the wave-driven alongshore current at the break point (equation 3.3) and A_{SZ} is the cross-shore cross-sectional area of the surf zone. This volume flux is agnostic to the presence of freshwater, but can act to transport any freshwater present in the surf zone. Therefore, $Q_{in} = Q_{out} = Q_A + Q_T$. The alongshore current transport at the Quinault is on average $Q_A \sim 300$m^3 s^{-1}, and Q_T scales with the river discharge, on average 150 m^3 s^{-1}. Therefore, Q_B is negligible compared to Q_A and Q_T (figure 3.10a).

Now, we examine the evolution of the surf zone freshwater fraction in such a system. We assume that cross-shore exchange due to Stokes'drift, undertow, and estuarine circulation is small[Kumar et al., 2012; Lentz and Fewings, 2012; Geyer and MacCready, 2014]. We allow cross-shore salt flux, $S'Q'$, due to eddies at the edge of the surf zone, which can be responsible for both incorporating ambient inner shelf water into the surf zone ($S'_{in}Q'$) and for ejecting fresher surf-zone water offshore ($S'_{out}Q'$). Note that Q' is a volume flux associated with a cross-shore exchange velocity and does not contribute to the surf zone volume budget.

We also assume that mixing in the volume V_{SZ} is ideal, such that the mean salinity of the outflowing alongshore mass flux in the surf zone is assumed to be equivalent to the mean salinity in the surf zone control volume V_{SZ}. In order for this to be true, the flow in the control volume must be barotropic. We therefore assume baroclinic processes to be small

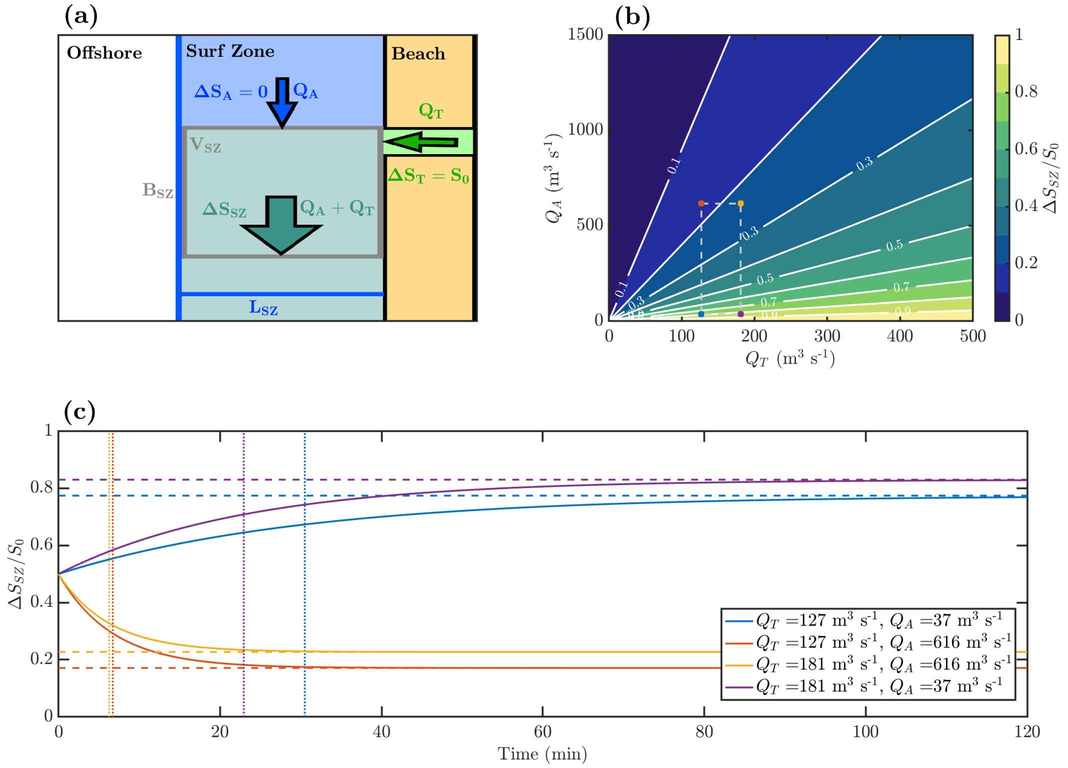

Figure 3.10: A schematic (a), the parameter space (b), and example time series (c) for the conceptual framework presented in section 3.4.1. Panel (a) shows the control volume described in the derivation of equation 3.13; panel (b) shows the steady-state freshwater fraction $\Delta S_{SZ}/S_0$ as a function of Q_A and Q_T, with the range of values present at the Quinault shown as the light grey dashed box; panel (c) shows example time series of equation 3.13 for the end members of the range of values present at the Quinault, matching line color to points on the corners of the grey box in panel (b). Horizontal dashed lines show the asymptotic limit for each case, and vertical dotted lines show the adjustment time τ for each case. The surf zone volume is taken as a representative value from 30 April 2017, $V_{SZ} = 3 \times 10^5$ m^3. An initial value of $\Delta S_{SZ}/S_0 = 0.5$ is used for all examples, allowing the calculation of $\mathcal{C}$.

relative to barotropic processes, as the wave-driven alongshore current is barotropic, and freshwater trapped due to cross-shore processes has lost most of its initial momentum. This treats the surf zone as analagous to a continuously stirred reactor (CSR), as the average salinity at the boundary of V_{SZ} is the average salinity of the volume V_{SZ} [Metcalf et al., 1979; Davis and Davis, 2003; Tchobanoglous et al., 2014].

We express the surf zone freshwater content as the freshwater fraction: the percentage of the surf zone volume, V_{SZ}, occupied by water fresher than a reference salinity S_0. The average freshwater fraction within the volume V_{SZ} is $\Delta S_{SZ}/S_0$, where the average surf zone salinity anomaly is defined as

$$\Delta S_{SZ} = \frac{1}{V_{SZ}} \iiint\limits_{V_{SZ}} (S_0 - S) dV. \tag{3.11}$$

It is possible to fill the region V_{SZ} with freshwater; when this occurs there can be no mixing within V_{SZ}.

By assuming ideal mixing, ΔS_{SZ} is the salinity anomaly associated with all outflows from the control volume. The salinity anomalies associated with the river flow, ΔS_T, the alongshore current, ΔS_A are similarly the average anomaly associated with the fluxes into the surf zone volume. Figure 3.10a shows a diagram of the freshwater budget in the surf zone control volume. Kastner et al. [2019] show the Quinault to be fully fresh at its mouth, so $\Delta S_T/S_0 = 1$. We assume that $S_A = S_0$, such that $\Delta S_A/S_0 = 0$ (figure 3.10a). The salinity anomalies associated with cross-shore exchange processes can be similarly assessed. Assuming that the salinity of the ambient inner shelf water is given by $S'_{in} = S_A$, so $\Delta S'_{in}/S_0 = 0$. We can therefore express the freshwater concentration evolution as

$$\frac{\partial}{\partial t}\left(\frac{\Delta S_{SZ}}{S_0}\right) = \frac{Q_T}{V_{SZ}} - \frac{\Delta S_{SZ}}{S_0}\frac{Q_A + Q_T + Q'}{V_{SZ}}. \tag{3.12}$$

If the volume fluxes Q_T and Q_A and the surf zone volume V_{SZ} vary much more slowly in time than $\Delta S_{SZ}/S_0$, then equation 3.12 can be solved for the freshwater fraction as a function of time,

$$\frac{\Delta S_{SZ}(t)}{S_0} = \frac{Q_T}{Q_T + Q_A + Q'} + \mathcal{C}e^{-t/\tau}, \tag{3.13}$$

where $\mathcal{C}$ is a constant of integration and the surf zone adjustment time, τ, is defined as

$$\tau = \frac{V_{SZ}}{Q_A + Q_T + Q'}. \tag{3.14}$$

We show in section 3.5.2 that Q' is small relative to Q_A and Q_T at the Quinault.

If $\tau < T_{var}$, the time scale of variability of the system, then equation 3.13 approaches a steady state where the surf zone freshwater fraction is proportional to the ratio of river volume flux to total surf zone alongshore volume flux. For the tidally modulated dynamics at the Quinault, the time scale of variability is associated with the $M2$ tide, $T_{var} \approx T_{M2}/2\pi \approx 2$ hrs. Estimates of τ and the steady state value of $\Delta S_{SZ}/S_0$ for a range of Q_A, Q_T, and V_{SZ} are shown in figure 3.10b-c.

If alongshore currents are negligible, then τ reduces to the surf zone fill time, $T_{SZ} = V_{SZ}/Q_T$. If $T_{SZ} < T_{var}$, then the surf zone will fill with fresh water ($\Delta S_{SZ}/S_0 = 1$) in the time T_{SZ}. Therefore, if $T_{SZ} < T_{var}$ and $\Delta S_{SZ}/S_0 < 1$, then freshwater is being exported from the surf zone.

3.4.2 Surf zone freshwater content

The evolution of the surf zone from fresh and minimally stratified to salty and highly stratified suggests a decrease in surf zone freshwater fraction. We estimate the surf zone freshwater fraction using the method outlined in appendix 3.7 (figure 3.6). In this section, we will show that there is a net export of freshwater from V_{SZ} and evaluate the role of wave-driven alongshore currents in removing this freshwater. At the Quinault, $S_0 = 27.5$ psu (appendix 3.7). The tidal volume flux Q_T and L_{SZ} both vary with the semidiurnal M2 tide [Kastner et al., 2019]. On April 30 2017, we consider an alongshore region on the south side of the river mouth, following the drifter trajectories. Note that Wong et al. [2013] show that in the presence of a wave-driven alongshore current, all the trapped river water is forced to one side of the river mouth. For a range of $100 < B_{SZ} < 500$ m, which characterizes the alongshore extent of the drifter trajectories in the surf zone, we see that T_{SZ} reaches a maximum of ~ 1.75 hrs for minimum river flow at high water (figure 3.11a). As $T_{SZ} < T_{M2}$ for the entire deployment but the surf zone freshwater fraction decreases, there must be transport of freshwater out of V_{SZ} and we can apply the framework developed in section 3.4.1.

Our observations of surf zone volume fluxes suggest that during our case study, Q_A and Q_T combine to set the alongshore volume flux in the surf zone (figure 3.11b). For the entire deployment on 30 April 2017, Q_B is much less than both Q_A and Q_T ($Q_B \sim 10$ m^3 s^{-1}), and is therefore neglected. As the offshore waves get larger and more obliquely incident during the deployment, Q_A increases, and as the tidal stage increases, Q_T decreases. We quantify uncertainty in Q_T by assuming a 20% error in the effective channel width, and in Q_A by assuming a 5° uncertainty in wave angle. As Q_A continues to grow over the course of the deployment with increasing wave height and angle (figure 3.5d), surf zone freshwater fraction decreases (figures 3.6 & 3.11d). In order to compare this change to the expected freshwater fraction of the surf zone from the CSR model, we note that the surf zone adjustment time τ is always shorter than our 30-minute averaging window and T_{M2} (figure 3.11a). We may therefore further simplify equation 3.13 to

$$\frac{\Delta S_{SZ}}{S_0} = \frac{Q_T}{Q_T + Q_A} \tag{3.15}$$

We can then compare a predicted freshwater fraction based on the volume fluxes Q_T and Q_A to a calculation of surf zone freshwater fraction (figure 3.11d).

Estimates of the surf zone freshwater fraction, with high uncertainty, show a similar decrease over the deployment. Note that V_{SZ} increases over the course of the deployment as wave height increases (figure 3.11c). The estimated freshwater fraction declines slightly before dropping off significantly (figures 3.6 & 3.11c). This decrease in freshwater fraction is consistent with freshwater being removed from the immediate region of the river mouth. The ratio of volume fluxes from equation 3.15 also decreases in time, but its specific behavior differs from the estimated freshwater fraction. These differences will be discussed in more detail in section 3.4.3.

As near-surface stratification increases when $\Delta S_{SZ}/S_0$ decreases, the remaining freshwater in the surf zone is in a near-surface layer. It follows that the DS/Dt and $\overline{S_t'^2}$ increase, as

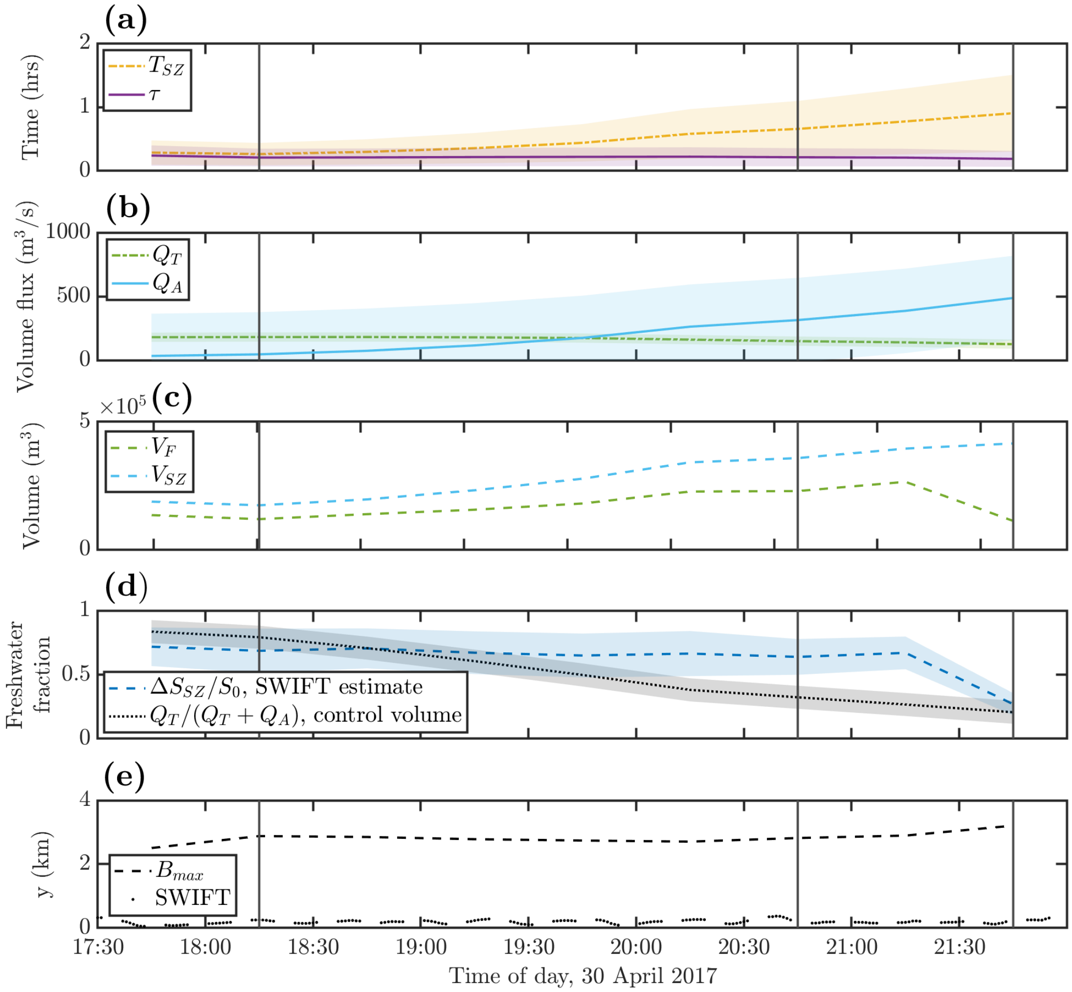

Figure 3.11: Time series of 30-minute average calculations related to the freshwater fraction of the surf zone. Panel (a) shows the time scales T_{SZ}, with an uncertainty interval generated by assuming a variety of values of B_{SZ}, and τ; panel (b) shows the volume fluxes due to the alongshore current and the tidal river flow; panel (c) shows estimates of the volume of freshwater in the surf zone and the total volume of the surf zone; panel (d) shows the estimated surf zone freshwater fraction (dashed blue line) and predicted surf zone freshwater fraction (dotted black line); panel (e) shows the alongshore position B_{max} (equation 3.16 and the alongshore location of the SWIFT drifter. The times of the cross sections in figure 3.6 are shown as vertical grey lines.

the region of high stratification at the base of the layer is exposed to higher wave-breaking turbulence.

3.4.3 The surf zone as a continuously stirred reactor: implications

Modeling the surf zone as a CSR synthesizes previous studies that have shown the surf zone to be retentive [Clark et al., 2010; Spydell and Feddersen, 2012; Hally-Rosendahl et al., 2014] and continuously forced by wave-breaking turbulence [Thornton and Guza, 1983; Feddersen, 2012a]. There are limitations to this comparison because of surf zone-specific dynamics, mainly that the surf zone is not perfectly retentive and that cross-shore exchange in the surf zone can be greatly increased by rip currents (see section3.5.2). Energetic, consistent wave-breaking turbulence and retentive behavior make the surf zone a relatively clear application of CSR theory by oceanographic standards, but the assumption that mixing is instantaneous and complete is an oversimplification; this a common problem in CSR applications [Metcalf et al., 1979; Tchobanoglous et al., 2014]. We will evaluate the discrepancies between the predicted surf zone freshwater fraction from CSR theory and estimated freshwater fraction in this context.

In a CSR, regions that are shielded from turbulence or gradients are known as "dead space" [Davis and Davis, 2003]. The presence of such regions reduces mixing, and so changes the composition of the fluid that exits the CSR [Menzinger et al., 1986]. The composition of the fluid in the dead spaces will be more similar than the well mixed fluid to the composition of one of the inflows. This is a possible explanation for the high freshwater fraction calculated using the SWIFT drifters. The drifters exit the river mouth and enter a surf zone eddy, remaing there for several hours, during which time the estimated freshwater fraction declines somewhat (figure 3.11d & figure 3.6a-b), but not as strongly as predicted by equation 3.15. The cross-shore extent of this eddy is approximately 1/4 of the surf zone width (figure 3.6a-b). When the drifters exit the eddy at the end of the deployment, they sample the surrounding surf zone, which is saltier and more highly stratified than the eddy, with a lower estimated freshwater fraction that is closer to the value predicted by equation 3.15. This is expected behavior from fluid that enters a dead space: river water stays closer to the river mouth salinity than the expected surf zone salinity while in the eddy. The implications of the CSR framework on the dynamics and mixing of small river plumes in the surf zone can thus be assessed and placed in context with previous studies.

The approximate surf zone freshwater fraction may be estimated using the framework from section 3.4.1 if V_{SZ}, Q_T, and Q_A are known. These may be estimated using a limited set of information: river discharge, incident wave height and angle, and beach slope. By calculating the surf zone adjustment time scale τ and $Q_T/(Q_T + Q_A)$, it may be possible to predict the freshwater fraction of the surf zone some distance away from the river mouth. If τ is less than T_{var} (T_{M2} for the Quinault), then the system is in steady state in a region within an alongshore distance of the river mouth given by

$$B_{max} = \frac{T_{var}\big(Q_A + Q_T\big)}{A_{SZ}}. \tag{3.16}$$

Therefore as Q_A increases relative to Q_T, V_{SZ} increases while the steady state freshwater fraction decreases. On an alongshore uniform beach, this results in a saltier, more diffuse plume when Q_A is high, and a fresher, more compact plume when Q_A is low but still significant. If Q_T increases relative to Q_A, then V_{SZ} increases and is fresher while it does so. In this case, baroclinic processes may drive dynamics near B_{max} if the plume propagates as a front through the surf zone, as shown in river plume studies [Garvine and Monk, 1974; Kilcher and Nash, 2010; Cole et al., 2020]. This framework may help determine if a plume is fresh and compact or salty and diffuse. At the Quinault, equation 3.16 yields $B_{max} \sim \mathcal{O}(10^3)$ m, increasing as $Q_A + Q_T$ increases and $\Delta S_{SZ}/S_0$ decreases (figure 3.11e). Our measurements are all well within B_{max} of the river mouth.

The theory developed and tested above and in sections 3.4.1 & 3.4.2 shows wave-driven alongshore currents are important for the dispersal of freshwater near the Quinault River mouth. Analogously, Wong et al. [2013] show that the presence of an alongshore current can act to trap river water if the alongshore current is strong enough to turn the river plume before it reaches the edge of the surf zone. This is expressed as the relationship between the surfzone width, L_{SZ}, and the jet-to-crossflow length scale associated with the river outflow and the alongshore current, $L_A = (U_T Q_T)^{1/2}/U_A$. When the ratio $L_{SZ}/L_A > 10$, Wong et al. [2013] show that surf zone entrainment is unity, meaning that all river discharge is trapped in the surf zone. If $L_{SZ}/L_A > 10$, then $Q_A > Q_T$, and so if the trapping condition found by Wong et al. [2013] is prevalent, $\Delta S_{SZ}/S_0 < 0.5$. In the limit where Q_T is very small compared to Q_A, the predicted surf zone freshwater fraction goes to zero and equation 3.14 simplifies to $\tau = B_{SZ}/u_a$, after which time the surf zone will be in steady state and salty at the alongshore distance B_{SZ}. The study of Wong et al. [2013] likely falls in this regime, as $Q_T \sim 0.2$ m^3 s^{-1}, and $Q_A \sim 3.75$ m^3 s^{-1}, so $\Delta S_{SZ}/S_0 \sim 0.05$, although this cannot be corroborated as the study does not include salinity measurements.

Results from Rodriguez et al. [2018] and Kastner et al. [2019] indicate that the freshwater flux into the surf zone may be less than the total volume flux out of the river mouth. These studies show that the volume of freshwater trapped in the surf zone, or the percent chance of a drifter being trapped in the surf zone, increases with decreasing river momentum flux relative to the wave momentum flux, but may not necessarily result in the total trapping of freshwater. Therefore, Q_T should be modified to reflect the flux of river water that is trapped in the surf zone. Additionally, with shore normal waves (and therefore $Q_A = 0$), Rodriguez et al. [2018] show that river water flows along the coast away from the river mouth on both sides of the mouth. In this situation, the volume flux of river water into the surf zone on one side of the river mouth, as defined in section 3.4.2, would be half of the total volume flux into the surf zone. In this scenario, Q_A is very small compared to Q_T, and so the predicted surf zone freshwater fraction becomes unity. The surf zone adjustment time (equation 3.14) becomes T_{SZ}, indicating that within B_{SZ} of the river mouth the surf zone will be fresh. Rodriguez et al. [2018] show the alongshore extent of freshwater in the surf zone after 1.7 days of continuous forcing in their figure 1c, finding $B \approx 3km$. Using equation 3.16 and values from Rodriguez et al. [2018] of $Q_T = 10$ m^{3}s^{-1} (half of river discharge), $L_{SZ} = 450$ m, $T_{var} = 1.7$ days, and beach slope $\tan\beta = 0.01$, we find that $B_{max} \approx 1.5$ km. Incorporating lateral exchange reduces the disparity between this predicted value of B_{max}

and the alongshore extent of low salinity found by Rodriguez et al. [2018] (section 3.5.2).

More comprehensive measurements are required to fully test the CSR model of the surf zone, but its application may be helpful in forecasting information desirable to the public, such as the residence time of salmon spawn near the Quinault River mouth and beach closures in Southern California.

3.5 Discussion

3.5.1 Vertical mixing of a river plume in the surf zone

We show in section 3.3.3 that K_z does not vary with respect to tidal stage on 30 April 2017, unlike Q_T, which decreases, and S, DS/Dt, $\overline{S_t'^2}$, and $\partial S/\partial z$, which increase. The lack of variability of K_z with respect to forcing parameters and parameters related to mixing is unlike previous plume studies. McCabe et al. [2008] show that the eddy diffusivity in the Columbia River plume drops from $K_z \sim \mathcal{O}(10^{-2})$ m^2 s^{-1} in the plume near field to $K_z \sim \mathcal{O}(10^{-4})$ m^2 s^{-1} farther away from the river mouth. This drop in eddy diffusivity is associated with a decrease in river momentum and salt flux as well as an increase in salinity from closer to farther away from the river mouth. It is notable, then, that we observe no trends in eddy diffusivity with Q_T, DS/Dt, and S.

While H_s increases modestly over the SWIFT deployment, there is no discernible increase in our estimates of ε. It may still be possible, therefore for K_z to depend on ϵ in the surf zone. ε is well predicted by models of surf zone turbulence, even in the presence of stratification. These models depend on the wave energy flux gradient, which in the surf zone is primarily determined by the offshore wave height. Therefore, because we cannot rule out a dependence of K_z on ε, and ε depends on H_s, we cannot rule out a dependence of K_z on H_s via the wave energy flux gradient (equation 3.8).

A significant simplifying assumption we make is taking K_z to be constant in the vertical. Our method of calculating K_z integrates over any vertical variability in the relationship between DS/Dt and $\partial S/\partial z$ (equation 3.4). Significant vertical variability on K_z has been observed in river plume systems [MacDonald and Geyer, 2004], and error in this assumption may explain some of the noise in our calculation of K_z using the best fit line shown in figure 3.8.

Our calculated values of K_z are of similar magnitude to river plume values (typically $\mathcal{O}(10^{-4})$ to $\mathcal{O}(10^{-2})$ m^{2}s^{-1}) [MacDonald and Geyer, 2004; McCabe et al., 2008], despite the high TKE dissipation rates we observe in the surf zone. This is likely due to the fact that unlike the stratified shear mixing common to river plumes, wave breaking turbulence is at a maximum at the water surface and is therefore not necessarily collocated with high salinity gradients [Feddersen, 2012b; Thomson et al., 2016]. Higher stratification near the surface (lower $\Delta S_{SZ}/S_0$)) therefore leads to larger DS/Dt, as shown in section 3.3.3. This is consistent with observations from the Fraser river plume [Kastner et al., 2018] and a one dimensional numerical model [Gerbi et al., 2015a], which both suggest that wave-driven turbulence has a greater impact on mixing when stratification near the surface is higher.

Assuming that salinity differences are the primary driver of density differences, then the buoyancy flux, $\mathcal{B}$, in the top 1.05 m of the water column can be expressed as

$$\mathcal{B} = \frac{g}{\rho_0}\beta \int \frac{DS}{Dt} dz, \tag{3.17}$$

where the reference density $\rho_0 = 1025$ kg m^{-3}, and $\beta = \partial\rho/\partial S = 0.77 \times 10^{-3}$ kg psu^{-1}, using the estimates of DS/Dt from the SWIFTv3. The average value of $\int \frac{DS}{Dt} dz$ is of order 10^{-2} psu m s^{-1}, leading to values of $\mathcal{B}$ that are 3-4 orders of magnitude smaller than the TKE dissipation rate, ε, in the same region (figures 3.7c and 3.8). This suggests that the surf-zone mixing efficiency, $\Gamma = \mathcal{B}/\varepsilon$, is several orders of magnitude lower than the commonly used value of $\Gamma = 0.2$ for stratified shear turbulence [Gregg, 2004]. Note, however, that the salt flux increases to 10^{-1} psu m s^{-1} as the surf zone becomes more stratified toward the end of the time series. This results in an increase in Γ, as ε remains the same, and suggests that the surf-zone mixing efficiency may be dependent on near surface stratification.

3.5.2 Lateral mixing and cross-shore exchange

The analysis presented in section 3.3.3 focuses on vertical mixing, assuming that lateral contributions to DS/Dt are small; however, lateral dispersion in the surf zone can be large [Clark et al., 2010; Spydell and Feddersen, 2012; Hally-Rosendahl et al., 2014]. The lateral salt flux can be parameterized as

$$\langle S'u' \rangle = K_x \frac{\partial S}{\partial x} \tag{3.18}$$

where $\langle S'u' \rangle$ is the flux of an entrained salinity S' by a velocity fluctuation u'. The horizontal eddy diffusivity, K_x, is taken as the range of values reported by Clark et al. [2010], $0.5 < K_x < 1.5$ m^2 s^{-1}, representing lateral exchange at the edge of the surf zone.

We take the cross-shore salinity gradient, $\partial S/\partial x$, to be the difference in salinity over a region of variability in the break point, the region of maximum cross-shore variability in salinity. We estimate the salinity difference for 30 April 2017 as the difference between the SWIFT measured salinity at 1.05 m depth and the mooring salinity at $\sim$ 1 m depth. This difference decreases from $\sim$ 22.5 psu to $\sim$ 8 psu over the drifter deployment (figure 3.12a). Using the method detailed in appendix 3.7, we observe the length scale of surf zone width variability, ΔL_{SZ}, to increase by a factor of $2.5 - 3$ over the course of the deployment period (figure 3.12a). We estimate $\partial S/\partial x$ as the mean value estimate at 1 m depth by the cross-shore fit in appendix 3.7 $\partial S/\partial x$ decreases over the length of the record by approximately one order of magnitude, with a similar decrease in lateral salt flux.

The estimated lateral salt flux is high, with values reaching $\mathcal{O}(10^{-1})$ psu m s^{-1} (figure 3.12b). This is similar to the maximum values of vertically integrated DS/Dt, which is equivalent to an average vertical salt flux in the top 1.05 m (figure 3.12b). These maxima do not occur at the same time—maximum lateral salt flux occurs when the surf zone is fresher at low water, while the maximum vertical salt fluxes occur at high water when $\partial S/\partial x$ has fallen by an order of magnitude. This suggests that lateral salt flux across the edge of the break point could be a source of high salinity water when the surf zone might be expected to be fresh. Additionally, as high salinity in the surf zone corresponds to a lower freshwater

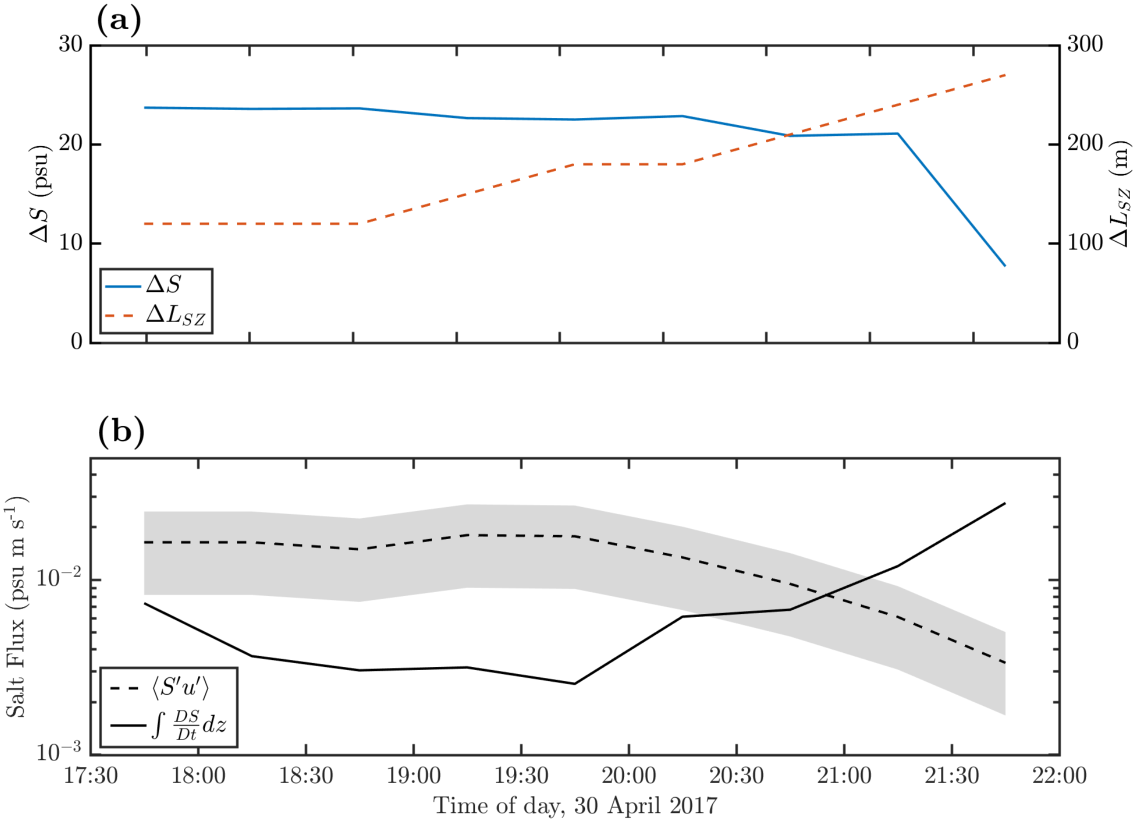

Figure 3.12: Time series of (a) the salinity difference between the surf zone and the shelf the surf zone width variability length scale and (b) the resultant lateral salt flux (dashed line) for $0.5 < K_x < 1.5$ m^2 (shading) s^{-1} and [Clark et al., 2010] and vertically integrated DS/Dt (solid line).

fraction and higher stratification but a lower cross-shore salinity gradient, vertical salt flux is large when lateral salt flux is expected at a minimum.

The lateral salt flux defined in equation 3.18 incorporates ambient water into the surf zone and surf zone water into the inner shelf. This exchange was taken to be negligible to obtain equations 3.14 & 3.15; we scale its contribution here. Equation 3.18 can be formulated as a volumetric salt flux by multiplying by the area of the break point such that $\langle S'Q' \rangle = \langle S'u' \rangle d_b B_{SZ}$. Taking $S'_{out} \sim \Delta S_{SZ} \sim \mathcal{O}(10^1)$ psu, the maximum value of $\langle S'u' \rangle \sim 0.01$ psu m s^{-1}, $d_b = 4$ m, and $B_{SZ} = 300$ m, $Q' \sim 1$ m^{3}s^{-1}. This is two orders of magnitude smaller than Q_A and Q_T. If the length scale $B_{max} \sim 3000$ m is used instead of B_{SZ}, $Q' \sim 10$ m^{3}s^{-1}. Lateral exchange may therefore contribute to the surf zone freshwater fraction of larger surf zone volumes, or if Q_A or Q_T is small. Incorporating Q' into the total surf zone transport helps refine the comparison of B_{max} to the alongshore extent of freshwater in the numerical model results of Rodriguez et al. [2018], assuming that the lateral exchange scales similarly at the Quinault and in the numerical model. Modifying the calculation from section 3.4.3 by taking the relevant volume flux for equation 3.16 to be $Q_T + Q' = 20$ m^{3}s^{-1}, where $Q' = 10$ m^{3}s^{-1} as calculated for a larger surf zone volume above, we find $B_{max} \sim 3$ km, similar to the maximum alongshore extent of freshwater found in Rodriguez et al. [2018].

Another exchange mechanism across the edge of the surf zone is the Stokes' drift-undertow overturning circulation, in which the depth-integrated Lagrangian transport due to Stokes' drift is balanced by a depth-uniform return flow (undertow) [Kumar et al., 2012; Lentz and Fewings, 2012]. The presence of freshwater in the surf zone will cause a baroclinic estuarine circulation [Geyer and MacCready, 2014]. These two overturning circulations act in opposite directions, as the net result of the Stokes' drift undertow circulation is onshore transport at the surface balanced by offshore transport at depth, and the estuarine circulation generates offshore velocity at the surface and onshore velocity at depth. The buoyant gravity current propagation speeds associated with the stratification at the Quinault moorings are not sufficiently large to overcome stokes drift [Kastner et al., 2019], but that does not preclude modification of the Stokes' drift-undertow circulation by the baroclinic pressure gradient associated with the estuarine circulation. Including the estuarine circulation in the nearshore mass balance would likely change the structure and magnitude of the residual transport, as shown in Rodriguez et al. [2018].

Rip currents have been show to significantly enhance cross-shore exchange between the surf zone and the inner shelf [Reniers et al., 2009; MacMahan et al., 2010; Clark et al., 2012; Hally-Rosendahl et al., 2014; Kumar and Feddersen, 2017a; Moulton et al., 2017], and are therefore likely to play a role in the removal of river water from the surf zone. The lateral spacing of bathymetrically driven rip currents may act as a control on B_{SZ} [MacMahan et al., 2006; Castelle et al., 2014], as the CSR framework as developed in section 3.4.1 does not include a rip current freshwater or volume flux. We did not observe the presence of rip currents at the Quinault River mouth in either the drifter trajectories or in the nearly continuous video recordings using an aerial drone, and so we are unable to estimate their significance in our dataset.

3.5.3 Surf zone freshwater content during the Quinault observational program

We can apply the model developped in section 3.4.1 to the ~ 9 days when the offshore wave measurement was deployed at the Quinault River mouth. We calculate Q_A as described above, and take Q_T to be the fraction of river water trapped in the surf zone, found using the conceptual model from Kastner et al. [2019] (figure 3.13a). The resulting adjustment time τ is always less than $T_{var} \approx 2$ hrs for a range of B_{SZ}, as in section 3.4.1 (figure 3.13b). We can therefore use the scaling from equation 3.15, assuming that the break point fluxes Q_B and Q' are small, as they are in the case study.

The resulting calculation shows semidiurnal tidal variability associated with variation in Q_T and longer period (2-3 day) variability associated with variability in the wave condition, and therefore Q_A (figure 3.13c). The wave-driven variability appears to be larger in magnitude than the tidal variability, but is less consistent. Decreases in freshwater content at high water when Q_T is low, as observed in the case study, may therefore be common, if not always large in magnitude. Note that when $Q_A \sim 0$, the freshwater fraction goes to unity.

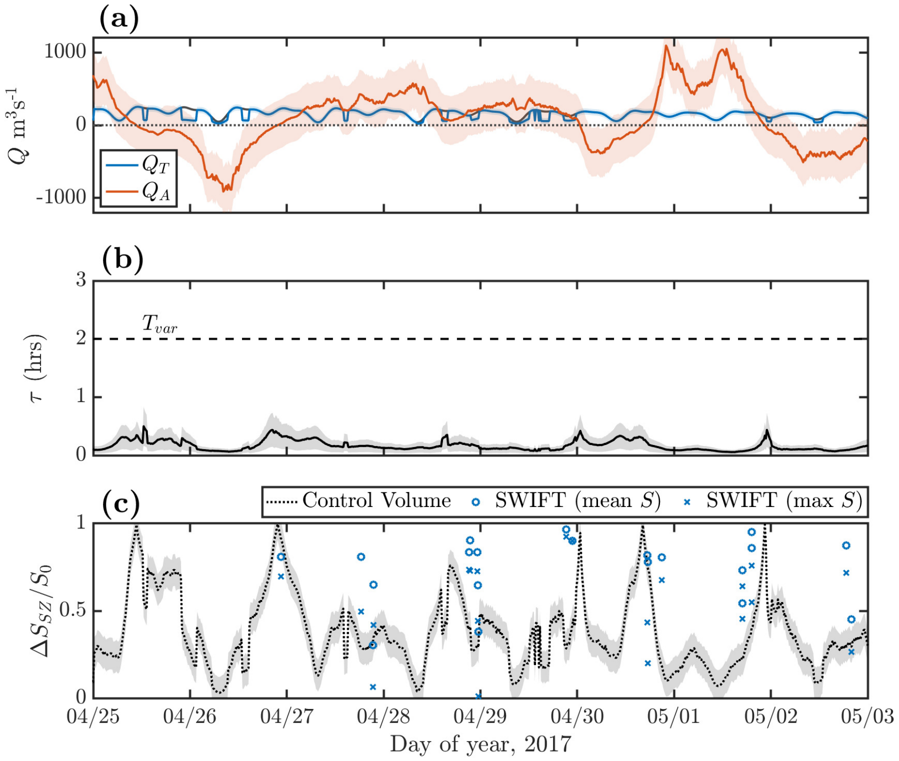

Figure 3.13: Estimates of surf zone freshwater content during the Quinault observational period. Panel (a) shows the trapped river volume flux in blue, with the grey line indicating the total when not all river water is trapped in the surf zone per the conceptual model of Kastner et al. [2019]; alongshore current volume flux is shown in red. The mean uncertainty over the record is shown by the shaded regions around each line. Panel (b) shows the surf zone adjustment time scale τ, with a range of values generated by letting B_{SZ} vary from 100 to 500 m. Panel (c) shows the surf zone freshwater fraction, with the control volume scaling shown as the dotted black line, and estimates of the freshwater fraction from the mean and maximum SWIFT salinity measurements in the surf zone shown as the circles and crosses, respectively. The shaded region indicates the maximum uncertainty generated by the propagation of error from Q_A and Q_T.

As Q_A grows in magnitude after such a period, the salinity anomaly associated with Q_A, ΔS_A may be nonzero, changing the form of equation 3.12. SWIFT estimates of freshwater fraction are mostly higher than the control volume calculation, especially when the mean SWIFT-measured surf zone salinity is used to calculate $\Delta S_{SZ}/S_0$, as opposed to the maximum SWIFT-measured surf zone salinity. As the SWIFTs start in fresh water in the river mouth, the SWIFT salinity measurements may therefore be biased fresh relative to the average surf zone salinity. Both the SWIFT estimates and the control volume calculation span the possible range of $\Delta S_{SZ}/S_0$, however, indicating that the surf zone freshwater fraction near the Quinault River mouth is highly variable on short time scales.

Expanding this calculation to the full year of 2017 indicates that seasonal variability is driven by variability in the river discharge, while monthly and shorter variability is driven by variability in the wave conditions. The adjustment time τ is always less than T_{var} during 2017 (not shown). The surf zone is generally fresher in the winter and fall than in the summer (figure 3.14). In general, Q_A varies more than Q_T, and so the freshwater content is driven more by the wave condition than the river discharge. Variability in Q_T due to the spring-neap tidal cycle may also play a role in setting $\Delta S_{SZ}/S_0$, but is not as pronounced. Note that this calculation assumes all river water is trapped in the surf zone. In chapter 2, 70% of river discharge is shown to be trapped in the surf zone, with more than 50% of the river discharge escaping during the summer, when the wave condition is low, and winter storms, when the discharge is high, as indicated by the shaded grey area on figure 3.14.

3.6 Summary

We present results from an observational study of river water that has been trapped in the surf zone near the Quinault River mouth. We find that the material derivative of salinity, DS/Dt, increases as stratification, $\partial S/\partial z$, and surf zone freshwater fraction, $\Delta S_{SZ}/S_0$, decrease. The relationship between stratification and DS/Dt yields estimates of vertical eddy diffusivity $K_z \approx 1 \times 10^{-2}$ m^2 s^{-1}. Estimates of lateral salt flux across the edge of the surf zone suggest that lateral processes may be important for the introduction of salty water to the surf zone,

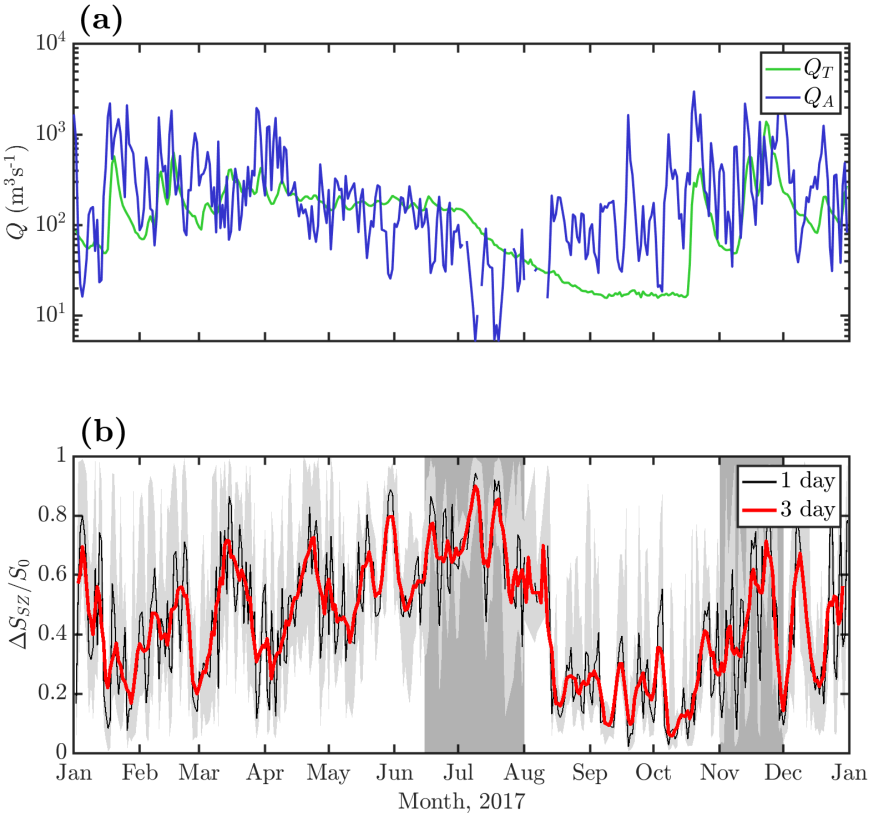

Figure 3.14: Estimates of Q_A (a), Q_T (a), and $\Delta S_{SZ}/S_0$ (b) for the year of 2017 from USGS and CDIP discharge, tide, and wave data. Panel (b) shows a daily average of freshwater fraction as well as a three day rolling average. The shaded error bar indicates the minimum and maximum freshwater content observed on a given day. The dark grey shaded areas on panel (b) indicate times of the year when the conceptual model (chapter 2) predicts that more than half the river water will escape the surf zone.

particularly when the surf zone is fresh and stratification is low (high freshwater fraction). Using framework similar to a continuously stirred reactor, we show the surf zone freshwater fraction to be related to the wave-driven alongshore transport, Q_A, and the flux of river water into the surf zone, Q_T. As Q_A increases relative to Q_T, the surf zone freshwater fraction decreases, and DS/Dt increases. Conversely, when Q_T increases relative to Q_A, the surf zone freshwater fraction increases, and DS/Dt decreases. The vertical structure of surf zone turbulence is not altered by stratification. Therefore, this behavior indicates that the presence of high near-surface vertical salinity gradients will lead to more mixing when $\Delta S_{SZ}/S_0$ is small than when $\Delta S_{SZ}/S_0$ is large.

3.7 Appendix: surf zone freshwater fraction calculations

In order to assess the surf zone freshwater fraction, we make use of mooring salinity observations near the surf zone edge and SWIFTv3 salinity observations in the surf zone. We reconstruct the vertical salinity profile from the moorings using a linear fit to the two CTD measurements, and a quadratic fit to the three SWIFT CT measurements. A quadratic profile is used in the surf zone to capture the high near surface stratification observed by the drifters (up to$\mathcal{O}(10)$ psu/m) without causing spuriously high salinity ($S > 27.5$ psu) at depth. We constrain these vertical fits such that the salinity can never exceed 30 psu and the minimum salinity is always at the water surface. Assuming alongshore uniformity, we then leverage the increasing cross-shore position of the moorings from north to south to fit a cross-shore (x) profile of the form

$$S(x,z) = \frac{S_{max}(z) + S_{min}(z)}{2} + \frac{S_{max}(z) - S_{min}(z)}{2} \tanh\left(\frac{x + L_{SZ}}{\Delta L_{SZ}}\right), \tag{3.19}$$

at each depth z, where S_{max} is the maximum salinity at a given depth, constrained by the mooring salinity linear fit, S_min is the minimum salinity constrained by the SWIFT salinity quadratic fit, L_{SZ} is the surf zone width calculated using the significant wave height [Kastner et al., 2019], and ΔL_{SZ} is the surf zone width variability. We assume that the surf zone salinity would vary with ΔL_{SZ} in the cross-shore near the break point. To estimate

ΔL_{SZ}, we assume a Rayleigh distribution of wave heights, and find the location at which waves of height $H_{RMS} = H_s/\sqrt{2}$ and $H_{1/10} = 1.27H_s$ will break [Dean and Dalrymple, 1984]. The difference between these cross-shore positions is ΔL_{SZ}.

Thie fit in equation 3.19 is calculated using the 30 minute average cross-shore position of the SWIFTv3 and the static cross-shore position of the moorings. We force stable stratification. We take the reference salinity to be the mean value measured at the bottom CTD of the North mooring during the SWIFT deployment, $S_0 \approx 27.5$ psu. The surf zone volume, V_{SZ} can be estimated using cross-shore bathymetry profiles compiled from the SWIFTv4 depth finder, and the offshore wave condition from the AWAC, shoaled using linear wave theory until a critical value of $H_s/d = \gamma = 0.6$ is reached. The surf zone freshwater volume per unit alongshore distance, V_F/B_{SZ}, can then be calculated as the integral of equation 3.19 in depth and cross-shore position, from the shoreline to the surf zone edge. The minimum freshwater fraction at a given time is found by taking the whole surf zone to be of uniform salinity equal to the average drifter measured salinity during each 30 minute period. The uncertainty interval found by the difference between this minimum freshwater fraction and the estimate found by integrating equation 3.19 is then assumed to be symmetrical.

Chapter 4

IMPLICATIONS

4.1 The fate of surf-zone trapped river water

The probability that a parcel of water exiting the Quinault River mouth escapes the surf zone is set by the cross-shore balance of river and wave forcing. Chapter 2 shows that balance is described by the ratio of length scales L_{NF}/L_{SZ}, the plume near field length over the surf zone width. This is similar to the scaling developed by Rodriguez et al. [2018] relating the river momentum flux and the wave radiation stress, $\rho u^2 h/S_{xx}$. When a strong wave-driven alongshore current is present, surf zone plume entrainment increases as the jet-to-crossflow length scale L_A decreases relative to L_{SZ}, with total entrainment at $L_{SZ}/L_A \approx 10$ [Wong et al., 2013], although this behavior is not observed at the Quinault [Kastner et al., 2019]. All of these metrics show that as river forcing increases relative to wave forcing (be it cross-shore or alongshore), more river water escapes the surf zone onto the inner shelf; conversely, as wave forcing increases relative to river forcing, more fresh, river water is trapped in the surf zone. The volume flux of river water into the surf zone is therefore the percentage of the volume flux out of the river mouth that is trapped in the surf zone.

Trapped river water has lost its cross-shore momentum in its fight to escape the surf zone, and is therefore primarily forced by surf zone processes in addition to its own volume flux. As detailed in chapter 3, the trapped river volume flux, Q_T, and the wave-driven alongshore current, Q_A, set the surf zone freshwater fraction, $\Delta S_{SZ}/S_0$, after a time τ determined by these fluxes and the volume of the surf zone. A freshwater fraction results in smaller gradients in surf zone salinity, and in turn lor DS/Dt. The relevance of the alongshore current in determining the surf zone freshwater fraction suggests that surf zone trapped freshwater may be influenced by surf zone dynamics such as eddies, instabilities, rip currents, and break point modulation by wave groups or the tide. Although the surf zone is generally retentive, these processes can cause exchange with the inner shelf [Clark et al., 2010; Spydell and Feddersen, 2012; Hally-Rosendahl et al., 2014].

4.1.1 The impact of surf zone processes on freshwater transport and mixing

Lateral eddies in the surf zone could retain or mix river water that enters them, depending on their stability. A stable circulation could act to cut off fresh river water from the surf zone around it as the surf zone freshwater fraction falls (see chapter 3), while an unstable eddy could cause lateral mixing [Spydell et al., 2007; Clark et al., 2010]. Chapter 3 section 3.5.2 suggests that lateral mixing could be a significant process when the surf zone freshwater fraction is high. This is likely especially relevant in the case of shear instabilities on an alongshore current, which form between the low-momentum water of the inner shelf and relatively high momentum water of the surf zone, generating significant exchange [Feddersen, 2014; Hally-Rosendahl et al., 2014]. The presence of such a shear instability along the surf zone edge when the surf zone is fresh and the inner shelf is not would transport freshwater offshore to the inner shelf and salty water onshore to the surf zone as well as laterally mixing a strong gradient.

Similarly, the presence of transient or bathymetrically controlled rip currents would cause exchange and mixing between a fresh surf zone and salty inner shelf. Transient rip currents, formed as vortex dipoles generated by short-crested wave breaking, might act to periodically flush some fresh surf zone water onto the inner shelf. This process may be especially important with a shore normal but directionally spread offshore wave condition, which would generate minimal alongshore currents but a large amount of transient rip activity [Clark et al., 2012; Hally-Rosendahl et al., 2014; Kumar and Feddersen, 2017a,b]. Bathymetrically dominated rip currents may serve as a barrier to the propagation of freshwater in the surf zone, as they occur in predictable locations [Reniers et al., 2009; MacMahan et al., 2010; Moulton et al., 2017]. The large, persistent, offshore velocities associated with bathymetric rip currents ($\mathcal{O}(1)$ m/s) are of similar magnitude to alongshore current and river mouth velocities, and could act as a release valve for surf zone trapped freshwater. In this scenario, a bathymetric rip current at some alongshore distance from the river mouth, B_{rip}, would act to prevent, or at least minimize, the expansion of freshwater in the surf zone beyond that distance. Observations from the Quinault do not show the presence of rip currents, but aerial imagery near the mouth of the Rio Maipo, near San Antonio, Chile, shows the presence of rip currents amidst the surf zone trapped plume water (figure 4.1).

Modulation of the break point when freshwater is trapped in the surf zone may allow the freshwater to escape when the break point moves onshore, as the freshwater at the surf zone's edge is then no longer subjected to the processes that pen it into the surf zone [Munk, 1949]. Such break point variability can occur on wave group and tidal time scales. Wave groups typically have a frequency on the order of minutes, with the waves at the group's maximum breaking further offshore than those at the minimum. This causes rapid movement of the break point, potentially allowing freshwater to escape while eroding the salinity gradient at the edge of the surf zone as the salinity gradient is exposed to wave breaking turbulence and lateral eddies. This is likely a transient process—the wave group induced break point motion is periodic, and absent strong inner shelf circulation will pass over the same water repeatedly.

The break point can also move on tidal time scales. For a constant wave condition, the breaker depth is constant. Over non-linear bathymetry, the cross-shore location of this depth will change as the tidal stage change. The surf zone volume therefore contracts and expands with the tide. Over an equilibrium beach profile where the depth is given by $d = Ax^{2/3}$ (where A is a constant) and the beach is alongshore uniform, the surf zone is smaller at high water than at low water [Dean and Dalrymple, 1984]. When the surf zone adjustment time is greater than the time scale of variability of the system, $\tau > T_{var}$, then the surf zone will not approach a steady state value of the freshwater fraction before the system has significantly changed. In this case, the tidal contraction and expansion of the surf zone near the river mouth may be important mechanisms for the export of freshwater or entrainment of saltwater, respectively. Far from the river mouth ($y > B_{max}$), this mechanism may also be important for removing remnant plume freshwater from the surf zone.

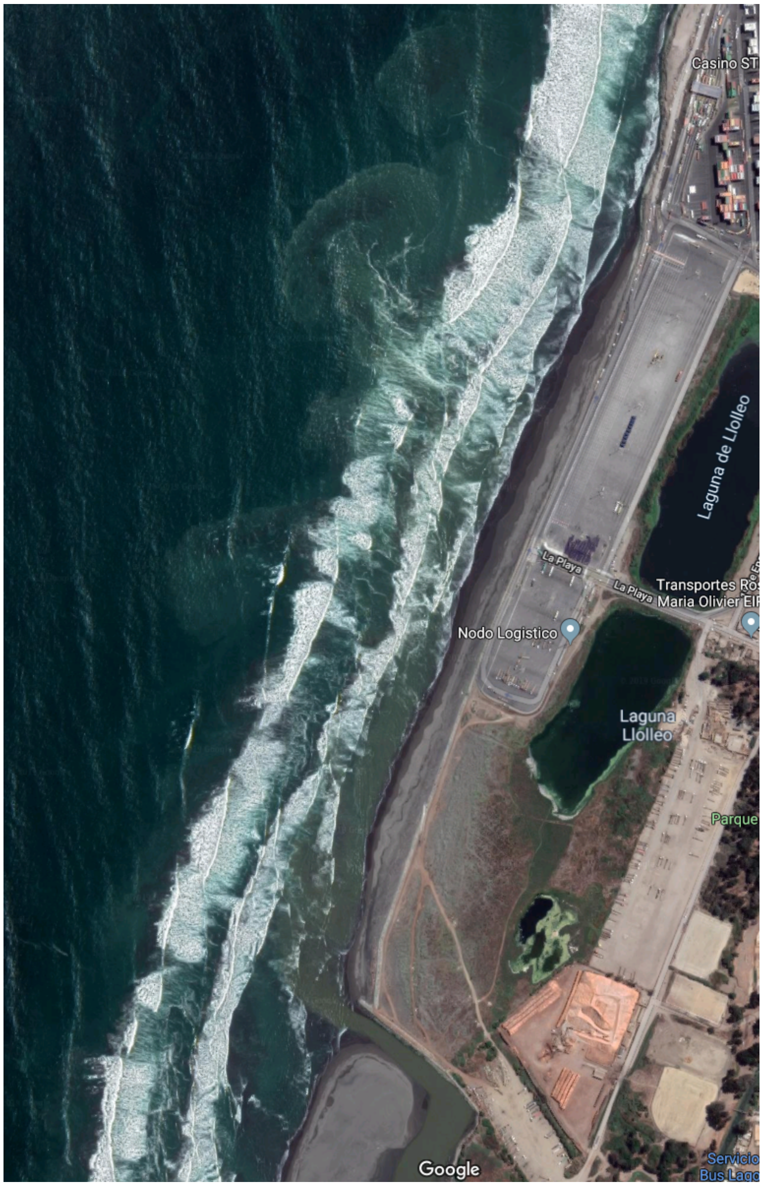

Figure 4.1: Google Earth aerial imagery of the mouth of Rio Maipo, near San Antonio, Chile. North is up. The river mouth is located in the South portion of the image, where brown river water enters the surf zone. The incoming wave condition is oblique to the coast in a manner that would be expected to force a northward alongshore current. Rip current activity is visible as several mushroom-shaped plumes of light colored water leaving the surf zone downstream from the river mouth in the direction of alongshore current propagation.

4.1.2 Comparison to conventional river plume dynamics

The surf zone-trapped plume, propagating along the coast while limited in cross-shore extent, bears a striking resemblance to the mid- and far-field river plume. If $\tau < T_{var}$, as at the Quinault, then by the theory laid out in chapter 3, a front will form at a distance alongshore $y = B_{max}$. The front at B_{max} will therefore have a baroclinic frontal propagation speed associated with the density difference between the water closer to the river mouth, in the newly trapped plume, and the water further from the river mouth. If the velocity associated with total alongshore volume flux, $(Q_A+Q_T)/A_{SZ}$ drops below the frontal propagation speed, then it is possible that the front will continue propagating as a gravity current [Garvine and Monk, 1974; Garvine, 1984; Nash and Moum, 2005b; Kilcher and Nash, 2010; Cole et al., 2020]. Changes to the volume fluxes Q_T and Q_A will change both the location of B_{max} and the surf zone freshwater fraction. At the plume front, baroclinic processes may be important, resulting in increased stratification due to baroclinic slumping [Farmer et al., 2002]. This may in turn cause an increase in mixing as high salinity gradients are exposed to more energetic wave breaking turbulence closer to the surface (see section 4.2).

The cross-shore dynamics of a surf zone trapped plume are similar to those of a far-field plume in that both are constrained by the coastline and an external forcing mechanism: waves for the surf zone trapped plume, wind for the far field plume [Fong and Geyer, 2001; Lentz, 2004; Lentz and Largier, 2006]. In the surf zone trapped plume, salinity gradients can occur in both the cross-shore and vertical directions (chapter 3). These will both cause a baroclinic pressure gradient that tends to push fresher water offshore and saltier water onshore. Such an estuarine circulation would cause the near-surface, where wave breaking turbulence is high, to become more stratified, potentially increasing mixing. This circulation is opposed, however, by the cross-shore radiation stress gradient, $\partial S_{xx}/\partial x$. Understanding this interaction will allow for better predictions of near-surface mixing in the surf zone.

4.2 *Wave-driven river plume mixing*

4.2.1 Previous work

Mixing requires turbulence and a gradient. In the case of stratified shear turbulence, which has been shown to be a dominant source of river plume mixing, shear-driven turbulence is colocated with high stratification. In most cases this will not be true for wave-driven mixing, as wave-breaking turbulence is highest at the water surface, and is unrelated to the stratification of the plume layer [Terray et al., 1996; Thomson et al., 2016; Zippel and Thomson, 2017]. The penetration length scale for the wave-driven turbulence has been shown to be related to the wave height, H_S. Defining the river plume depth h_p to be the location of maximum stratification, then one might expect wave-driven river plume mixing to scale with the ratio H_S/h_p.

Previous studies of wave-driven plume mixing have focused on steepness limited wave breaking, either due to an excess input of energy from the wind [Gerbi et al., 2013b, 2015b] or wave-current interaction [Thomson et al., 2014; Kastner et al., 2018]. A common theme among these studies is that wave-driven mixing is strongest near the water surface and weaker as depth increases [Gerbi et al., 2015b; Kastner et al., 2018]. Specifically, Gerbi et al. [2015b] show with a numerical model that the near-surface TKE balance with a surface mixed layer is between dissipation, buoyancy flux, and the wave-driven downward flux of TKE, with shear production becoming more important near the base of the surface mixed layer. The surface mixed layer also thickens faster initially in simulations that include wave breaking turbulence, as the strong gradients at its base are accessible to wave-driven turbulence.

When h_p is large relative to H_S, wave-driven mixing is lessened. The numerical simulations of Gerbi et al. [2015b] show this, as simulations with and without wave-driven turbulence approach similar mixed layer thickening rates as the mixed layer becomes deeper, and the interface is shielded from wave-driven mixing. Observations from the Fraser River plume also show that wave-driven turbulence is small at the base of the plume when $h_p \sim 3$ m and $H_S/h_p < 1$ [Kastner et al., 2018].

When waves break due to steepening from encountering an opposing current at a river plume front, downwelling currents present at the plume front may advect the wave-driven turbulence beyond its typical penetration length scale H_S (implied by Thomson et al. [2014]). This may allow wave-driven mixing to be important at greater depths than in the absence of such currents, as wave-driven turbulence can persist for several wave periods [Sullivan et al., 2004; Thomson et al., 2016], and downwelling velocities in the river plume front can be $w \sim 0.2$ m/s [O'Donnell et al., 1998], so for such a downwelling velocity, $H_S = 2$ m, and a wave period $T = 7$ s, the penetration length scale $H_S + nwT = 6.2$ m, assuming the wave-driven turbulence persists for $n = 3$ wave periods.

4.2.2 Analytical framework

The length scales H_S and h_p are the characteristic vertical length scales of wave-driven turbulent dissipation rate (ε) and stratification ($\partial S/\partial z$), respectively. The relationship between ε and $\partial S/\partial z$ characterizes wave-driven mixing: both must be significant for turbulence to cause mixing. An understanding of the vertical structure of wave-driven mixing can therefore be gained by using classic parameterizations of wave-driven TKE dissipation rate and stratification.

The specific parameterizations to use for ε and $\partial S/\partial z$ depend on the system of interest; the choices presented here are relevant in the surf zone but can be generalized, as discussed below. The vertical structure of wave-driven turbulence is well described by equation 3.6 [Terray et al., 1996; Feddersen, 2012a]. The model of ε dervied by Feddersen [2012b] is explicitly suited for the surf zone, but Zippel and Thomson [2015] and chapter 3 show that both models perform adequately, and equation 3.6 is more easily applied to steepness limited breaking, as is present due to wave current interaction at the front of the Columbia River plume [Thomson et al., 2014] or whitecapping in the far-field Hudson River plume [Gerbi et al., 2013b]. Assuming that the salinity profile is well described by a hyperbolic tangent function,

$$S(z) = \frac{S_{max} + S_{min}}{2} - \frac{S_{max} - S_{min}}{2} \tanh\left(\frac{z - h_p}{\Delta h}\right), \tag{4.1}$$

where S_{max} and S_{min} are the maximum and minimum salinity in the water column and Δh is the characteristic length scale of vertical variability at the base of the plume layer, which reaches maximum stratification at $z = h_p$. In order to generate the vertical profiles of salinity, stratification, and dissipation in figure 4.2, values characteristic of the Quinault system are used to evaluate equations 3.6 & 4.1 (table 4.1).

Model	Quantity	Description	Value
Terray et al. [1996] ε scaling (eq. 3.6)	H_S	Significant wave height	1.5 m
	$\partial F/\partial x$	Wave energy flux gradient	36 W/m^2
	A_T	Fitting constant)	5×10^{-5}
	λ	Fitting constant)	-1.2
Salinity tanh profile (eq. 4.1)	S_{max}	Maximum salinity	27.5 psu
	S_{min}	Minimum salinity	15 psu
	h_p	Plume depth	1 m
	Δh	Vertical variability length scale	0.5 m

Table 4.1: Quantities used to evaluate the models for ε and S in equations 3.6 & 4.1, respectively, for figure 4.2. These values are characteristic of the surf zone near the Quinault River mouth (chapters 2 & 3)

.

Figure 4.2 shows that wave-driven turbulence decays by roughly an order of magnitude from its near-surface maximum to its characteristic depth at $z = -H_S$, while a region of elevated stratification exists in the range of $0.5 < z < 1.5$ m, dictated by the values of Δh and h_p. It would therefore be expected that the most mixing would occur in that depth range, with a maximum between $0.5 < z < 1$ m. In this upper portion of the region of high stratification, wave-driven dissipation is higher.

In the TKE budget, mixing is expressed as a buoyancy flux. Assuming shear production is small (i.e. wave breaking is the only source of turbulence), and the turbulence is relatively steady [Gerbi et al., 2009; Scully et al., 2011], the budget reduces to

$$0 = \mathcal{B} - \mathcal{T} + \varepsilon, \tag{4.2}$$

where $\mathcal{B}$ is the buoyancy flux and $\mathcal{T}$ is the transport of TKE due to wave breaking. The buoyancy flux can be expressed as

$$\mathcal{B} = \frac{g}{\rho_0}\beta\langle S'w'\rangle, \tag{4.3}$$

where $\beta = \frac{\partial \rho}{\partial S} = 0.77 \times 10^{-3}$ kg m^{-3} psu^{-1}. Similar to the definition of the mixing efficiency, Γ, in stratified shear turbulence, the wave-driven mixing efficiency, Γ_W, can be defined as

$$\Gamma_W = 1 - \frac{\mathcal{T}}{\varepsilon} = \frac{B}{\varepsilon}. \tag{4.4}$$

By collapsing the TKE transport into Γ_W, it is possible to directly relate dissipation to buoyancy flux,

$$\varepsilon = \frac{K_z}{\Gamma_W}\frac{g}{\rho_0}\beta\frac{\partial S}{\partial z}. \tag{4.5}$$

Here, the salt flux has been expressed as the product of the vertical eddy diffusivity, K_z, and stratification.

The structure of surf zone TKE dissipation rate is not significantly modified by stratification (chapter 3), so the only quantities in equation 4.5 that are not easily measured or parameterized are K_z and Γ_W. A constant value of $K_z \approx 10^{-2}$ m^2/s is determined in chapter 3. This value of K_z is not dependent on wave energy or surface velocity; however, the method used to calculate K_z integrates over any vertical variability. Using a constant value of K_z to determine a value of Γ_W using the estimates of ε and $\partial S/\partial z$ presented in chapter 3 is therefore a dubious proposition. The order of magnitude of Γ_W can be approximated using characteristic values from the Quinault surf zone in the near-surface, where $\varepsilon \sim \mathcal{O}(10^{-2})$

W/kg, $K_z \sim \mathcal{O}(10^{-2})$ m^2/s, and $\partial S/\partial z \sim \mathcal{O}(10^0)$ psu/m. These values yield $\Gamma_W \sim \mathcal{O}(10^{-4})$. This suggests that for average conditions at the Quinault, Γ_W is much smaller in magnitude than the quasi-canonical $\Gamma = 0.2$ for stratified shear turbulence. However, this scaling mainly serves as a note of caution, as the specific value of Γ_W will significantly depend on K_z, including any unresolved vertical structure.

In order to fully constrain Γ_W, the vertical structure of K_z must be determined by relating stratification to direct estimates of salt flux. This could be accomplished by mounting fast-sampling CTDs and Acoustic Doppler Velocimeters (ADVs) to a frame in the surf zone near the Quinault River mouth (or a similar system). The frame would span the entire water column, would have pairs of instruments consisting of one CTD and one ADV, mounted as closely together as possible and at exactly the same vertical position. The pairs of instruments would be mounted as closely together in the vertical as possible in order to maximize the amount of the water column that could be measured (this would obviously be very expensive). Such a field setup could be used to calculate the vertical salt flux as the covariance of S and w after significant quality control and removing the influence of wave orbital motions [Bryan et al., 2003; Thomson et al., 2007; Feddersen, 2010; Derakhti et al., 2020]. Equation 3.2 could then be evaluated to obtain the vertical structure of K_z, and in turn Γ_w.

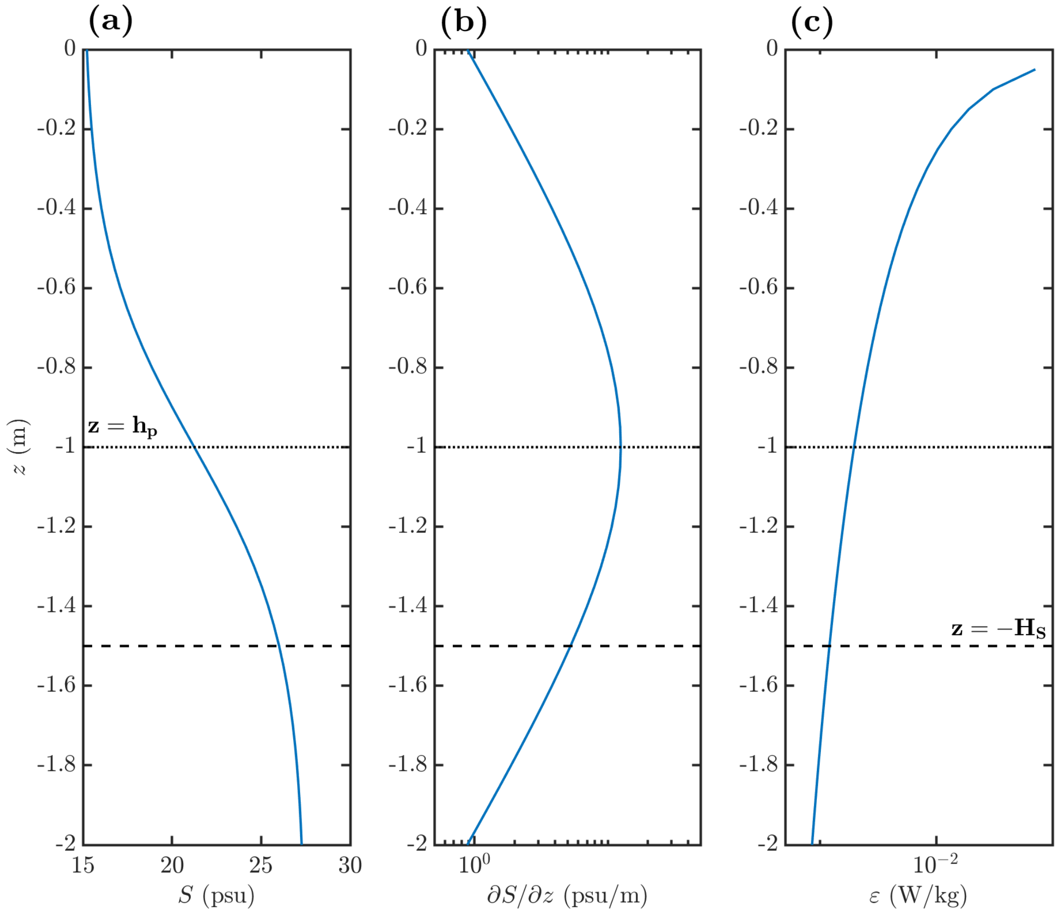

Figure 4.2: Synthetic profiles of (a) salinity, (b) stratification, and (c) TKE dissipation rate using characteristic values from the surf zone near the Quinault River mouth (chapters 2 & 3, table 4.1) to evaluate the models for ε and S in equations 3.6 & 4.1, respctively. The vertical position of the characterstic length h_p and H_S are given by the black dotted and dashed lines, respectively.

Chapter 5

SUMMARY

Chapter 2: A conceptual model based on the interaction of river and wave forcing over complex bathymetry describes the behavior of the Quinault River plume.

- When wave forcing dominates over river forcing, freshwater is trapped in the surf zone.
- Tidal variability allows river water to escape due to river momentum and bathymetric effects.
- The maximum excursion of trapped river water is set by the plume near field length.

Chapter 3: Mixing in the surf zone is higher when the surf zone freshwater content is lower.

- Mixing of river water that is trapped in the surf zone scales with near surface stratification and is well described by a constant eddy diffusivity.
- The surf zone near a river mouth can be stratified; this stratification does not change the vertical structure of wave breaking turbulence.
- The freshwater content of the surf zone can be modeled as a continuously stirred reactor, with a flux of salty water from a wave-driven alongshore current and a flux of freshwater from the river discharge, mixed by wave breaking turbulence.

Chapter 4: The fate of trapped river water is tied to surf zone dynamics and mixing.

- Wave driven mixing is expected to be largest when high stratification is closest to the source of wave breaking turbulence at the surface; this is similar to findings from previous studies.

BIBLIOGRAPHY

Ç. Akan, S. Moghimi, H. T. Özkan-Haller, J. Osborne, and A. Kurapov. On the dynamics of the mouth of columbia river: Results from a three-dimensional fully coupled wave-current interaction model. *Journal of Geophysical Research: Oceans*, pages n/a–n/a, 2017a. ISSN 2169-9291. doi: 10.1002/2016JC012307. URL `http://dx.doi.org/10.1002/2016JC012307`.

C. Akan, S. Moghimi, O.-H. H. T., O. J., and K. A. On the dynamics of the mouth of columbia river: Results from a three-dimensional fully coupled wave-current interaction model. *Journal of Geophysical Research: Oceans*, 122(8):2373–2388, 2017b.

J. A. Battjes and J. P. F. M. Janssen. *Energy Loss and Set-Up Due to Breaking of Random Waves*, pages 569–587. American Society of Civil Engineering, 1978. doi: 10.1061/9780872621909.034. URL `https://ascelibrary.org/doi/abs/10.1061/9780872621909.034`.

N. Booij, R. Ris, and L. Holthuijsen. A third-generation wave model for coastal regions. I- Model description and validation. *Journal of Geophysical research*, 104(C4):7649–7666, 1999.

A. J. Bowen and R. A. Holman. Shear instabilities of the mean longshore current: 1. theory. *Journal of Geophysical Research: Oceans*, 94(C12):18023–18030, 1989. doi: 10.1029/JC094iC12p18023. URL `https://agupubs.onlinelibrary.wiley.com/doi/abs/10.1029/JC094iC12p18023`.

J. A. Brown, J. H. MacMahan, A. J. H. M. Reniers, and E. B. Thornton. Field observations of surf zone–inner shelf exchange on a rip-channeled beach. *Journal of Physical Oceanography*, 45(9):2339–2355, 2015. doi: 10.1175/JPO-D-14-0118.1. URL `https://doi.org/10.1175/JPO-D-14-0118.1`.

A. Bruscas. Forecast prompts Quinaults to halt 2019 commercial blueback fishery. *The North Coast News*, 2019. URL `https://www.northcoastnews.com/news/forecast-prompts-quinaults-to-halt-2019-commercial-blueback-fishery/`.

K. R. Bryan, K. P. Black, and R. M. Gorman. Spectral estimates of dissipation rate within and near the surf zone. *J. Phys. Oceanogr.*, 33:979–993, 2003.

B. Castelle, A. Reniers, and J. MacMahan. Bathymetric control of surf zone retention on a rip-channelled beach. *Ocean Dynamics*, 64(8):1221–1231, 2014.

F. Chen and D. G. MacDonald. Role of mixing in the structure and evolution of a buoyant discharge plume. *J. Geophys. Res.*, 111(C11002):doi:10.1029/2006JC003563, 2006.

F. Chen, D. G. MacDonald, and R. D. Hetland. Lateral spreading of a near-field river plume: observations and numerical simulations. *J. Geophys. Res.*, 114:C07013, doi:10.1029/2008JC004893, 2009.

G. C. Christodoulou. Interfacial mixing in stratified flows. *J. Hydraulic Research*, 24(2): 77–92, 1986.

D. B. Clark, F. Feddersen, and R. T. Guza. Cross-shore surfzone tracer dispersion in an alongshore current. *Journal of Geophysical Research: Oceans*, 115(C10), 2010. doi: 10.1029/2009JC005683. URL `https://agupubs.onlinelibrary.wiley.com/doi/abs/10.1029/2009JC005683`.

D. B. Clark, S. Elgar, and B. Raubenheimer. Vorticity generation by short-crested wave breaking. *Geophysical Research Letters*, 39(24):n/a–n/a, 2012. ISSN 1944-8007.

D. Codiga. *Unified Tidal Analysis and Prediction Using the UTide Matlab Functions.* University of Rhode Island, 2011.

K. L. Cole, D. G. MacDonald, G. Kakoulaki, and R. D. Hetland. River plume source-front connectivity. *Ocean Modelling*, 150:101571, 2020. doi: https://doi.org/10.1016/j.ocemod.2020.101571.

M. E. Davis and R. J. Davis. *Fundamentals of chemical reaction engineering.* McGraw-Hill, Boston, 2003. ISBN 9781628704372.

R. Dean and R. Dalrymple. *Water wave mechanics for engineers and scientists.* World Scientific, London, 1984. ISBN 9810204205.

M. Derakhti, J. Thomson, and J. T. Kirby. Sparse sampling of intermittent turbulence generated by breaking surface waves. *J. Phys. Oceanogr.*, 50:867–885, 2020. doi: https://doi.org/10.1175/JPO-D-19-0138.1.

J. Devine. *The Impacts of Beach Pollution.* Testing the Waters: 24th Edition. Natural Resources Defense Council, 2014.

T. H. Ellison and J. S. Turner. Turbulent entrainment in stratified flows. *J. Fluid Mech.*, 6: 423–448, 1959.

Ensmenger. Bringing back the blueback. `http://qlandandwater.org/departments/fisheries/salmon/`, Sept. 2010.

D. Farmer, R. Pawlowicz, and R. Jiang. Tilting separation flows: a mechanism for intense vertical mixing in the coastal ocean. *Dyn. Atmos. Oceans*, 36(1):43–58, 2002.

F. Feddersen. Quality controlling surf zone acoustic doppler velocimeter observations to estimate the turbulent dissipation rate. *J. Atmos. Ocean. Tech.*, 27(12):2694–2696, 2010.

F. Feddersen. Observations of the surfzone turbulent dissipation rate. *J. Phys. Oceanogr.*, 42:386–399, 2012a.

F. Feddersen. Scaling surf zone turbulence. *Geophys. Res. Lett.*, 39(18 (L18613)), 2012b. doi: 10.1029/2012GL052970.

F. Feddersen. The generation of surfzone eddies in a strong alongshore current. *Journal of Physical Oceanography*, 44(2):600–617, 2014/02/13 2014. doi: 10.1175/JPO-D-13-051.1. URL `http://dx.doi.org/10.1175/JPO-D-13-051.1`.

F. Feddersen and R. T. Guza. Observations of nearshore circulation: Alongshore uniformity. *Journal of Geophysical Research: Oceans*, 108(C1):6–1–6–10, 2003. doi: 10.1029/2001JC001293. URL `https://agupubs.onlinelibrary.wiley.com/doi/abs/10.1029/2001JC001293`.

F. Feddersen and J. H. Trowbridge. The effect of wave breaking on surf-zone turbulence and alongshore currents: A modeling study. *Journal of Physical Oceanography*, 35(11):2187–2203, 2005a. doi: 10.1175/JPO2800.1. URL `https://doi.org/10.1175/JPO2800.1`.

F. Feddersen and J. H. Trowbridge. The effect of wave breaking on surf-zone turbulence and alongshore currents: A modeling study. *J. Phys. Oceanogr.*, 35:2187–2203, 2005b.

F. Feddersen, R. T. Guza, S. Elgar, and T. H. C. Herbers. Alongshore momentum balances in the nearshore. *Journal of Geophysical Research: Oceans*, 103(C8):15667–15676, 1998. doi: 10.1029/98JC01270. URL `https://agupubs.onlinelibrary.wiley.com/doi/abs/10.1029/98JC01270`.

M. Fewings, S. J. Lentz, and J. Fredericks. Observations of cross-shelf flow driven by cross-shelf winds on the inner continental shelf. *Journal of Physical Oceanography*, 38(11):2358–2378, 2008.

H. B. Fischer. Mass transport mechanisms in partially mixed estuaries. *J. Fluid Mech.*, 53(4):671–687, 1972.

H. B. E. Fischer, J. List, R. C. Koh, J. Imberger, and N. H. Brooks. *Mixing in Inland and Coastal Waters*. Academic Press, San Diego, 1979.

A. W. Fisher, N. J. Nidzieko, M. E. Scully, R. J. Chant, E. J. Hunter, and P. L. F. Mazzini. Turbulent mixing in a far-field plume during the transition to upwelling conditions: Microstructure observations from an auv. *Geophysical Research Letters*, 45(18):9765–9773, 2018. doi: 10.1029/2018GL078543. URL `https://agupubs.onlinelibrary.wiley.com/doi/abs/10.1029/2018GL078543`.

D. A. Fong and W. R. Geyer. Response of a river plume during an upwelling favorable wind event. *J. Geophys. Res.*, 106(C1):1067–1084, 2001.

W. Fry. Tijuana sewage runoff prompts county to extend beach closure to imperial beach. *San Diego Union-Tribune*, 2020. URL `https://www.sandiegouniontribune.com/news/border-baja-california/story/2020-06-13/tijuana-sewage-runoff-prompts-county-to-extend-beach-closure-to-imperial-beach`.

R. W. Garvine. Observations of the motion field of the connecticut river plume. *Journal of Geophysical Research (1896-1977)*, 82(3):441–454, 1977. doi: 10.1029/JC082i003p00441. URL `https://agupubs.onlinelibrary.wiley.com/doi/abs/10.1029/JC082i003p00441`.

R. W. Garvine. Radial Spreading of Buoyant, Surface Plumes in Coastal Waters. *J. Geophys. Res.*, 89(C2):1989–1996, 1984.

R. W. Garvine. Estuary Plumes and Fronts in Shelf Waters: A Layer Model. *J. of Phys. Oceanogr.*, 17:1877–1896, 1987.

R. W. Garvine and J. D. Monk. Frontal structure of a river plume. *Journal of Geophysical Research (1896-1977)*, 79(15):2251–2259, 1974. doi: 10.1029/JC079i015p02251. URL `https://agupubs.onlinelibrary.wiley.com/doi/abs/10.1029/JC079i015p02251`.

G. Gerbi, J. Trowbridge, E. Terray, A. J. Plueddemann, and T. Kukulka. Observations of turbulence in the ocean surface boundary layer: energetics and transport. *J. Phys. Oceanogr.*, 39:1077–1096, 2009.

G. P. Gerbi, R. J. Chant, and J. L. Wilkin. Breaking surface wave effects on river plume dynamics during upwelling-favorable winds. *Journal of Physical Oceanography*, 43(9): 1959–1980, 2013/09/05 2013a. doi: 10.1175/JPO-D-12-0185.1. URL `http://dx.doi.org/10.1175/JPO-D-12-0185.1`.

G. P. Gerbi, R. J. Chant, and J. L. Wilkin. Breaking surface wave effects on river plume dynamics during upwelling-favorable winds. *Journal of Physical Oceanography*, 2013/08/05 2013b.

G. P. Gerbi, S. E. Kastner, and G. Brett. The role of whitecapping in thickening the ocean surface boundary layer. *Journal of Physical Oceanography*, 45(8):2006–2024, 2015/08/12 2015a. doi: 10.1175/JPO-D-14-0234.1. URL `http://dx.doi.org/10.1175/JPO-D-14-0234.1`.

G. P. Gerbi, S. E. Kastner, and G. Brett. The role of whitecapping in thickening the ocean surface boundary layer. *Journal of Physical Oceanography*, 45(8):2006–2024, 2015b.

W. Geyer, A. Lavery, M. Scully, and J. Trowbridge. Mixing by shear instability at high Reynolds number. *Geophys. Res. Lett.*, 37:L22607, doi:10.1029/2010GL045272, 2010.

W. R. Geyer and P. MacCready. The estuarine circulation. *Annual Review of Fluid Mechanics*, 46(1):175–197, 2014. doi: 10.1146/annurev-fluid-010313-141302. URL `https://doi.org/10.1146/annurev-fluid-010313-141302`.

W. R. Geyer, D. K. Ralston, and R. C. Holleman. Hydraulics and mixing in a laterally divergent channel of highly stratified estuary. *Journal of Geophysical Research: Oceans*, 122(6):4743–4760, 2017.

M. Gregg. Small-scale processes in straits. *Deep Sea Research Part II: Topical Studies in Oceanography*, 51(4–5):489 – 503, 2004. ISSN 0967-0645. doi: https://doi.org/10.1016/j.dsr2.2003.08.003. URL `http://www.sciencedirect.com/science/article/pii/S0967064504000293`. The Physical Oceanography of Sea Straits.

M. Gregg, E. D'Asaro, J. Riley, and E. Kunze. Mixing efficiency in the ocean. *Annual Review of Marine Science*, 10(1):443–473, 2018. doi: 10.1146/annurev-marine-121916-063643. URL `https://doi.org/10.1146/annurev-marine-121916-063643`. PMID: 28934598.

M. C. Haller, U. Putrevu, J. Oltman-Shay, and R. A. Dalrymple. Wave group forcing of low frequency surf zone motion. *Coastal Engineering Journal*, 41(02):121–136, 1999. doi: 10.1142/S0578563499000085. URL `https://doi.org/10.1142/S0578563499000085`.

M. C. Haller, R. A. Dalrymple, and I. A. Svendsen. Experimental study of nearshore dynamics on a barred beach with rip channels. *Journal of Geophysical Research: Oceans*, 107(C6): 14–1–14–21, 2002. doi: 10.1029/2001JC000955. URL `https://agupubs.onlinelibrary.wiley.com/doi/abs/10.1029/2001JC000955`.

K. Hally-Rosendahl and F. Feddersen. Modeling surfzone to inner-shelf tracer exchange. *Journal of Geophysical Research: Oceans*, 121(6):4007–4025, 2016. doi: 10.1002/2015JC011530. URL `https://agupubs.onlinelibrary.wiley.com/doi/abs/10.1002/2015JC011530`.

K. Hally-Rosendahl, F. Feddersen, and R. T. Guza. Cross-shore tracer exchange between the surfzone and inner-shelf. *Journal of Geophysical Research: Oceans*, 119(7):4367–4388, 2014. doi: 10.1002/2013JC009722. URL `https://agupubs.onlinelibrary.wiley.com/doi/abs/10.1002/2013JC009722`.

R. D. Hetland. The effects of mixing and spreading on density in near-field river plumes. *Dyn. Atmos. Oceans*, 49:37–53 doi:10.1016/j.dynatmoce.2008.11.003, 2010.

B. M. Hickey, R. M. Kudela, J. Nash, K. W. Bruland, W. T. Peterson, P. MacCready, E. J. Lessard, D. A. Jay, N. S. Banas, A. M. Baptista, E. P. Dever, P. M. Kosro, L. K. Kilcher, A. R. Homer-Devine, E. D. Zaron, R. M. McCabe, J. O. Peterson, P. Orton, J. Pan, and M. C. Lohan. River influences on shelf ecosystems: Introduction and synthesis. *J. Geophys. Res.*, 115:10.1029/2009JC005452, 2010.

R. A. Holman, K. L. Brodie, and N. J. Spore. Surf zone characterization using a small quadcopter: Technical issues and procedures. *IEEE Transactions on Geoscience and Remote Sensing*, 55(4):2017–2027, April 2017. ISSN 0196-2892. doi: 10.1109/TGRS.2016.2635120.

A. Horner-Devine, R. D. Hetland, and D. MacDonald. Transport and mixing in coastal river plumes. *Annual Review of Fluid Mechanics*, 47:569—594, 2015.

A. R. Horner-Devine. The bulge circulation in the Columbia River plume. *Cont. Shelf Res.*, 29:234–251, 2009.

J. G. Izett and K. Fennel. Estimating the cross-shelf export of riverine materials: Part 2. estimates of global freshwater and nutrient export. *Global Biogeochemical Cycles*, 32(2): 176–186, 2018. doi: 10.1002/2017GB005668. URL `https://agupubs.onlinelibrary.wiley.com/doi/abs/10.1002/2017GB005668`.

T. Janssen and J. Battjes. A note on wave energy dissipation over steep beaches. *Coastal Engineering*, 54(9):711 – 716, 2007. ISSN 0378-3839. doi: https://doi.org/10.1016/j.coastaleng.2007.05.006. URL `http://www.sciencedirect.com/science/article/pii/S0378383907000580`.

G. H. Jirka. Turbulent Buoyant Jets in Shallow Fluid Layers. In W. Rodi, editor, *Turbulent Buoyant Jets and Plumes*, page 184. Pergamon Press, 1982.

G. H. Jirka, E. E. Adams, and K. D. Stolzenbach. Buoyant surface jets. *J. Hydraulics Div., Proc. ASCE*, 107(HY11):1467–1487, November 1981.

G. R. Jones, J. D. Nash, R. L. Doneker, and G. H. Jirka. Buoyant Surface Discharges into Water Bodies. I: Flow Classification and Prediction Methodology. *J. Hydraulic Engineering*, 133(9):1010–1020, 2007.

J. T. Jurisa, J. D. Nash, J. M. Moum, and L. Kilcher. Controls on turbulent mixing in a strongly stratified and sheared tidal river plume. *Journal of Physical Oceanography*, 46 (8):2373–2388, 2016.

S. E. Kastner, A. R. Horner-Devine, and J. Thomson. The influence of wind and waves on spreading and mixing in the fraser river plume. *Journal of Geophysical Research: Oceans*, 123(9):6818–6840, 2018. doi: 10.1029/2018JC013765. URL `https://agupubs.onlinelibrary.wiley.com/doi/abs/10.1029/2018JC013765`.

S. E. Kastner, A. R. Horner-Devine, and J. M. Thomson. A conceptual model of a river plume in the surf zone. *Journal of Geophysical Research: Oceans*, 124(11):8060–8078, 2019. doi: 10.1029/2019JC015510.

L. Kilcher and J. Nash. Structure and dynamics of the Columbia River tidal plume front. *J. Geophys. Res.*, 115(C05S90):doi:10.1029/2009JC006066, 2010.

L. Kilcher, J. Nash, and J. N. Moum. The role of turbulence stress divergence in decelerating a river plume. *J. Geophys. Res.*, 117(C05032), 2012.

J. T. Kirby and T.-M. Chen. Surface waves on vertically sheared flows: Approximate dispersion relations. *Journal of Geophysical Research: Oceans*, 94(C1):1013–1027, 1989. doi: 10.1029/JC094iC01p01013. URL `https://agupubs.onlinelibrary.wiley.com/doi/abs/10.1029/JC094iC01p01013`.

N. Kumar and F. Feddersen. The effect of stokes drift and transient rip currents on the inner shelf. part i: No stratification. *Journal of Physical Oceanography*, 47(1):227–241, 2017a. doi: 10.1175/JPO-D-16-0076.1. URL `http://dx.doi.org/10.1175/JPO-D-16-0076.1`.

N. Kumar and F. Feddersen. The effect of stokes drift and transient rip currents on the inner shelf. part ii: With stratification. *Journal of Physical Oceanography*, 47(1):243–260, 2017b. doi: 10.1175/JPO-D-16-0077.1. URL `http://dx.doi.org/10.1175/JPO-D-16-0077.1`.

N. Kumar, G. Voulgaris, J. C. Warner, and M. Olabarrieta. Implementation of the vortex force formalism in the coupled ocean-atmosphere-wave-sediment transport (coawst) modeling system for inner shelf and surf zone applications. *Ocean Modelling*, 47(0):65 – 95, 2012. ISSN 1463-5003.

S. Lentz. The Response of Buoyant Coastal Plumes to Upwelling-Favorable Winds. *J. Phys. Oceanogr.*, 34(11):2458–2467, 2004.

S. J. Lentz and M. R. Fewings. The wind-and wave-driven inner-shelf circulation. *Annual Review of Marine Science*, 4:317–343, 2012.

S. J. Lentz and J. Largier. The influence of wind forcing on the chesapeake bay buoyant coastal current. *Journal of Physical Oceanography*, 36(7):1305–1316, 2006.

S. J. Lentz, M. Fewings, P. Howd, J. Fredericks, and K. Hathaway. Observations and a model of undertow over the inner continental shelf. *Journal of Physical Oceanography*, 38 (11):2341–2357, 2008.

M. Longuet-Higgins and R. Stewart. Changes in the form of short gravity waves on long waves and tidal currents. *Journal of Fluid Mechanics*, 8(4):565–583, 1960.

M. Longuet-Higgins and R. Stewart. The changes in amplitude of short gravity waves on steady non-uniform currents. *Journal of Fluid Mechanics*, 10(4):529–543, 1961.

M. Longuet-Higgins and R. Stewart. Radiation stress and mass transport in gravity waves, with application to 'surf beats'. *Journal of Fluid Mechanics*, 13(4):481–504, 1962.

M. Longuet-Higgins and R. Stewart. Radiation stresses in water waves; a physical discussion, with applications. *Deep Sea Research*, 11:529–562, 1964.

M. S. Longuet-Higgins. Longshore currents generated by obliquely incident sea waves: 1. *Journal of Geophysical Research*, 75(33):6778–6789, 1970.

D. Luketina and J. Imberger. Characteristics of a suface buoyant jet. *J. Geophys. Res.*, 92 (C5):5435–5447, 1987.

P. MacCready, W. R. Geyer, and H. Burchard. Estuarine exchange flow is related to mixing through the salinity variance budget. *J. Phys. Oceanogr.*, 48:1375–1384, 2018.

D. G. MacDonald and F. Chen. Enhancement of turbulence through lateral spreading in a stratified-shear flow: Development and assessment of a conceptual model. *J. Geophys. Res.*, 117(C05025):doi:10.1029/2011JC007484, 2012.

D. G. MacDonald and W. R. Geyer. Turbulent energy production and entrainment at a highly stratified estuarine front. *J. Geophys. Res.*, 109:C05004, doi:10.1029/2003JC002094, 2004.

D. G. MacDonald, L. Goodman, and R. D. Hetland. Turbulent dissipation in a near-field river plume: A comparison of control volume and microstructure observations with a numerical model. *J. Geophys. Res.*, 112:C07026, doi:10.1029/2006JC004075, 2007.

D. G. MacDonald, J. Carlson, and L. Goodman. On the heterogeneity of stratified-shear turbulence: Observations from a near-field river plume. *Journal of Geophysical Research: Oceans*, 118(11):6223–6237, 2013. doi: 10.1002/2013JC008891. URL `https://agupubs.onlinelibrary.wiley.com/doi/abs/10.1002/2013JC008891`.

J. MacMahan, J. Brown, J. Brown, E. Thornton, R. A, T. Stanton, M. Henriquez, E. Gallagher, J. Morrison, T. S. M. Austin, and N. Senechal. Mean lagrangian flow behavior on an open coast rip-channeled beach: A new perspective. *Marine Geology*, 268(1-4):110–133, 2010. doi: https://doi.org/10.1016/j.margeo.2009.09.011.

J. H. MacMahan, A. J. H. M. Reniers, E. B. Thornton, and T. P. Stanton. Surf zone eddies coupled with rip current morphology. *Journal of Geophysical Research: Oceans*, 109(C7), 2004. doi: 10.1029/2003JC002083. URL `https://agupubs.onlinelibrary.wiley.com/doi/abs/10.1029/2003JC002083`.

J. H. MacMahan, E. B. Thornton, and A. J. Reniers. Rip current review. *Coastal Engineering*, 53(2-3):191–208, 2006.

G. O. Marmorino and C. L. Trump. Gravity current structure of the chesapeake bay outflow plume. *Journal of Geophysical Research: Oceans*, 105(C12):28847–28861, 2000. doi: 10.

1029/2000JC000225. URL `https://agupubs.onlinelibrary.wiley.com/doi/abs/10.1029/2000JC000225`.

R. McCabe, B. M. Hickey, and P. MacCready. Observational estimates of entrainment and vertical salt flux in the interior of a spreading river plume. *J. Geophys. Res.*, 113(C08027), 2008.

R. McCabe, P. MacCready, and B. M. Hickey. Ebb-tide dynamics and spreading of a large river plume. *Journal of Physical Oceanography*, 39(11):2839–2856, 2009.

C. Mei. *The Applied Dynamics of Ocean Surface Waves*, volume 1 of *Advanced Series on Ocean Engineering*. World Scientific, Signapore, 1989.

M. Menzinger, M. Boukalouch, P. D. Kepper, J. Boissonade, J. C. Roux, and H. Saadaoui. Dynamical consequences of nonideal mixing in continuously stirred tank reactor studies of chemical instabilities: Comparative stirring effects of premixed and nonpremixed feeds on the bistable ci02$^-$ + i$^-$ reaction. *J. Phys. Chem.*, 90(2):313–315, 1986.

L. Metcalf, H. P. Eddy, and G. Tchobanoglous. *Wastewater engineering : treatment, disposal, and reuse*. McGraw-Hill, New York, 1979. ISBN 007124140X.

A. Miche. Mouvements ondulatoires de la mer en profondeur croissante ou decroissante. premiere partie. mouvements ondulatoires periodiques et cylindriques en profondeur constante. *Annales des Ponts et Chaussees*, 114:42–78, 1944.

J. D. Milliman and J. P. M. Syvitski. Geomorphic/tectonic control of sediment discharge to the ocean: The importance of small mountainous rivers. *The Journal of Geology*, 100(5): 525–544, 1992. doi: 10.1086/629606. URL `https://doi.org/10.1086/629606`.

Monterey Bay National Marine Sanctuary. Beach closures and microbial contamination. `https://montereybay.noaa.gov/resourcepro/beach_plan.html`, Dec. 2019.

M. Moulton, S. Elgar, B. Raubenheimer, J. C. Warner, and N. Kumar. Rip currents and alongshore flows in single channels dredged in the surf zone. *Journal of Geophysical Research: Oceans*, 122(5):3799–3816, 2017. doi: 10.1002/2016JC012222. URL `https://agupubs.onlinelibrary.wiley.com/doi/abs/10.1002/2016JC012222`.

W. Munk. Surf beats. *Eos, Transactions American Geophysical Union*, 30(6):849–854, 1949. doi: 10.1029/TR030i006p00849. URL `https://agupubs.onlinelibrary.wiley.com/doi/abs/10.1029/TR030i006p00849`.

J. Nash and J. Moum. River plumes as a source of large-amplitude internal waves in the coastal ocean. *Nature*, 437:400–403, 2005a. doi: 10.1038/nature03936.

J. D. Nash and J. N. Moum. River plumes as a source of large-amplitude internal waves in the coastal ocean. *Nature*, 437:400–403 doi:10.1038/nature03936, 2005b.

J. O'Donnell. The Formation and Fate of a River Plume: A Numerical Model. *J. of Phys. Oceanogr.*, 20(4):551–569, 1990.

J. O'Donnell, G. O. Marmorino, and C. L. Trump. Convergence and Downwelling at a River Plume Front. *J. Geophys. Res.*, 28:1481–1495, 1998.

M. Olabarrieta, W. R. Geyer, and N. Kumar. The role of morphology and wave-current interaction at tidal inlets: An idealized modeling analysis. *Journal of Geophysical Research: Oceans*, 119(12):8818–8837, 2014. doi: 10.1002/2014JC010191. URL `https://agupubs.onlinelibrary.wiley.com/doi/abs/10.1002/2014JC010191`.

D. H. Peregrine. Surf zone currents. *Theoret. Comput. Fluid Dynamics*, 10:295–309, 1998. doi: https://doi.org/10.1007/s001620050065.

Quinault Division of Natural Resources. Quinault salmon recovery program. `http://qlandandwater.org/departments/fisheries/salmon/`, Jan. 2020.

B. Raubenheimer, R. T. Guza, and S. Elgar. Wave transformation across the inner surf zone. *Journal of Geophysical Research: Oceans*, 101(C11):25589–25597, 1996. doi: 10.1029/96JC02433. URL `https://agupubs.onlinelibrary.wiley.com/doi/abs/10.1029/96JC02433`.

A. J. H. M. Reniers, J. H. MacMahan, E. B. Thornton, T. P. Stanton, M. Henriquez, J. W. Brown, J. A. Brown, and E. Gallagher. Surf zone surface retention on a rip-channeled beach. *Journal of Geophysical Research: Oceans*, 114(C10), 2009. doi: 10.1029/2008JC005153. URL `https://agupubs.onlinelibrary.wiley.com/doi/abs/10.1029/2008JC005153`.

S. E. Rennie, J. L. Largier, and S. J. Lentz. Observations of a pulsed buoyancy current downstream of Chesapeake Bay. *J. Geophys. Res.*, 104(C8):18,227–18,240, 1999.

A. R. Rodriguez, S. N. Giddings, and N. Kumar. Impacts of nearshore wave-current interaction on transport and mixing of small-scale buoyant plumes. *Geophysical Research Letters*, 45(16):8379–8389, 2018. doi: 10.1029/2018GL078328. URL `https://agupubs.onlinelibrary.wiley.com/doi/abs/10.1029/2018GL078328`.

M. Scully, W. Geyer, and J. Trowbridge. The influence of stratification and nonlocal turbulent production on estuarine turbulence: an assessment of turbulence closure with field observations. *J. Phys. Oceanog.*, 41(1):166–185, 2011.

L. Sherman. Thousands of beach closures and advisories linked to bacteria. *Daily Commerical*, 2019. URL `https://www.dailycommercial.com/news/20190720/thousands-of-beach-closures-and-advisories-linked-to-bacteria`.

W. Smyth, J. Nash, and J. Moum. Self-organized criticality in geophysical turbulence. *Nature Sci Rep.*, 9:3747, 2019. doi: https://doi.org/10.1038/s41598-019-39869-w.

M. Spydell and F. Feddersen. A lagrangian stochastic model of surf zone drifter dispersion. *J. Geophys. Res.*, 117(C3):C03041, 2012.

M. Spydell, F. Feddersen, R. T. Guza, and W. E. Schmidt. Observing surf-zone dispersion with drifters. *Journal of Physical Oceanography*, 37(12):2920–2939, 2012/01/25 2007. doi: 10.1175/2007JPO3580.1. URL `http://dx.doi.org/10.1175/2007JPO3580.1`.

G. G. Stokes. On the theory of oscillatory waves. *Transactions of the Cambridge Philosophical Society*, 8:441–482, 1847.

P. P. Sullivan, J. C. McWilliams, and W. K. Melville. The oceanic boundary layer driven by wave breaking with stochastic variability. part 1. direct numerical simulations. *Journal of Fluid Mechanics*, 507:143–174, 5 2004. ISSN 1469-7645. doi: 10.1017/S0022112004008882.

G. Tchobanoglous, H. D. Stensel, R. Tsuchihashi, F. L. Burton, and M. Abu-Orf. *Wastewater engineering : treatment and resource recovery*. McGraw-Hill Education, New York, 2014. ISBN 9780073401188.

E. Terray, M. Donelan, Y. Agrawal, W. Drennan, K. Kahma, A. Williams, P. Hwang, and S. Kitaigorodskii. Estimates of kinetic energy dissipation under breaking waves. *J. Phys. Oceanogr.*, 26:792–807, 1996.

J. Thomson. Wave breaking dissipation observed with SWIFT drifters. *Journal of Atmospheric and Oceanic Technology*, 29(12):1866–1882, 2013/01/03 2012. doi: 10.1175/JTECH-D-12-00018.1.

J. Thomson, S. Elgar, T. H. C. Herbers, B. Raubenheimer, and R. T. Guza. Refraction and reflection of infragravity waves near submarine canyons. *Journal of Geophysical Research*, 112(C10009), 2007.

J. Thomson, A. R. Horner-Devine, S. Zippel, C. Rusch, and W. Geyer. Wave breaking turbulence at the offshore front of the columbia river plume. *Geophysical Research Letters*, 41(24):8987–8993, 2014. doi: 10.1002/2014GL062274. URL `https://agupubs.onlinelibrary.wiley.com/doi/abs/10.1002/2014GL062274`.

J. Thomson, M. S. Schwendeman, S. F. Zippel, S. Moghimi, J. Gemmrich, and W. E. Rogers. Wave-breaking turbulence in the ocean surface layer. *Journal of Physical Oceanography*, 46(6):1857–1870, 2016. doi: 10.1175/JPO-D-15-0130.1. URL `http://dx.doi.org/10.1175/JPO-D-15-0130.1`.

J. Thomson, M. Moulton, A. de Klerk, J. Talbert, M. Guerra, S. E. Kastner, M. M. Smith, M. Schwendeman, S. Zippel, and S. Nylund. A new version of the swift platform for waves, currents, and turbulence in the ocean surface layer. *Current, Waves, and Turbulence Measurement and Applications Workshop*, 2019.

E. B. Thornton and R. T. Guza. Transformation of wave height distribution. *Journal of Geophysical Research: Oceans*, 88(C10):5925–5938, 1983. doi: 10.1029/JC088iC10p05925. URL `https://agupubs.onlinelibrary.wiley.com/doi/abs/10.1029/JC088iC10p05925`.

E. B. Thornton and R. T. Guza. Surf zone longshore currents and random waves: Field data and models. *Journal of Physical Oceanography*, 16(7):1165–1178, 1986.

M. E. Williams and M. T. Stacey. Tidally discontinuous ocean forcing in bar-built estuaries: The interaction of tides, infragravity motions, and frictional control. *Journal of Geophysical Research: Oceans*, 121(1):571–585, 2016. doi: 10.1002/2015JC011166. URL `https://agupubs.onlinelibrary.wiley.com/doi/abs/10.1002/2015JC011166`.

S. H. C. Wong, S. G. Monismith, and A. B. Boehm. Simple estimate of entrainment rate of pollutants from a coastal discharge into the surf zone. *Environmental Science & Technology*, 47(20):11554–11561, 2013. doi: 10.1021/es402492f. URL `https://doi.org/10.1021/es402492f`. PMID: 24006887.

R. Xia. See how your favorite beach ranks in the latest pollution report card. *Los Angeles Times*, 2020. URL `https://www.latimes.com/california/story/2020-06-30/california-beach-report-card`.

Y. Yuan and A. Horner-Devine. Laboratory investigation of the impact of lateral spreading on buoyancy flux in a river plume. *J. Phys. Oceanogr.*, 43(12):2588–2610, 2013.

S. Zippel and J. Thomson. Wave breaking and turbulence at a tidal inlet. *Journal of Geophysical Research: Oceans*, pages n/a–n/a, 2015. ISSN 2169-9291. doi: 10.1002/2014JC010025. URL `http://dx.doi.org/10.1002/2014JC010025`.

S. Zippel and J. Thomson. Surface wave breaking over sheared currents: Observations from the mouth of the columbia river. *Journal of Geophysical Research: Oceans*, pages n/a–n/a, 2017. ISSN 2169-9291. doi: 10.1002/2016JC012498. URL `http://dx.doi.org/10.1002/2016JC012498`.